Microelectrode Arrays based on Transfer-free Multilayer Graphene and PEDOT:PSS for Neural Activity Detection

Delft University of Technology

Master of Science in Biomedical Engineering
November 2024

Nerea Alvarez de Eulate Llano

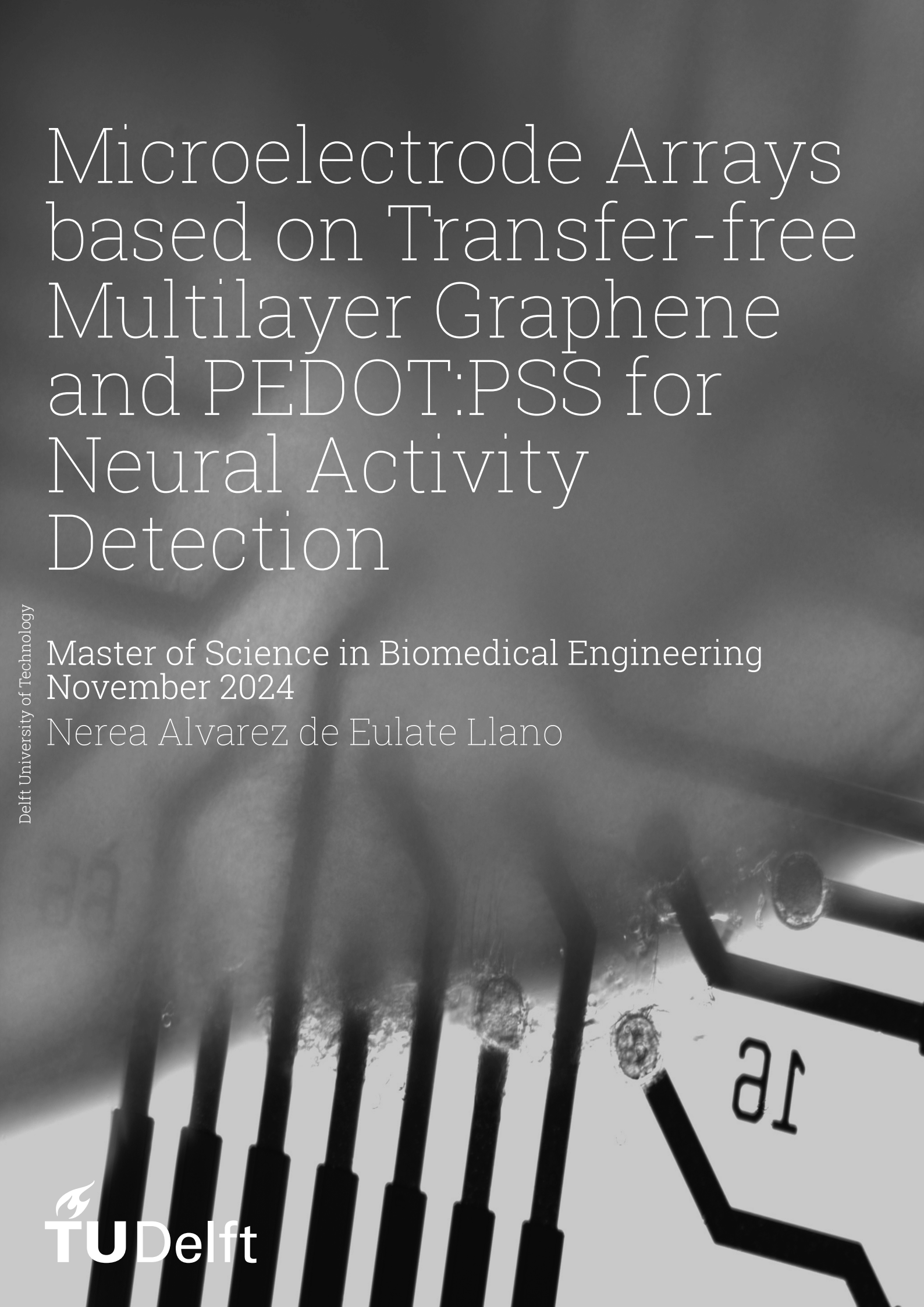

TU Delft

Microelectrode Arrays based on Transfer-free Multilayer Graphene and PEDOT:PSS for Neural Activity Detection

by

Nerea Alvarez de Eulate Llano

to obtain the degree of Master of Science
at the Delft University of Technology,
to be defended publicly on Friday November 22, 2024 at 10:00 AM.

Student Number:	5827876	
Project Duration:	December, 2023 - November, 2024	
Thesis committee:	Dr. Vasiliki Giagka	TU Delft, supervisor
	Dr. Sten Vollebregt	TU Delft, supervisor
	Dr. Achilleas Savva	TU Delft
	Dr. Murali Ghatkesar	TU Delft

TU Delft

Abstract

Resolving the underlying mechanisms of complex brain functions and associated disorders remains a major challenge in neuroscience, largely due to the difficulty in mapping large-scale neural network dynamics with high temporal and spatial resolution. Multimodal neural platforms that integrate optical and electrical modalities offer a promising solution, with microelectrode arrays (MEAs) being particularly effective for capturing electrophysiological activity across multiple neurons at the cellular level. Graphene has emerged as a highly attractive material for such neural interfaces due to its unique combination of biophysical, electrical, mechanical, biological, and optical properties. However, current graphene-based electrodes face challenges, including the need for transferring pre-grown graphene layers, which causes reliability issues.

In this work, microelectrode arrays based on transfer-free multilayer graphene and PEDOT:PSS are developed, and their feasibility for *in vitro* neural activity detection is evaluated through a brain slice culture. Firstly, the design and fabrication of graphene-based MEAs (grMEA) on transparent substrates is presented, establishing optimized microfabrication procedures for the integration of transfer-free multilayer graphene technology on *in vitro* MEAs. Several electrode diameters, ranging from 10 µm to 500 µm, are included to accommodate different experimental requirements and test the limits of the technology. Second, the combination of graphene and PEDOT:PSS conductive polymer is explored to overcome the fundamental limitations associated with graphene electrodes, such as high impedance at small electrode sizes, without compromising the optical transparency. A technique to integrate patterned PEDOT:PSS polymer coating on the electrodes to form graphene/PEDOT:PSS microelectrodes (grppMEA) is developed.

The electrochemical performance, including charge storage capacity (CSC) and impedance properties, of the grMEA and grppMEA devices are evaluated. Obtained results, comparable with state-of-the-art neural interfaces, show that the PEDOT:PSS coating increases CSC values more than the double and substantially reduces the impedance by 10-20 times (e.g., from 247 $k\Omega$ to 13 $k\Omega$ for 50 µm diameter electrodes). This demonstrates the potential of the devices for efficient electrical coupling with neural tissue. Additionally, the volumetric capacitance of grppMEA electrodes was found to be 55.7 F/cm^3, highlighting the volumetric ionic-electronic interaction coming from the PEDOT:PSS film, a feature absent in metal electrodes.

A custom-made interface that effectively connects the MEA devices to specific recording systems is developed to enable the acquisition of neural signals. The electrophysiological recording capabilities of the grMEA and grppMEA devices were subsequently evaluated through *in vitro* cerebellar brain slice cultures. Acute recordings of spontaneous activity and spike pattern characteristics of Purkinje cells and other neurons have been successfully obtained. The obtained signal-to-noise ratio values, $\sim$ 30 dB, demonstrate the great recording potential of the proposed MEAs. Overall, the results presented in this work demonstrate that transfer-free multilayer graphene MEA technology, especially when combined with PEDOT:PSS, overcomes the current limitations and offers the possibility for high-density recordings with single-cell resolution.

Thesis Framework

The work presented in this MSc thesis has been developed in Technische Universiteit Delft (TU Delft), within the Bioelectronics and ECTM (Electronic Components, Technology and Materials) groups, under the supervision of Dr. Vasiliki Giagka and Dr. Sten Vollebregt. The realization of this work was done taking advantage of numerous laboratories, from microfabrication cleanroom facilities (Else Kooi Laboratory, MEMS Lab) to material characterization and assembly labs. The research involved collaboration with several experts. The PEDOT:PSS solution preparation and fabrication protocol as well as the parylene lift-off fabrication method were kindly shared with us by Dr. Achilleas Savva and his team, specializing in organic bioelectronics. Dr. Filipe Arroyo Cardoso motivated the potential application of graphene in biosensing applications. *In vitro* experiments have been performed with the collaborations of Dr. Zhenyu Gao at the Erasmus Medical Center (Erasmus MC) in Rotterdam. Ongoing research on the development of flexible graphene electrodes for *in vivo* applications continues within the Dutch Brain Interface Initiative (DBI2) project.

Acknowledgements

There are many the people that in one way or another helped me during this academic trip and I would like to express my gratitude. First of all, I would like to thank my two supervisors, Dr. Vasiliki Giagka and Dr. Sten Vollebregt for giving me the opportunity to join this project. As a MSc student, I feel incredibly fortunate to have been able to conduct this research in such a stimulating environment. Despite having no prior practical experience in microfabrication processes, you both gave me the confidence, knowledge, and means to explore the art of cleanroom process development. After countless hours in the cleanroom, I went from being a complete beginner to becoming a more confident researcher with (at least some!) critical thinking skills. Thank you Vasso for your great leadership, ambition, enthusiasm, expertise on neural interfaces and for always pushing me to go the extra mile. Thank you Sten for your guidance, for being a master of graphene and always finding some time to discuss and rescue me from process difficulties. It has been truyly inspiring to learn and work from and with both of you. And of course, I cannot forget about Dr. Christos Pavlou, thank you for all your scientific and personal advice, your constant support and for reminding me to enjoy the process.

A big thank you to all the colleagues from the Bioelectronic group. To Dr. Achilleas Savva, for your constructive inputs, encouragement and for making me discover how fascinating PEDOT:PSS polymer is. To Liwen Wang and Mustafeez Shah for the nice electrochemistry discussions and always sharing and helping together along the way. To all the members in the Bioelectronics group — Johan, Ronald, Samuel, Niloufar, Limitha, Diogo, Cesc, Chris, Bakr… — for creating such a nice working and social atmosphere. To Brian and Kellen for their technical and management support, as well as their great initiatives and ideas for organizing cool events. To all my colleagues along the way — Maria, Bea, Ines, Juanfran and Cecilia… — you all created a very warm environment! Special thanks to the Bioelectronics branch in Berlin for your help and valuable contribution on the design of the PCBs. Not to forget Gonzalo for always being available to share his valuable knowledge on the topic. It has been a great pleasure to contribute and advance the project that initiated with you.

I'd also like to extend my sincere thanks to the EKL staff — Francesco, Hande, Daniel, Johannes, Paolo, Bruno… — you are the real heroes of the cleanroom! Thank you for all the trainings, your daily support in the cleanroom, thoughtful discussions and for giving me the opportunity to be part of the EKL team as a Cleanroom Engineer Assistant, which greatly broadened the horizon of my work.

I would also like to acknowledge the collaborators without whom the preliminary clinical validation of our technology would not have been possible. Thanks to Dr. Gerard Borst and Dr. Zhenyu Gao from the Neuroscience Department in Erasmus MC for believing in graphene electrodes technology, your great interest and willingness to collaborate.

Finally, I would like to dedicate these last lines to all of you that gave me continuous support and love along the challenging path of this scientific journey. To all my friends in Delft, Agapi and Fellow Loyaliszts, I only feel grateful that our paths crossed and built a beautiful chapter of my life. To Aina for accompanying me by the hand in this journey. To my parents for the confidence you have always had in me. All my achievement in life would not have been possible without your love and support.

My deepest thanks to all of you!

Nerea Alvarez de Eulate Llano
Delft, November 2024

Contents

1

Introduction

1.1. Neural cells and their electrical properties

Neurons are excitable cells within the human nervous system that are capable of generating and transmitting electrical impulses [1]. These impulses, known as action potentials, are responsible for communication between neurons and the transmission of information throughout the nervous system. The structure of a neuron typically consists of three main parts: the soma or body cell, dendrites and axon. Dendrites receive electrical signal coming in and the axon conducts the electrical impulse.

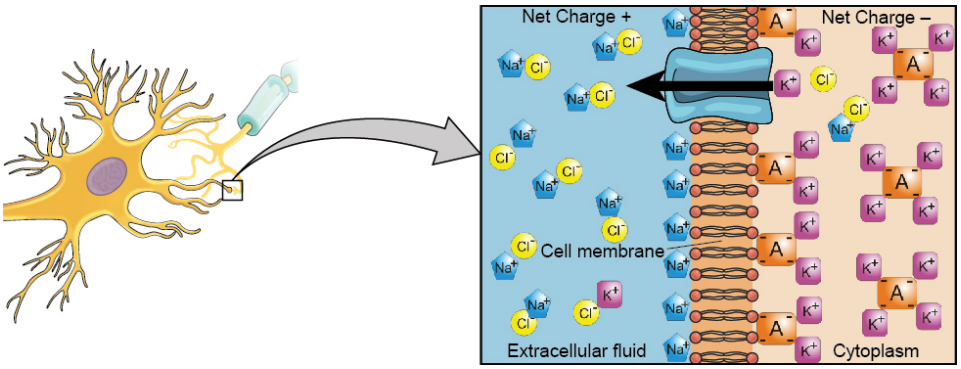

Figure 1.1: Membrane potential of a neuron at resting state. At the resting state of a neuron, the intracellular space is more negatively charged compared to the extracellular space. Na^+ ions are highly concentrated outside the cell, whereas K^+ ions are more concentrated in the inside, and together with other organic anions the interior net charge becomes more negative. Ion channels are permeable to specific ions (Na^+, K^+), which allow them to move in and out, contributing to the dynamic behaviour of the cell membrane potential. Image taken from [1].

Depending on their membrane potential, neurons can be in different states: the *resting* state, where it is not transmitting signals, the *action potential* state, where it is actively transmitting signals and a *depolarization state* without necessarily firing an action potential. This depolarization can occur due to excitatory inputs that bring the membrane potential closer to the threshold but do not reach it, resulting in subthreshold phenomena. At resting, neurons have a polarized membrane with a negative internal charge and a positive external charge (see Fig. 1.1). When the excitation threshold is exceeded, the neuron undergoes large depolarization, which leads to the generation of an action potential. The action potential is a rapid, temporary change in the electrical charge of the neuron's membrane. This change is due to the movement of positively charged ions, such as sodium and potassium, across the cell membrane. The movement of these ions is facilitated by ion channels, which are protein structures embedded in the cell membrane. These ion channels open and close in response to changes in the membrane potential, allowing ions to flow in and out of the neuron. The flow of ions during the action potential is a crucial process in neuronal communication. During the action potentials, the electrical charge across the membrane changes dramatically (see Fig. 1.2 b). After the depolarization phase,

the neuron goes through repolarization, where the cell's interior becomes negative again. This is followed by a brief period of hyperpolarization, during which the neuron is less likely to generate another action potential. This is known as the *refractory period*.

Understanding the electrical properties of neurons provides insights into the fundamental mechanisms of brain function and has important implications for various fields, including neuroscience, medicine, and technology.

1.2. Electrophysiological recording of neuronal activity

Our nervous system can be seen as an electro-chemical machine. Nerve impulses are transmitted through both chemical conduction between neurons (via neurotransmitters) and electrical conduction along the neuron (via ion channels). This means that electricity can also be used as a mean to interact with the nerves and neural cells [2, 3]. This field is known as *bioelectronic medicine* or *electroceuticals*. Unlike traditional medicine, dominated by the use of pharmaceuticals to interact with the nervous system, bioelectronic medicines have the potential to detect and modulate electrical signals of excitable cells in a highly selective manner and tailored to the need of the patient. Bidirectional bioelectronic systems entail miniature, implantable devices distributed close to the target tissue(s) operating in a close-loop manner. Meaning that the system is capable of sensing, deciphering electrical signals, analysing them in real time and modulating (stimulating) accordingly: the envisioned path towards high-precision personalized therapy. This current work focuses on the electrical recording side.

The patch clamp technique is considered to be the first generation of neural interfaces for electrophysiological recording of neuronal activity [4]. The patch clamp technique involves inserting a microelectrode into a single neuron to record single ion channel signals, i.e., intracellular recording (see Fig. 1.2 a). This technique was first introduced by Erwin Neher and Bert Sakmann in 1976, and made it possible to understand and characterize the active behaviour of the neurons membrane through the well-known Hodgkin-Huxley model. It has since revolutionized the field of electrophysiology.

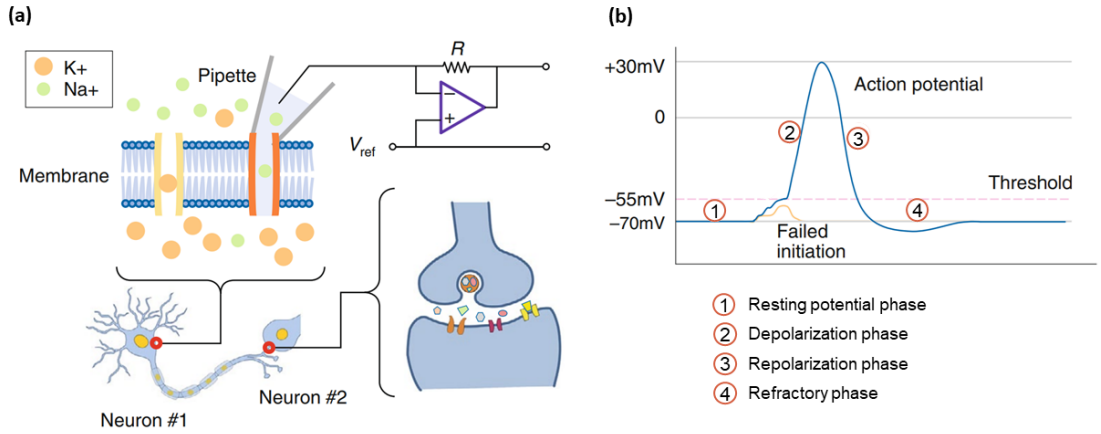

Figure 1.2: (a) Patch clamp technique illustration. A glass pipette electrode makes contact with the cell membrane and measures the current of a single ion channel, as well as the capacitance of the cell membrane. **(b) Typical action potential of a neuron**. When the excitation threshold is exceeded, the neuron rapidly undergoes a depolarization phase in which the membrane potential becomes less negative. Subsequently, the repolarization and hyperpolarization phases return the membrane potential to its resting state. Image taken from [4].

With the second generation of neural interfaces, both implantable electrode devices and *in vitro* microelectrode arrays (MEAs) have emerged to enable simultaneous recording from multiple neurons or brain regions. Implantable systems allow for *in vivo* monitoring, e.g., in chronic studies, while MEAs provide a controlled environment for studying neuronal activity. Electrode array technologies enable extracellular recording of neuronal activity, which is typically a result of the signal summation of multiple

neurons in a localized region [4]. This allows neuroscientists to study the collective activity patterns and interactions between neurons. MEAs are especially valuable in neuroscience because of their versatility in studying neural activity across various experimental models, including cell cultures, brain slices, and organoids. In cell cultures, these devices allow researchers to record and stimulate neuronal networks, offering insights into how neurons develop, connect, and function. Furthermore, their use with organoids, lab-grown miniature versions of brain tissue, has become increasingly common, allowing for the monitoring of the maturation and activity of complex 3D neural networks. This capability to record from multiple neurons or clusters simultaneously, without invasive procedures, makes MEAs an indispensable tool for neuroscientists. More advanced generations of *in vitro* neural interfaces now integrate MEAs with organ-on-a-chip systems, which better replicate physiological conditions by more precisely controlling the biological environment and maintaining tissue-specific functions. Other advanced generations of neural interfaces are directing towards combining electrophysiological recording with other modalities, such as optogenetics or imaging techniques, to provide a more comprehensive understanding of neural activity and circuitry [5].

1.3. Optical imaging tools for neuroscientific research

Optical imaging methods are very powerful tools in neuroscience to record and manipulate neural activity with high spatiotemporal resolution [6]. In particular, there is a growing interest for *in vivo* recordings using fluorescence imaging in the neuroscience research field as a way to monitor the spiking activity of a large number of neurons [7, 8, 9], thus expanding the understanding of the neural connectivity within specific brain regions. This technique is also useful for *in vitro* models, allowing to reveal information on the synaptic communication between neurons on a cell culture or brain slice. Typically, in optical functional imaging a genetically encoded indicator sensitive to neural activity is introduced to the target cells. There exist different fluorescing indicators, calcium and voltage being the most common ones. When an action potential occurs in a neuronal cell, the voltage-gated calcium channels open leading to an influx of Ca^{2+} ions and a subsequent increase in the intracellular Ca^{2+} concentration. Genetically encoded calcium indicators (GECIs) respond to the increase in Ca^{2+} concentration by emitting fluorescence when excited at a specific wavelength. GCaMP6 is a well-known calcium indicator based on green fluorescence protein (GFP) with a peak excitation wavelength of 485 nm and a peak emission wavelength of 515 nm [10].

Alternatively, genetically encoded voltage indicators (GEVIs), also present an alternative way to monitor neuronal activity. The voltage-sensitive dye molecules bind to the cell membrane and convert membrane potential changes into fluorescence signals. Voltage-sensitive dye imaging (or voltage imaging) presents a more direct way of measuring neuronal signals compared to calcium indicators. Importantly, it has been shown that voltage-sensitive dyes emit fluorescence proportional to the changes in the membrane potentials [11]. This makes it possible to monitor sub-threshold membrane phenomena. GEVIs additionally provide the benefit of instantaneous response due to their fast kinetics, which makes it possible to capture high-frequency neuronal activity (e.g., spiking activity of the Purkinje cells) which are unable to reveal by calcium imaging.

Several microscopy systems can provide illumination for fluorescent imaging. Traditional fluorescence microscopy, such as confocal, relies on a linear one-photon absorption process to generate a signal. Such techniques are adequate for imaging superficial tissue (less than 100 µm), however, at greater depths light scattering compromises the image quality [12]. The recent development of multiphoton imaging such as two-photon (2P) microscopy overcomes the limitations by allowing the visualization of deeper tissue. It relies on a nonlinear two-photon absorption process, where two photons of light with double the wavelength interact nonlinearly with matter to excite fluorophores. This creates a more tight and controllable focal point and makes it possible to image through thick, high scattering tissue, e.g., brain [13]. The laser wavelengths used for these systems vary, from around 635 nm in confocal microscopy to approximately 920 nm for 2P microscopy.

1.4. The need of multimodal neural interfaces

In neuroscience research, electrophysiology has been the most standard method for recording single-cell neuronal activity to behavioural outcome [14, 15]. Although it provides high temporal resolution, it has the limitation of not being able to record the activity of a large number of neurons. Recent advancements in optical methods, such as two-photon (2P) microscopy, has enable to capture the activity of densely packed neurons, opening the path towards understanding the complex spatial network dynamics of a group of neurons. However, the slow kinetic of the calcium indicator and/or the frame acquisition rate of the microscope system limit the temporal resolution in 2P imaging [16, 17]. This reveals that there is a need of combining the advantages of both modalities in order to have high spatiotemporal resolution. In this context, microelectrode arrays compatible with imaging techniques present a very promising tool. The most common materials for electrodes are gold (Au) or platinum (Pt) due to their good electrical performance, high biocompatibility and chemical stability [18]. However, they are opaque materials and thus, it would not allow the visualization of neuronal cells under the electrodes.

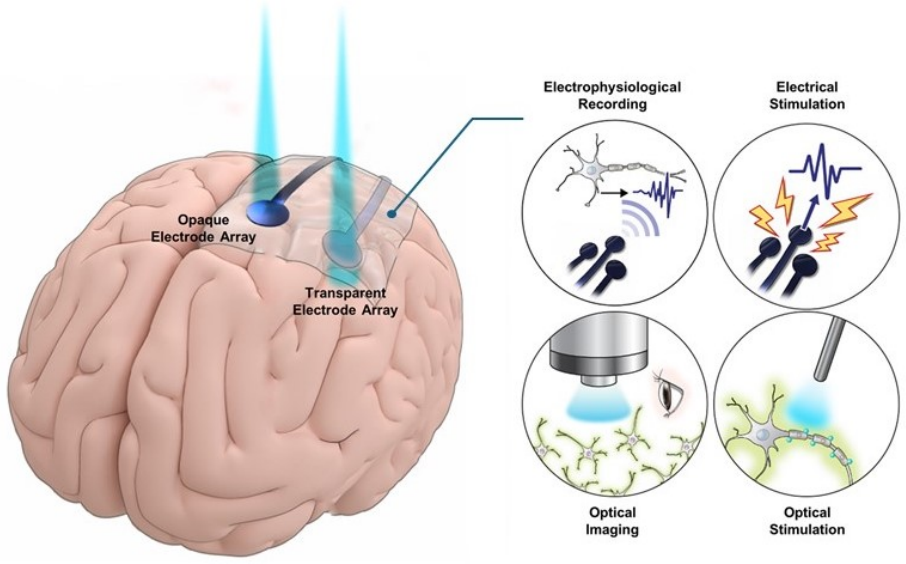

Figure 1.3: Transparent neural interfaces for multimodal applications. Transparent electrode arrays compatible with electrophysiological recording, stimulation, optical imaging (e.g., two-photon calcium imaging) and optical stimulation (optogenetics). Image adapted from [19].

Along with this, electrode technologies are advancing towards high-density arrays with single-cell resolution. A critical aspect is that the impedance scales up with decreased electrode dimensions due to the reduction in surface area. Electrode impedance reflects how efficiently signals are transduced. This highlights the need for novel materials that can offer a multimodal interface and record neural signals with high sensitivity.

1.5. Research Objectives

The goal of the research presented in this thesis was to develop optically transparent graphene-based microelectrode arrays (MEAs) by means of microfabrication technologies for multimodal neural interfaces. Microfabrication enables the achievement of a miniaturized neural interface by using photolithography techniques. The fabrication of the envisioned MEA devices was carried out at the Else Kooi Laboratory (EKL) of Delft University of Technology.

To achieve this, several critical aspects of this goal have been investigated. First, a thoughtful analysis of the microfabrication process based on previous work [20] was carried out, identifying several critical steps to improve and optimize. Some of the main fabrication aspects that this research work focus on were: (1) developing transfer-free graphene with complete removal of the underneath metal catalyst

layer, (2) optimizing MEAs design by enhancing track conductivity and integrating multiple electrode sizes, (3) reducing electrical impedance by surface modification strategies. Special focus was made on the last point, by exploring PEDOT:PSS as a conductive coating for graphene to further improve the electrode-electrolyte interface. Since the impedance of graphene is limited by the capacitance of the electrochemical double-layer, its combination with a PEDOT:PSS coating was investigated. The interaction between these two materials, which is not extensively studied in the literature, was explored.

Then, a full assessment of the electrochemical characteristics of the fabricated graphene MEAs was performed, and the performance between graphene/PEDOT:PSS and graphene electrodes was compared. The MEA devices were designed to offer a great versatility for electronic read-out, by allowing to be coupled to various commercially available electrophysiology recording systems. In this work, a custom-made interface that effectively connects the MEA devices to a specific recording system is presented. Finally, the MEA devices were evaluated through a *ex vivo* model, with some cerebellar brain slices with the aim to assess their recording capabilities in a biological environment.

1.6. Outline of the Report

This thesis is organized in 7 chapters. Chapter 1 introduced the underlying concepts of neural cells and their electrical activity, including the active behaviour of neurons and the generation of extracellular action potentials and local field potentials. A brief overview of the historical development of neural activity recording techniques is provided. Moreover, optical imaging methods for neuroscientific purposes are discussed, given their potential for understanding complex neural network dynamics. The concept of multimodal neural interfaces, which enables the combination of electrical and optical domains, is introduced.

Chapter 2 describes fundamental theory of electrodes, introducing an electrical equivalent model which facilitates the understanding of the components contributing to the electrode-electrolyte interface. Standardized methods to characterize the electrochemical performance of electrodes are presented. Next, state-of-the-art graphene-based electrode technologies are reviewed, highlighting their novelties and limitations in neural recording applications. A unique approach for the fabrication of transfer-free multilayer graphene, developed by researchers at TU Delft, is described. Then, surface modification techniques to improve the electrochemical performance of graphene electrodes, such as coatings with conductive polymers like PEDOT:PSS, are discussed. Finally, some concepts about biological characterization of electrodes, including biocompatibility and signal-to-noise ratio (SNR) are introduced.

In Chapter 3, the design of *in vitro* MEAs on transparent substrates is presented. In particular, the design of the photolithography masks that will define the patterns on each material layer on the processed wafers are described. Design choices and considerations regarding the dimensions and geometries of the electrodes, interconnections and contact pads are explained, taking into account layer-to-layer margins to minimize challenges that may arise during the different fabrication steps. In this chapter, a brief analysis on the electrical crosstalk effect between neighbouring electrodes is also presented.

Chapter 4 focuses on the fabrication aspects of MEAs based on the transfer-free multilayer graphene technology. A detailed step-by-step microfabrication process of graphene MEAs is described, as well as the integration of a patterned PEDOT:PSS coating on the electrodes using the parylene lift-off technique. Process observations and challenges encountered during the development of theses devices are discussed and substantiated with optical images, SEM analysis and Raman spectroscopy.

Detailed material characterization methods and results, namely Raman spectroscopy, four-point probe sheet resistivity and optical transparency are presented in Chapter 5. Additionally, the electrochemical characterization of the fabricated graphene and PEDOT:PSS-coated graphene electrodes, including cyclic voltammetry (CV) and electrochemical impedance spectroscopy (EIS) is reported. The influence of the PEDOT:PSS coating on the electrochemical performance is analyzed.

Chapter 6 presents a custom-made interface that effectively connects the MEA devices to specific recording system and enables the acquisition of neural signals. The interface consists of a custom PCB which interchangeably couples the MEA pads to a connector compatible with commercially available recording hardware from Intan Technologies. Finally, the electrophysiological recording capabilities of the fabricated graphene and PEDOT:PSS-coated graphene MEAs are evaluated through *in vitro* experiments using cerebellar brain slice cultures. The post-processing of the acquired data and the computation of SNR values is reported and discussed.

The thesis concludes with Chapter 7 which summarizes the key achievements of this work, discusses the limitations and provides an outlook on future research directions.

2

Literature Review

2.1. Electrodes theory

Electrodes represent the interface between the biological cells/tissues and the electronic systems. They transduce the ionic currents naturally present in the body to electronic signals, from ions to electrons and inversely. In a neural interface, electrodes can be used bidirectionally, either 'recording' meaning signals are sensed or 'stimulating' meaning signals are injected into the tissue. For *in vitro* cell recording application, typically microelectrode arrays (MEAs) are used, referring to a device with multiple microelectrode elements.

2.1.1. Electrical equivalent circuit of an electrode recording system

Modelling the general electrical behaviour of an electrode system gives valuable insights on the role that each component can play in the system. Fig. 2.1 shows the electrical circuit for a microelectrode recording system [21].

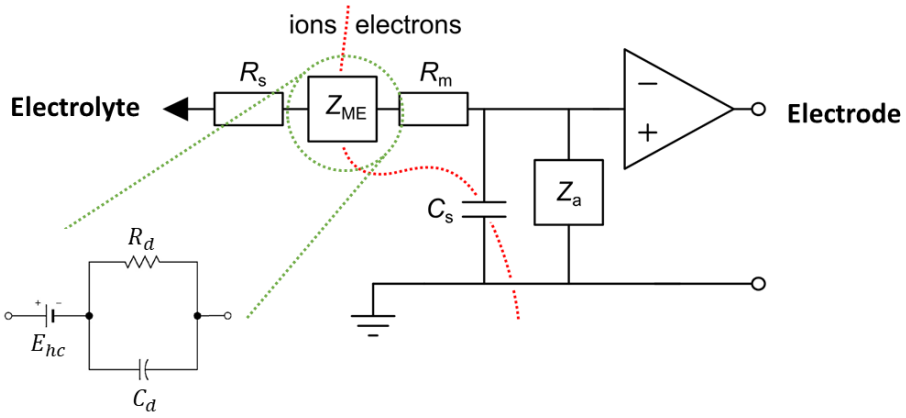

Figure 2.1: Equivalent electrical circuit of a recording microelectrode. E_{hc} refers to the half-cell potential, R_d and C_d are associated to the resistive and capacitive components, respectively, of the double layer formed at the electrode-electrolyte interface. And R_s describes the resistance intrinsic to the electrolyte solution [21, 22].

The ions from the electrolyte first encounter the resistance intrinsic to the solution, R_s. Following the circuit in Fig. 2.1, the red dots represent the electrode-electrolyte interface, where the conversion between ionic and electrical charge carriers happens. This is represented by an impedance element, Z_{ME}, which has a frequency dependent behaviour. The electrode impedance magnitude at 1 kHz is, in fact, the most accepted and practical quality metric for recording microelectrodes. The electrode-electrolyte interface will be further analysed in the following section. The shunt capacitance, C_s, rep-

resents the coupling capacitances present in the system which can arise due to electrical crosstalk between adjacent traces and/or capacitive coupling to the substrate or electrolyte solution. The tracks from the microelectrodes to the external contact pads (for connection to an amplifier), present an intrinsic resistance which is represented by the R_m element. This value depends on the sheet resistance of the material as well as the width and length of the tracks. The wider the tracks, the lower the resistive component. However, in high-density and large coverage microelectrode arrays, the width of the tracks might be compromised due to the lack of physical space in the layout. The last component of this equivalent circuit represents the input impedance of the amplifier, Z_a. Typically, high input impedances are desirable to capture small extracellular potentials, as well as low intrinsic noise amplitudes.

2.1.2. Electrode-electrolyte interface

The term *electrode-electrolyte interface*, Z_{ME}, is the fundamental term that analyses the passage of current from the electrode to the electrolyte and the involved electrochemical reactions. The electrolyte contains ions, anions and cations, representing the body fluid. The electrodes represent the interface that allows the transfer of charge between carriers, transitioning between electronic and ionic signals [22].

The electrical characteristics of electrodes have been widely studied throughout the years, in particular, the current-voltage relationship. Electrodes behaviour varies with different input conditions. Their characteristics are current-density dependent and frequency dependent. The electrical impedance varies at different frequencies. Modelling electrode behaviour with an equivalent circuit can help towards better understanding of electrode characteristics. Fig. 2.1 shows the equivalent electrical circuit for a biopotential electrode in contact with an electrolyte. The circuit model is a combination of a voltage source representing the half-cell potential with some resistive components in series associated with the electrode-electrolyte interface and the electrolyte itself.

This electrode-electrolyte model is constructed from several distinct components. R_d and C_d refer to the resistive and capacitive components of the double layer formed at the electrode-electrolyte interface, respectively. E_{hc} represents what is known as *half-cell potential*, the electrochemical potential difference between an electrode and its corresponding electrolyte. A half-cell is a single electrode immersed in a solution containing its ions, and the half-cell potential is a measure of the tendency of a particular electrode to undergo a reduction or oxidation reaction.

2.2. Electrochemical characterization methods

The common techniques for electrochemical characterization of neural electrodes are impedance spectroscopy, cyclic voltammetry (CV) and voltage transients (VT).

2.2.1. Electrochemical Impedance Spectroscopy

Electrochemical impedance spectroscopy (EIS) involves measuring electrical impedance and phase angle in response to sinusoidal voltage or current excitation across a wide frequency range (typically $< 1Hz$ to 10^5Hz). The electrode to be characterized, analogous to the working electrode (WE), is immersed into an electrolyte solution which contains the ground, counter electrode (CE), as illustrated in Fig. 2.2 a. It should be noted that CE is much larger in size than the microelectrode to be characterized, in this way, CE impedance contribution is minimal. The reference electrode (RE) provides a stable potential for accurate measurement. The impedance (Z) of the electrode is deduced by comparing the amplitude and phase of the input signal with the output signal [23]. An input sinusoidal signal with a range of frequencies is applied and a spectrum of impedances is obtained, which is then represented in a bode plot.

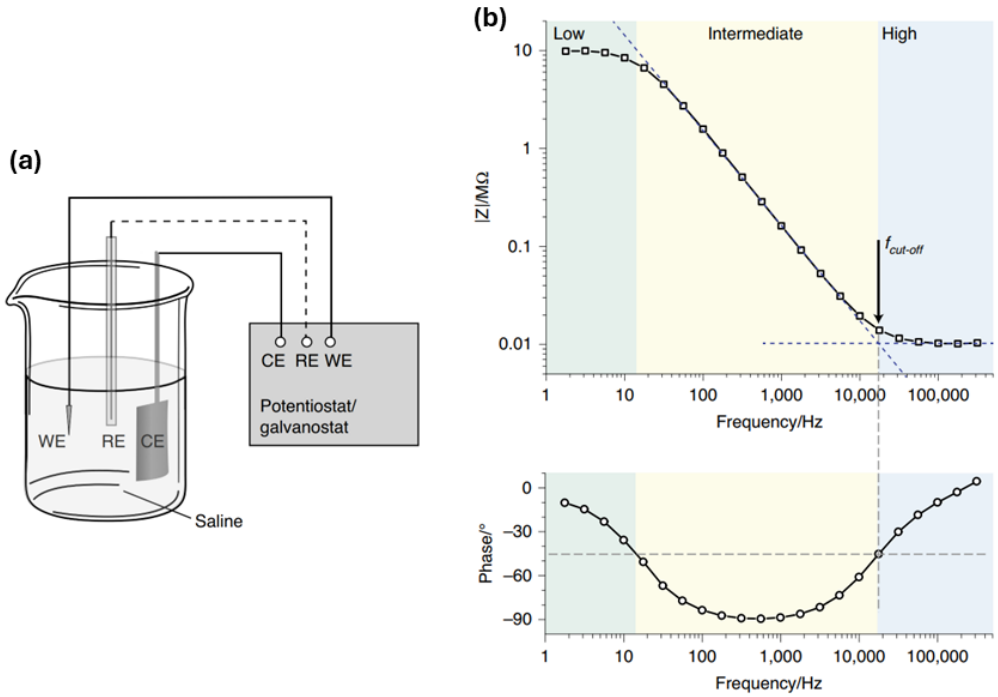

Figure 2.2: (a) Three-electrode setup consisting of a working electrode (WE), counter electrode (CE) and a reference electrode (RE). **(b)** A typical EIS bode plot of a metal-electrode. The amplitude (top graph) and phase shift (bottom graph) over a wide range of frequencies, from 1 to $10^5 Hz$, are shown.

A typical bode plot for a metal electrode is depicted in Fig. 2.2 b. The main contributor to the variation of impedance is the double-layer capacitance (denoted by C_d in the equivalent circuit model, Fig. 2.1). Note that at higher frequencies (Fig. 2.2 b, blue zone) the current passes smoothly through the electrode-electrolyte interface, almost with no opposition. This reveals that the impact of C_d is almost negligible and that the measured impedance mainly depends on the electrolyte resistance (denoted as R_s in the equivalent circuit model, Fig. 2.1). In intermediate frequencies (Fig. 2.2 b, yellow zone), the impedance of the double-layer capacitor, C_d, increases in a logarithmic manner with higher frequencies, and there is a 90º phase shift. Over the low frequency range (Fig. 2.2 b, green zone), the high impedance values hinder the current passage through the electrode-electrolyte interface due to the substantial increase in the impedance contribution of C_d. As observed in the example, at low frequencies there is no phase shift, indicating that the total impedance is governed by the R_d and R_s in series. Consequently, to drive current within this frequency range, higher voltages would be required, which are associated with increased energy demand and higher probability of damaging the electrodes or target tissue.

Impedance spectroscopy serves a dual purpose by examining both tissue and electrode properties. By estimating the resistive contribution of tissue conductivity at high frequencies, where the impact of charge transfer at the electrode-tissue interface is minimal, valuable insights into the electrode's behaviour are gained [24].

2.2.2. Cyclic Voltammetry

Cyclic voltammetry (CV) is a standard technique for electrochemical surface analysis. During this test, the potential in the working electrode is swept cyclically between two potentials limits, also referred as the *potential window* or *water window*, and the current flow is monitored. The current flow is driven by (1) faradaic processes, originating from the transfer of electrons through oxidation and reduction reactions and by (2) capacitive processes, resulted from the redistribution of chemical species which store charge at a double layer [25, 26].

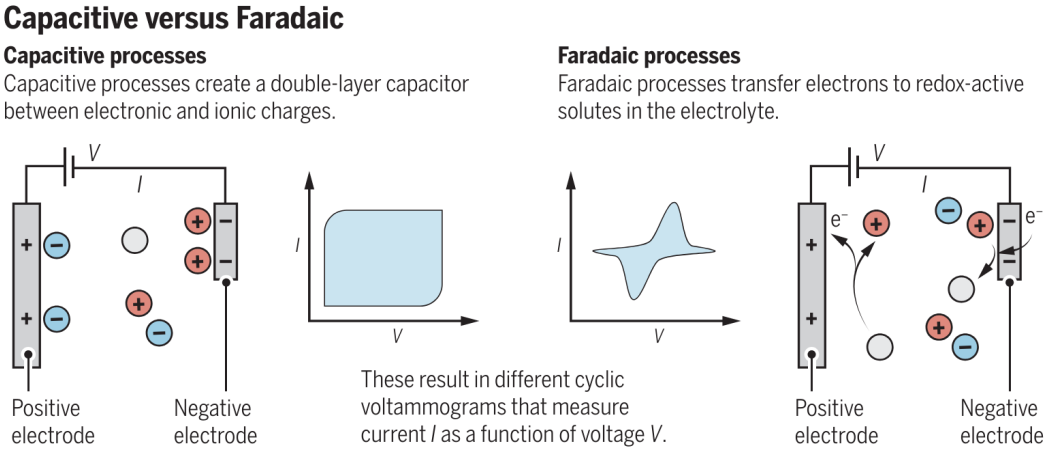

Figure 2.3: Capacitive versus Faradaic processes occurring when an external voltage is applied to a working electrode immersed on an electrolyte during a cyclic voltammetry (CV) measurement. Image taken from [26]. Electrodes with high ionic conductivity exhibit a dominant capacitive behaviour translating into a box-shaped cyclic voltammogram. In contrast, the current flow of electrodes with lower specific capacitance values is dominated by Faradaic processes, resulting in a limited charge storage capacity, and their CV curve typically shows distinct peaks.

Usually in a metal/electrolyte interface a combination of faradaic and capacitive processes are measured. The capacitive behaviour is mainly determined by specific capacitance intrinsic to the material. In case of graphene, its specific capacitance is reported to be $3\mu F/cm^2$ [27] independent on the number of layers (up to 5 layers). When driving the potential further from equilibrium, faradaic currents become more dominant and if they exceed the water window, the redox reactions become irreversible. The water window is defined as the potential range were electrolysis, irreversible reactions, does not occur. From the CV curve, the charge storage capacity (CSC) can be obtained, which is an electrode quality metric relevant for stimulation that represents the amount of charge that can be stored reversibly in an electrode [25]. CSC [$\mu C/cm^2$] can be calculated based on the area under the CV curve divided by the scan rate [V/s], and normalized to the electrode area.

2.3. Graphene potential as neural interface

Graphene, a single layer of carbon atoms arranged in a two-dimensional honeycomb lattice, has emerged as a promising material for neural interfaces due to its unique combination of electrical, mechanical, and biocompatible properties, as well as offering optical transparency [28, 29, 30]. Graphene is a zero-gap semimetal material [31], meaning that the conduction band and the valence band intersect at the Dirac point (i.e., absence of bandgap). As a result, both electrons and holes can act as charge carriers leading to increased electronic conductivity. Graphene, additionally, exhibits high charge carrier mobility at room temperature [32]. However, the quality of graphene and the substrate that it is used greatly affect its electronic properties. To make it a competitive candidate among conventional metals, graphene´s electronic conductivity could be further improved by chemically doping (with electrons or holes) [31]. The electrical conductivity of graphene facilitates signal transduction, making it a good candidate for the design of electrical tracks. This few atoms thick material also exhibits mechanical flexibility, which allows it to conform closely to the complex geometries of neural tissues, reducing the mechanical mismatch and potential tissue damage during long-term implantation. Furthermore, the biocompatibility of graphene, while initially controversial, has shown promising results in more recent studies. Particularly graphene produced by chemical vapor deposition (CVD), has shown no significant signs of toxicity, supporting its use in chronic neural interfacing applications [33].

Moreover, graphene's optical transparency broadens its application in multimodal neural interfaces that integrate both electrical recording and optical imaging or stimulation. This unique property is particularly advantageous in optogenetics, where precise control and monitoring of neuronal activity via light-sensitive proteins is required. Advances in graphene fabrication techniques, such as chemical vapor deposition (CVD), have also improved the scalability and reproducibility of graphene-based devices.

Additionally, graphene can undergo various material functionalization techniques, such as chemical doping to improve conductivity or integration with other materials (e.g., platinum nanoparticles, conductive polymers) to enhance its electrochemical performance. Consequently, graphene stands out as a versatile and powerful material for next-generation neural interfaces, promising significant advancements in both fundamental neuroscience research and bioelectronic medicine.

2.4. State-of-the-art graphene electrode arrays

Recently, D.-W. Park et al. [34] explored the usability of graphene microelectrodes for optogenetic applications. Authors demonstrated that graphene microelectrode device can be implanted on the brain surface in rodents for high-resolution neurophysiological recording. The authors also showed that due to graphene's broad spectrum transparency, it is an excellent candidate for applications requiring a wide range of wavelengths (from ultraviolet to infrared). These applications include neural imaging and optogenetics, where there is the need of stimulating various opsin types and visualizing different fluorescent dyes bonded in cells (note that the excitation light wavelength varies depending on the optical imaging technique, whether confocal microscopy or 2P microscopy). The same authors published a detailed protocol, [35], describing the fabrication process of their graphene-based micro-electrocorticography (µECoG) electrode array and its usage alongside electrophysiology, fluorescence microscopy and optogenetics. Moreover, Park et al., as a continuation of their work, also studied the neural stimulation capability of the electrodes in combination with optical monitoring in transgenic GCaMP6f mice model [36]. The capacitive four-layer graphene electrodes were characterized to deliver a charge density of 116.07-174.10 $\mu C/cm^2$ through the tissue (with a stimulation current of 100−150 μA). Higher stimulation currents resulted in electrode damage, being limited by the initial condition of the graphene layer (number of defects). Even so, the reported current density values were within the documented limits for safely activating tissue [37].

In D. Kuzum et al. [38], authors present graphene microelectrodes on flexible polyimide (Kapton) substrate. The array was tested for *in vivo* electrocorticography recording and *in vitro* hippocampal slice recording. With an electrode area of 50 × 50 μm^2, approximately ten neuronal cell bodies were shown to be overlapping with the electrode area. The electrode recordings were combined with calcium imaging (with confocal microscopy and 2P imaging techniques) to benefit from the spatial and temporal resolution of both modalities. Years later, the same authors demonstrated that the electrodeposition of platinum nanoparticles (Pt NPs) on graphene electrodes significantly reduces the electrical impedance. However, a trade-off was observed between impedance reduction and optical transparency. While the impedance decreased by a factor of 100, the transparency dropped from over 90 % to 50 %, a reduction that may be acceptable for certain experimental applications [39]. Pt NPs provide a parallel conduction path and help to overcome the inherent limiting quantum capacitance of graphene. The PtNP/graphene microelectrodes were tested in a transgenic mice model, successfully combining 2P imaging and cortical potential (µECoG) recordings. A follow-up paper of the same authors, [40], presents a PtNP/graphene microelectrode array with decreased dimensions up to single-cell (i.e., electrode diameter of 20 μm) and ultra-high density (i.e., arrays up to 256 channels) for increased spatial resolution. The study proposes a novel material architecture: interlayer-doped double-layer graphene with deposited Pt NPs. The Pt NPs substantially lowered electrode impedance, while the interlayer-doped double-layer graphene provided high-conductivity transparent wiring. This design ensured full transparency of the array and counteracted graphene's relatively high sheet resistivity (compared to other metals), while also making it less susceptible to defects during fabrication and processing. The authors reported low impedance values at 1 kHz, in the range of 300 $k\Omega$ (for 20 μm electrode diameter).

Graphene has also been explored as an ideal candidate for fabricating field-effect transistor (FET) arrays for providing an excellent interface with neural cells with higher signal-to-noise (SNR) ratio. Hébert et al. [41] introduced a flexible graphene solution-gated field-effect transistors (gSGFET) consisting of a single-layer graphene channel connected by two metallic contacts (i.e., drain and source). The proposed gSGFETs were immersed into an electrolyte solution where the gate voltage was modulated by an external reference electrode. The authors demonstrated a high sensitivity for the detection of local field potential (LFP) because of the local preamplification that is inherent to the transistor configuration.

Specifically, they reported an intrinsic gate noise level of 20 μV RMS, which is far below the LFP amplitude recorded at the cortex surface. Graphene microtransistor technology can be further exploited by selectively functionalizing the transistors to monitor relevant neural biomarkers for brain diseases. The same authors, in a recent publication [42], functionalized gSGFET by directly immobilizing chemically modified aptamers bioreceptors on the graphene surface for biosensing applications.

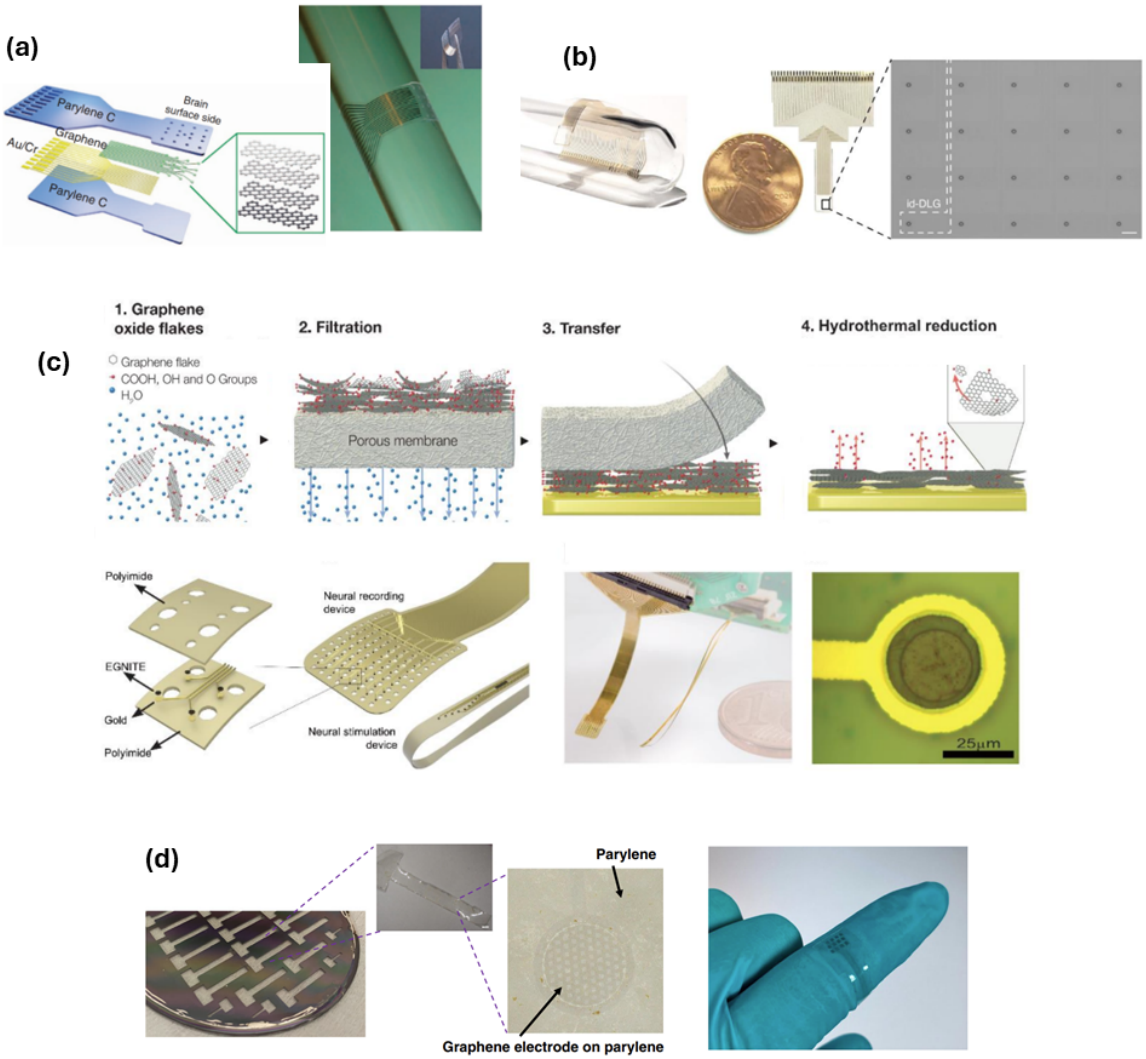

Figure 2.4: State-of-the-art graphene-based electrode technologies for neural interfaces. (a) Graphene-based transparent electrode array showing the different stacked layers and its mechanical flexibility from Park et al. [34]. **(b)** High-density transparent and flexible PtNP/graphene microelectrode array proposed by Ramezani et al. 2024 [40]. It consists of a 64-channel array with an electrode dimension of 20 μm of diameter. The scale bar is 100 μm. A reduced electrode impedance was achieved through an interlayer doped double layer graphene (id-DLG) configuration. **(c)** Nanoporous graphene-based thin-film microelectrodes presented by Viana et al. [43]. Hydrothermal reduction was used to create nanometre-scale pores that form capillarities between graphene flakes. The porous configuration increases the volumetric surface area and resulted lower impedance values and higher charge injection capacity was demonstrated. **(d)** Multilayer CVD graphene electrodes using a wafer-scale transfer-free process from Babaroud et al. work [18]. A method to grow graphene avoiding the manual transfer of pre-grown sheets is presented, resulting in higher reproducibility, higher yield, and greater compatibility with conventional wafer-scale processes.

For bidirectional neural interfaces (i.e., recording and stimulating), Viana et al. [43] proposed a reduced graphene oxide (rGO) thin film with a nanoporous nature. The focus of this graphene technology

	Graphene technology	**Substrate**	**Channel count**	**Electrode area** (μm^2)	**Impedance @1KHz** ($k\Omega$)	**Area-normalized impedance** ($\Omega \cdot cm^2$)	**CSC** ($\mu C/cm^2$)	**Water window**	**CIC** ($\mu C/cm^2$)	**SNR** (dB)	**Biological test**
Park et al. 2018 [36]	Four-layer graphene	Parylene-C	16	7854 (D=100) 17671 (D=150) 31416 (D=200)	286.4 $\pm$ 92.6 248.7 $\pm$ 125.0 215.7 $\pm$ 120.4	22.49 $\pm$ 7.27 43.95 $\pm$ 22.09 67.76 $\pm$ 37.82	*cathodic:* 87.8 (*v*: 1 V/s)	-0.6 to 0.8 V	57.13	-	*In vivo* neural electrical stimulation combined with optical imaging (fluorescence microscopy)
Ramezani et al. 2024 [40]	PtNP/graphene (interlayer-doped double layer)	Parylene-C	256	314 (D=20)	250 $\pm$ 56	0.78 $\pm$ 0.18	*total:* 30720 (*v*: not specified)	-1 to 1 V	-	-	High-density *in vivo* neural recording (cortical potentials) and 2P calcium imaging
Viana et al. 2024 [43]	EGNITE: porous reduced graphene oxide (rGO)	Polyimide	64	491 (D=25)	26.8 $\pm$ 4.7	0.13 $\pm$ 0.02	*cathodic:* 33700 *anodic:* 27600 (*v*: 0.1 V/s)	-0.9 to 0.8 V	2800	40 at 10Hz 5 at 1Hz	*In vivo* neural recording (epicortical and intracortical) and stimulation (in sciatic nerve)
Duvan et al. 2024 [44]	EGNITE: porous reduced graphene oxide (rGO)	Borosilicate glass	60	491 (D=25) 1962 (D=50) 7850 (D=100)	27.6 $\pm$ 2.97 11.9 $\pm$ 0.44 6.37 $\pm$ 0.43	0.14 $\pm$ 0.015 0.23 $\pm$ 0.009 0.50 $\pm$ 0.034	38440 $\pm$ 7160 18920 $\pm$ 1850 11780 $\pm$ 1410 *cathodic* (*v*: 0.05 V/s)	-0.9 to 0.8 V	3940 1960 1550	24.74 $\pm$ 2.52 24.36 $\pm$ 1.16 23.02 $\pm$ 0.56	*In vitro* MEA recording and stimulation of hippocampal neuronal culture and explanted retinal tissue
Driscoll et al. 2021 [45]	Two-layer graphene doped with HNO_3	Parylene-C	16	2500 (50 x 50)	908 $\pm$ 488	22.70 $\pm$ 12.20	*cathodic:* 22.4 (*v*: 0.5 V/s)	-0.8 to 0.8 V	-	> 5	*In vivo* neural recording and optical imaging (calcium epifluorescence imaging)
Körbitzer et al. 2019 [46]	Few layers graphene	Borosilicate glass	59	707 (D=30)	2300	16.26	*total:* 910 (*v*: 1 V/s)	-1.4 to 1.6 V	150	35.8	MEA for cortical rat neurons culturing
Kshirsagar et al. 2018 [47]	Monolayer graphene/PEDOT:PSS (1s electropolymerization)	Borosilicate glass	9	707 (D=30)	166 $\pm$ 13	1.17 $\pm$ 0.09	-	-	-	-	*In vitro* MEA recording of cardiac field potentials and optical imaging
Babaroud et al. 2022 [18]	Transfer-free multilayer CVD graphene	Parylene-C	4	68320 (D=340)	27.4 $\pm$ 7.5	18.72 $\pm$ 5.12	*total:* 3549 *cathodic:* 2151 (*v*: 0.1 V/s)	-0.8 to 0.6 V	44	-	-
Babaroud et al. 2023 [48]	Transfer-free multilayer CVD graphene with 40% Pt NPs	Parylene-C	4	68320 (D=340)	7.26 $\pm$ 0.95	4.96 $\pm$ 0.61	*total:* 4365 *cathodic:* 3614 (*v*: 0.1 V/s)	-0.6 to 0.6 V	30.6 $\pm$ 1.8	-	-

Table 2.1: Current state-of-the-art graphene based electrode arrays. CSC, *v* and CIC stands for charge storage capacity, scan rate and charge injection capacity.

was not on optical transparency, but rather on developing a material for efficient neural interfacing. The porous configuration increases the volumetric surface area and results in lower impedance values (for recording) and higher charge injection capacity, CIC, (for stimulation). The film of stacked GO flakes deposited onto a conductive substrate are hydrothermally reduced to exhibit superior electrical properties. With electrodes size of 25 μm diameter (array consisting of 64 channels arranged in 8 x 8 grid), characterization tests showed very low electrical impedance around 26.8 $k\Omega$ @1kHz and CIC around 2.8 mC/m^2 for 1 ms pulses. Moreover, authors conducted *in vivo* testing with the proposed flexible µECoG devices for recording (epicortical and intracortical) and stimulation (in the sciatic nerve) applications. In the epicortical recordings, the microelectrodes exhibited very low intrinsic noise, thus high SNR (of 40 dB at 10 Hz and 5 dB at 1 kHz), allowing highly sensitive registration of cortical potentials with high spatial resolution.

2.5. Transfer-free multilayer graphene technology

High quality graphene can be grown by chemical vapour deposition (CVD) process. The mechanism of growth typically requires high temperatures (900-1000 ºC) for the carbon source (i.e., CH_4) to decompose into various radicals. Some of these carbon radicals travel to the catalyst surface, react with it and nucleate into graphene. If the growth time is sufficiently high, a continuous graphene layer will be formed. The quality of graphene is determined by several factors including growth conditions (time, temperature, pressure, gas flow rates), substrate type, cleanliness and morphology, among others. Current state-of-the-art graphene electrodes fabrication approaches focus on growing monolayer graphene on metal foil substrates or thin-films (i.e., copper, nickel) by CVD method and subsequently, transferring the graphene sheet to the substrate of interest [36, 38, 45, 46]. This process is especially crucial as substrates containing polymers are unable to withstand the high temperatures required in the CVD process. Although transferring graphene to the substrate of interest is a standard procedure in the field, it remains the most critical step due to its susceptibility to cause potential graphene film degradation by introducing damage, polymer contamination, cracks and wrinkles [49]. Moreover, it potentially affects the reproducibility and limits large-scale wafer processing.

Recently, researchers from TU Delft have been working in developing wafer-scale transfer-free multilayer graphene electrodes which can be coupled with flexible substrates [18]. The transfer-free approach uses a sputtered molybdenum (Mo) layer as the catalyst for graphene growth. This allows to grow multi-layer graphene avoiding the complications from the numerous transfer steps while demonstrating an increase in its charge storage capacity (CSC) for stimulation purposes. Additionally, the transfer-free microfabrication method provides higher reproducibility, higher yield, and greater compatibility with conventional wafer-scale processes. A follow-up paper from the same authors, [48], proposes a surface functionalization strategy with Platinum (Pt) nanoparticles (NPs) for improved performance (reduced impedance, higher charge injection capacity (CIC)) of the graphene electrodes.

2.6. Surface modification

Graphene has shown to be a promising candidate for multimodal neural interfaces, permitting the combination of optical and electrical techniques. The ideal neural recording and stimulation electrodes should have high sensitivity, high selectivity, low impedance, good biocompatibility, high charge injection capacity and long-term stable neural recording [30, 50]. Graphene, however, suffers from low sheet conductivity and large impedance limited by quantum capacitance (compared to conventional metals), originating from its low density of states [39]. Impedance is the major bottleneck of neural electrodes which limits scaling down the electrode dimensions towards single-cell neural activity detection. This is because as the electrode size decreases, its electrical impedance goes up due to a higher thermal noise [30], which in turn results in a lower signal-to-noise (SNR) ratio (i.e., a lower sensitivity).

Some strategies to lower the electrical impedance of graphene electrodes include chemical doping and surface modification. Chemical doping has been shown to reduce graphene's sheet resistance to some extend [51, 52]. However, a more recent study, [39], suggests that the reduction in electrical impedance by chemical doping is not enough to scale down the electrode dimensions to single-cell resolution. Instead, electrodeposition of platinum (Pt) nanoparticles (NPs) on graphene electrodes seems

to be a better choice based on a study which showed a 100 times impedance reduction while maintaining optical transparency (values above 50 %). Yet, the long-term stability and adhesion of graphene/Pt NPs electrodes were not investigated in the aforementioned work. Babaroud et al. [48] also presented a method to spark ablate Pt NPs on graphene surface demonstrating a 4.5 times lower impedance with 40% NP print surface density. Even though authors performed some electrochemical and mechanical tests to study the stability, test samples instead of the final flexible electrodes were used, making it more difficult to obtain conclusive results on the long-term adhesion and stability of the NP coating. Even though the described spark ablation technique has limited scalability, it is much more controllable compared to electrodeposition which highly depends on the homogeneity of the material layers.

2.6.1. PEDOT:PSS coating

Conductive polymers, such as poly(3,4-ethylenedioxythiophene) doped with poly(styrene sulfonate) (PEDOT:PSS), have the potential to elevate the performance of neural electrodes by increasing the volumetric surface area and thus, lowering the impedance. PEDOT:PSS is widely used in the field of organic electronics due to its tunable conductivity, easy processing and commercial availability. Particularly, it exhibits high electronic and ionic conductivity, which enhances the electrochemical interactions in the electrode-electrolyte interface, thus being a more efficient electronic transducer of neural signals [53]. Electronic conductivity values up to 2500 S/cm have been reported previously in literature [54], which are far below the values for metallic conductors (in the order of 10^6 to 10^8). However, due to its volumetric architecture, as illustrated in Fig. 2.5, it presents high charge capacitance values, which greatly reduces the impedance. Other advantageous properties that have made it an attractive material for organic bioelectronic devices are its high transparency in the visible range, good film-forming properties, mechanical compliance to the biological tissues and biocompatibility [55, 53]. PEDOT:PSS has been investigated as a conductive coating for metal (gold) electrodes [56, 57] to further reduce the impedance and improve the recording and stimulation capabilities. However, the integration of PEDOT:PSS with graphene for transparent neural interfaces remains relatively unexplored.

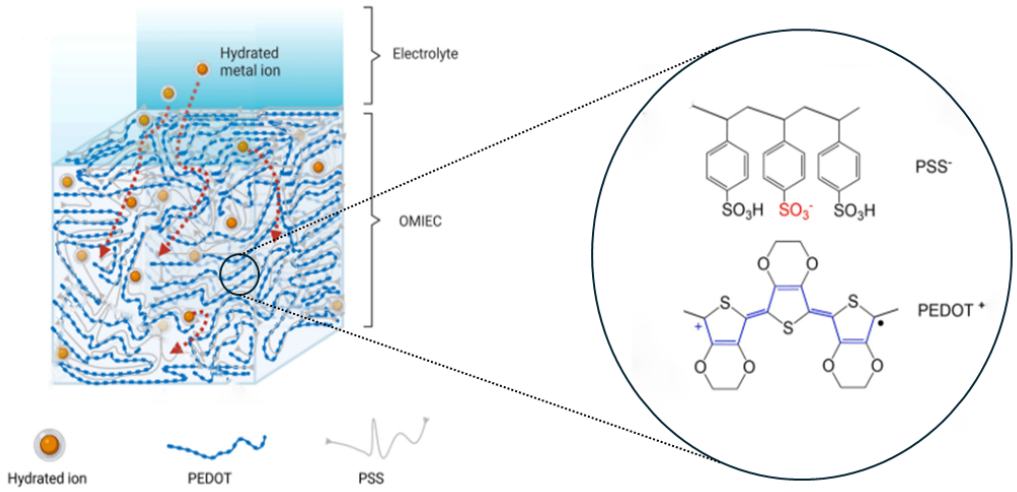

Figure 2.5: PEDOT:PSS film interface with an electrolyte solution. OMIEC: organic mixed ionic and electronic conductors. PEDOT:PSS conductive polymer exhibits high ionic and electronic conductivity, acting as a volumetric capacitor. Image taken from [53].

A study on PEDOT:PSS electrodeposition in graphene microelectrodes, with 30 µm in diameter, was shown to reduce their impedance from 2.9 $M\Omega$ to 166 $k\Omega$ while presenting transparencies of 84 %, and their application with optical imaging and electrophysiology was demonstrated [47]. However, the study highlights several limitations: uncontrolled wrinkles in graphene were observed and run-to-run variability of graphene quality was mentioned, which might be caused by the graphene transfer process. Additionally, despite the optical transparency of the microelectrodes, the presence of gold tracks within the field of view obstructs the visualization of adjacent fluorescent cells and generates photo-induced

artifacts due to the photosensitivity of gold. Furthermore, the study did not assess the charge storage capacity (CSC) or conduct cyclic voltammetry characterization, which could have demonstrated the high charge capacitance attributed to the volumetric architecture of PEDOT:PSS as supported by existing literature. This reveals that further research is needed to understand the combined behaviour of these two materials and their potential application for multimodal neural interfaces.

2.7. Polymeric encapsulation

Conformable polymer-based organic layers have been considered very adequate encapsulant materials for neural implants due to their favourable mechanical flexibility, reduced mechanical mismatch with the neural tissue, and their biocompatibility [58]. Among them, parylene C provides a highly flexible barrier which can be vapor-deposited onto the electrode forming a thin (< 100 μm) and uniform layer with a pinhole-free surface [59]. Various studies have reported the usage of parylene as the encapsulant layer for graphene-based neural electrodes [34, 35, 36, 45, 40]. Even though no polymer is a perfect water barrier, parylene exhibits a lower permeability to water vapor and moisture. While organic polymer layers present increased conformability and flexibility, their water vapor transmission rate (WVTR) characteristics, ion permeability and adhesion capability to noble metals remain a critical aspect.

Delamination during long-term use is one of the most frequent failure mechanisms in thin-film electrodes, either between encapsulation-metallisation layers or between metallisation-electrode surface layers [60]. Delamination occurs as a consequence of the poor adhesion of polymers to inorganic metallisation tracks. Polymer-based encapsulation materials are selected due to their chemical inertness; however, this results in the lack of ability to form compounds with the metal atoms which entails reduced adhesion to the metallisation layer [61]. To our knowledge, no studies have investigated the long-term adhesion of polymeric encapsulants to a graphene substrate.

Oxygen plasma surface treatments have been proposed to address this issue [62, 63]. Plasma treatments activate the surface by increasing its energy and thus, improve the adhesion strength between thin-films. The big downside is that plasma, especially oxygen plasma, will damage or etch the graphene layer, thus hindering its integration for graphene-based devices. Alternatively, adhesion promoters have also been investigated for improved adhesion strength due to their ability to form chemical bonds between the polymer and metallization layer [60]. Silane A-174 is the most investigated one for parylene. However, according to literature [64], effective coupling between gold surface and parylene with silane has not been realized yet. Instead, thiol-containing adhesion promoters such as 2-methylthio ethyl methacrylate and 4-chlorothiophenol demonstrated positive results after pull tests.

In the light of the limited long-term endurance of these coatings, Kim et al. [65] proposed a multilayer architecture consisting of hybrid organic/inorganic barriers for optimal encapsulation. By combining ALD Al_2O_3-TiO_2 and CVD parylene C in a single chamber at low temperature, the advantages from both approaches are synergized, thus providing a balance between hermeticity and flexibility, without compromising its biocompatibility and miniaturization. Authors achieve a higher quality barrier with extended lifetime even after cracking thanks to the multilayer design, which supports random partial cracks while preventing all-through cracking under mechanical strain.

2.8. Biological Characterization

Various *in vitro* and *ex vivo* models are essential for studying neural interface technology, circumventing the limitations of *in vivo* studies [66]. Among these, brain slice cultures are particularly valuable as they preserve the brain's native cytoarchitecture and neuronal networks. Typically derived from rodent brains, these organotypic cultures allow for detailed neurophysiological investigations and material testing. Despite some limitations, such as the absence of a blood-brain barrier and circulating immune cells, brain slice cultures provide a reproducible platform for high-throughput screenings and long-term biocompatibility assessments, making them an invaluable model for advancing microelectrode research [66].

2.8.1. Biocompatibility

Biocompatibility is crucial for the successful integration of microelectrodes technologies with brain tissue. To ensure long-term functionality and minimal adverse effects, the constituent materials of these microelectrodes must be non-toxic to neural cells and should not provoke adverse reactions, also known as foreign body response, in the surrounding tissues. Moreover, in order to avoid fibrotic encapsulation, a common failure cause of long-term implants, the microelectrode surface has to mimic the physicochemical and mechanical characteristics of the extracellular matrix (ECM) to promote neuronal development, property known as *biomimicry*. Furthermore, the microelectrode materials must maintain their physical integrity and electrochemical stability in the highly corrosive environment of body fluids and tissues, property known as *biostability* [66]. Achieving such biocompatibility and biostability is essential to prevent the formation of insulating glial scars and to preserve the electrochemical performance of microelectrode platforms during long-term use.

The biocompatibility of graphene has been previously studied by means of direct cell-to-graphene interfaces [67, 68, 69, 70]. In [69], monolayer CVD graphene substrate was compared with glass substrates for human neural stem cell (hNSC) cultures, in terms of cellular survival rates and coexistence with a biomaterial. Results showed that graphene provides a favourable microenvironment for enhanced cellular adhesion on the surface and hNSC differentiation into neurons. Moreover, it has been shown that graphene-based substrates do not alter neural cell and synaptic behaviour [70]. Given the importance of biocompatibility, graphene seems to be a promising material for the development of neural interfaces.

2.8.2. SNR ratio

A good understanding of the origin of microelectrode noise is necessary to optimize electrodes design towards high sensitivity recordings, able to detect small extracellular potentials. Various noise sources, both intrinsic and extrinsic, can impact the quality of electrophysiological recordings and the signal-to-noise ratio (SNR) [21]:

- Thermal noise: also known as Johnson-Nyquist noise, it generates from the random motion of charge carriers within the electrode material. It is the dominant intrinsic noise of microelectrodes. Thermal noise can be mathematically calculated by the following expression:

$$v_t = [4k_B T \int_{f_1}^{f_2} Re(Z)\, df]^{1/2}$$

  where k_B represents Boltzmann constant, T temperature, $Re(Z)$ the real part of electrode impedance, and f_1 to f_2 is the selected recording bandwidth. The expression shows a positive correlation between the impedance and noise of microelectrodes. Narrowing the bandwidth to the frequency range of interest is desirable to further minimize the thermal noise. Notably, neural cells produce local field potentials (LFPs) at low frequencies (< 300 Hz) and action potentials at higher frequencies (500 – 1500 Hz) [71].
- Biological noise: it is originated from the activity contribution of more distant neurons that is picked up by the recording electrode. It depends on the density and the firing rates of neurons nearby the recording electrode. Spike sorting algorithms aim at identifying individual cells based on the recorded activity patterns, by feature extraction and clustering computational techniques.
- Instrumentation noise: it comes from the recording hardware (e.g., amplifiers, DAQs). In case of the RHD2000 amplifier chips, they exhibit a low noise floor around 2.4 μV rms.
- Interference: it is resulted from external sources such as power lines and nearby equipments. Typically, the commonly known 50 or 60 Hz interference are filtered out from the recordings.
- Shot noise: at low currents, stochastic variations in the number of charge carriers might occur, known as shot noise. It is not, however, very significant in microelectrode recordings.
- Flicker noise: it is the noise inversely proportional to the frequency ($1/f$) noise. It is possible to remove it with a high-pass filter.

From the described noise sources, thermal noise and biological noise are typically the dominant ones in electrophysiological recordings with multielectrode arrays. The combined effect of these noise sources will determine the signal-to-noise ratio (SNR) of the microelectrodes during action potential recordings. The SNR can be calculated with the equation below:

$$SNR = (\frac{A_{peak}}{\sigma_{noise}})^2$$

, where A_{peak} is the signal amplitude and the σ_{noise} the standard deviation of noise. As for the noise estimation, a graphene MEA without neural cells (but with the culture medium) could be used.

2.9. Summary

In conclusion, microelectrode arrays (MEAs) represent a powerful tool for interfacing with biological tissue, enabling the simultaneous electrophysiological recording of multiple neuronal cells with high spatiotemporal resolution. Traditional MEAs, typically fabricated using materials such as gold and platinum, exhibit limitations in their compatibility with multimodal applications, particularly with respect to their integration with optical imaging methods commonly employed in neuroscience. Consequently, recent efforts have focused on the development of novel materials that provide optical transparency alongside favorable electrochemical properties for efficient neural interfacing. Among these, graphene has emerged as a promising candidate for multimodal neural interfaces.

State-of-the-art graphene-based electrode arrays have successfully demonstrated the integration of electrical recordings with two-photon (2P) imaging techniques, offering a versatile platform for neural investigations. Recent advancements have further scaled down graphene electrode dimensions to achieve single-cell resolution through surface modifications, such as the incorporation of platinum nanoparticles (Pt NPs), which significantly reduce impedance. In addition, chemical doping of graphene has been shown to lower its sheet resistance, thereby enhancing its suitability for use in conductive tracks and enabling the development of fully transparent electrodes. However, all these studies have in common the necessity of transferring graphene sheets from their initial substrate to the final device substrate, introducing a critical step in the fabrication process that may compromise device performance.

To address this challenge, researchers at TU Delft have developed a wafer-scale, transfer-free technology for fabricating multilayer graphene electrodes, thus eliminating the risks associated with the transfer process. Despite these advances, the inherent impedance of graphene, governed by its double-layer capacitance, continues to limit further miniaturization of the electrodes. Although platinum nanoparticle modifications have been explored to address this limitation, further research is required to assess the long-term stability and adhesion of these nanoparticles, as well as bringing this technology to *in vitro* or *in vivo* tests.

Conductive polymers, such as PEDOT:PSS, offer a promising alternative due to their ability to function as volumetric capacitors, exhibiting high ionic and electrical conductivity. However, the integration of PEDOT:PSS with graphene electrodes has been relatively unexplored.

This current work presents the design and fabrication of graphene *in vitro* MEAs on transparent substrates. Several electrode diameters, ranging from 10 µm to 500 µm, were included to accommodate different experimental requirements and test the limits of the technology. This work has a strong focus on process development, establishing optimized microfabrication procedures for the integration of transfer-free multilayer graphene technology on *in vitro* MEAs. Moreover, a technique to integrate patterned PEDOT:PSS polymer coating on the electrodes is introduced, enabling the exploration of hybrid graphene/PEDOT interfaces for more efficient neural interfacing platforms. The electrochemical performance of graphene electrodes and graphene/PEDOT:PSS electrodes was thoroughly assessed. Finally, the fabricated MEA devices were tested with brain slices to validate their electrophysiological recording capabilities. This work aims to advance the development of graphene-based neural interfaces, offering insights into improved fabrication techniques and material combinations for more effective neural recording platforms.

3

Device design

In this chapter, the architecture and material layers of microelectrode arrays (MEAs) are explored, focusing on the design considerations necessary for achieving optically transparent devices for multimodal neural application. The encountered technological challenges in developing high-density electrode arrays, the strategies employed to mitigate these challenges, and the selection of materials are discussed. Additionally, insights into the design of photolithography masks that enable precise patterning of the various material layers are provided.

3.1. MEA device architecture and material layers

In order to achieve an optically transparent MEA device with superior recording capabilities (i.e., high sensitivity, high selectivity and low impedance), thoughtful material and design choices will be considered, as well as the requirements for its validation in brain slice recording test in collaboration with the Neuroscience Department in Erasmus MC. Detailed information regarding the slice activity recording test is provided in section 6.2.

For effective microelectrode array (MEA) design, achieving a large cover area, referring to the spatial extent needed to capture diverse neural activity, and a high-density electrode array are essential. The epifluorescence upright microscope with a patch clamp slice recording setup available at Erasmus MC, which will be used for validating the microfabricated MEAs, features a 0.6 mm diameter field of view with a x40 objective. Therefore, the electrode array layout should be designed to densely cover this area. However, creating a large coverage and high-density array presents several technological challenges. The interconnection tracks connecting each microelectrode to the external contact pads, referred to as routing, become complex, as it is crucial to ensure sufficient track width to avoid compromising total resistance and potentially impacting the signal-to-noise ratio (SNR). Additionally, since microfabrication is a two-dimensional technology, track design is limited to a single layer, leading to potential issues with lack of physical space and electrical crosstalk. To address these challenges, several electrode arrays with varying electrode sizes, numbers of electrodes, and pitches were designed to meet different experimental requirements and explore the limits of the technology.

Regarding the materials, graphene was the chosen material for the microelectrodes and inner tracks. In contrast to traditional metal microwires, graphene exhibits a relatively high sheet resistance. In order to mitigate this characteristic, one approach involves minimizing the length of the graphene intermediate tracks. This entails confining the graphene within the designated field of view, while concurrently forming the out-of-field tracks using highly conductive and biocompatible metals. Gold, with a thin adhesion layer of titanium, was the chosen metal for the outer tracks and contact pads.

The final envisioned MEA, shown in Fig. 3.1, will consist of a graphene layer defining the microelectrodes and inner tracks resting on a quartz substrate and connecting to the Ti/Au outer tracks and contact pads. The MEA will be encapsulated by a parylene-C layer on the frontside with dedicated openings in the electrodes and contact pads.

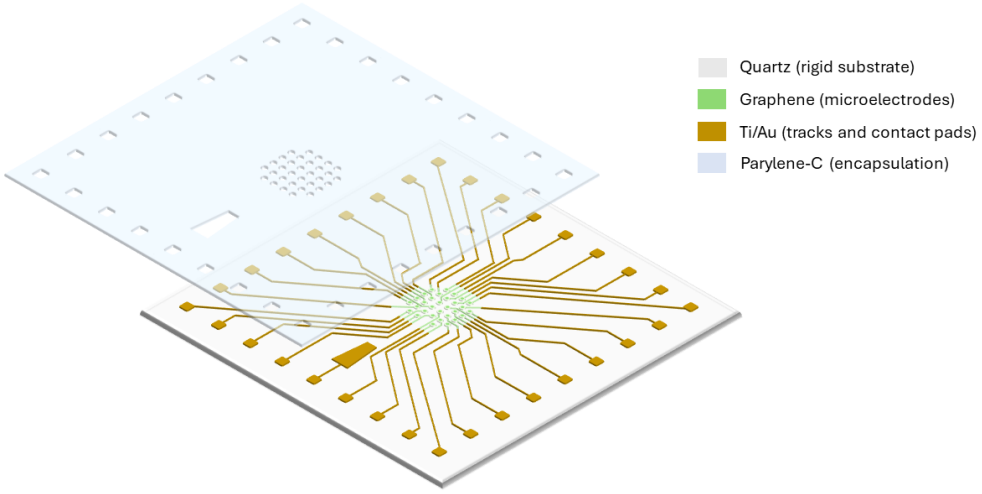

Figure 3.1: Proposed microfabricated *in vitro* MEA dies. Graphene-based electrode array on a rigid transparent substrate, quartz.

The proposed device architecture and materials are well-suited for wafer-scale microfabrication processes, which allow to create structures in micrometer scale with high precision and reproducibility. Microfabrication technology is the standard manufacturing process for semiconductor Integrated Circuits (IC). It is a 2D planar technology based on adding and subtracting layers of materials to create desired structures. Silicon is the dominant material used in IC industry today, most fabrication facilities and equipment are optimized for silicon wafers. Although not highly standardized, other starting materials such as quartz, can also be used for microfabrication processes, allowing for the fabrication of structures on a transparent substrate. The fabrication of graphene MEAs was done entirely in Else Kooi Laboratory of TU Delft.

3.2. Photolithography masks

Photolithography masks are used to define patterns on the surface, and these patterns are transferred through various etching processes (using plasma or chemicals). Every photomask defines a pattern in a single layer of material, thus for a device consisting of multiple layers of materials several photomasks will be required. In particular, a photolithography mask consists of a quartz plate with patterned chromium layer which controls the passage of the incoming light to the photoresist layer deposited on the wafer, thus, restricting the activation of the photochemical process in non-exposed areas. If positive photoresist is used, the developer process will remove photoresist material only in the exposed area. The pattern is now defined and can be subsequently transferred using etching processes.

The design of the photolithography masks was performed using L-Edit v2015.4 software. A total of 12 MEAs with a dimension of 20 × 20 mm could be fitted in a single mask limited by the 4” wafer size, translating into 12 MEAs per wafer. This led to the incorporation of various MEA designs into the masks, primarily by adjusting electrode density and dimensions to enable potential use in diverse applications and to explore the limits of graphene-based technology. The masks were designed compatible with the contact aligner and with dedicated alignment marks. The alignment markers are part of the design and fall within the frame. For each layer there is a separate alignment marker, which allows for aligning the actual mask with respect to the zero layer or first mask.

The photomasks contain the patterns for 12 MEAs with different array layout designs. Several design parameters such as the number of electrodes, diameter and pitch (i.e., centre-to-centre inter-electrode distance) were considered. The nomenclature of the MEA design is as follows: *number of*

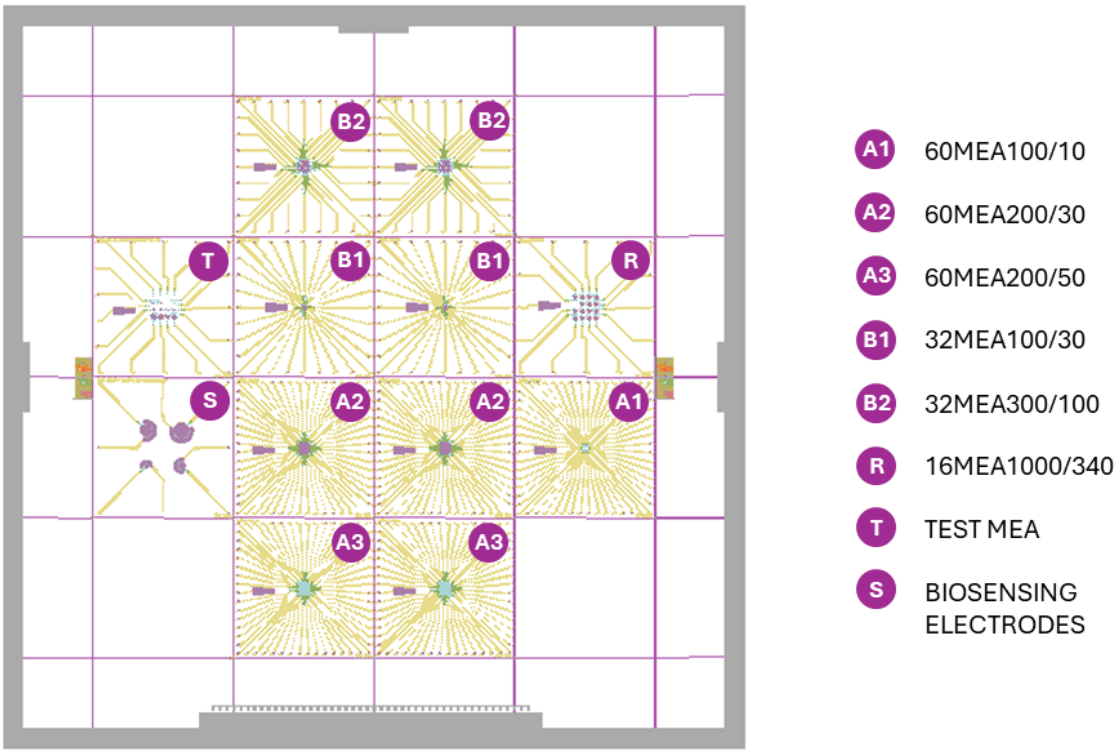

Figure 3.2: Combined overview of the designed photolithography masks. It contains a total of 12 MEAs with a dimension of 20 × 20 mm each in a single mask, translating into 12 MEAs per wafer. Different MEA designs were included tagged with A1, A2, A3, A4, A5, R, T, and B labels. The specification of each MEA design is defined in Table 3.1.

electrodes/MEA/pitch/electrode diameter. The *32MEA100/30* design, see in Fig. 3.3, was developed through iterative discussions with collaborators at Erasmus MC. Their goal was to create a relatively small electrode diameter approaching single-cell resolution while keeping a compact pitch. Flexibility in the total number of electrodes allowed for adjustments. After initial calculations to balance technological constraints, such as maintaining track resistivity and ensuring sufficient spacing, the final established design was a 32-electrode MEA with 30 µm diameter and a spacing of 100 µm pitch. An electrode layout with larger dimensions, *32MEA300/100*, was tailored for lower impedance and higher SNR recordings (given that the impedance scales up inversely with the electrode size). Electrode layouts with higher number of electrodes, e.g., *60MEA200/30* and *60MEA200/50*, were designed to have a larger coverage area. In order to test the limits of the graphene-based technology, a high-density electrode array with single-cell dimension electrodes, *60MEA100/10*, was considered. An additional layout, *16MEA1000/340*, to relate the results and quality of graphene with previous work [18] was included. The specifications of the aforementioned electrode layouts are described in Table 3.1. On top of that, a *Test MEA* with various electrode diameters (10, 20, 30, 50, 100, 200, 340, 500 µm) was included for a more direct and efficient characterization of the electrodes' performance with respect to their sizes. Finally, an electrode layout for biosensing applications, *Biosensing electrodes*, was designed to explore specific hydrogels on graphene electrode substrate as a selective sensing method of certain biomolecules. In this design, each sensing electrode was paired with a surrounding reference electrode, separated by a specific distance, allowing the measurement of capacitance between the two as the primary variable of interest.

To achieve the desired patterning of each material layer in the MEAs, a total of four distinct masks, Fig. 3.4, were designed:

- GRAPHENE: A bright field mask intended for use with positive photoresist. This mask is used to pattern the molybdenum catalyst layer for the selective CVD growth of multilayer graphene.
- METAL ELECTRODES: A bright field mask also used with positive photoresist. This mask patterns

	Number of electrodes	*Diameter* (μm)	*Total electrode area** (μm^2)	*Pitch* (μm)	*Tracks width* (μm)		*Field of view* (μm^2)
					graphene	*Au*	
$32MEA100/30$	32	30	707	100	20	30-150	700 x 700
$32MEA300/100$	32	100	6480	300	80	100-150	2100 x 2100
$60MEA100/10$	60	10	79	100	15	20-120	900 x 900
$60MEA200/30$	60	30	707	200	30	40-120	1800 x 1800
$60MEA200/50$	60	50	1825	200	30	40-120	1800 x 1800
$16MEA1000/340$	16	340	68320	1000	100	200	5000 x 5000

Table 3.1: Specifications of the different MEA designs included in the mask. Several design parameters such as the number of electrodes, diameter and pitch were considered. The total electrode area and field of view scaled up with the electrodes' sizes and the density. The widths of the tracks were adapted to each of the design. Au track widths increased outward from the graphene contact points towards the contact pads as more space became available. * The total electrode area is calculated after subtracting the holes. These holes are included to prevent delamination between the Ti/Al protective metal layer and the graphene layer. For electrodes with diameters of 30 µm or smaller, the risk of Ti/Al delamination is lower, allowing the omission of holes [20]. Hole sizes of 2x2 µm, 5x5 µm and 20x20 µm were designed for the 60MEA200/50, 32MEA300/100 and 16MEA1000/340, respectively.

the Ti/Al layer, which serves as a sacrificial layer to protect the graphene throughout processing and particularly during the creation of openings in the parylene layer via O_2 plasma etching.

- AU TRACKS: A bright field mask designed for use with negative photoresist. This mask is employed to pattern the Ti/Au layer via lift-off process.
- OPENINGS: A dark field mask intended for use with positive photoresist. It is used to pattern the openings in the parylene-C layer, exposing the underlying electrodes and contact pads.

MASK DESIGN CONSIDERATIONS

The design of photolithography masks is essential to the success of the microfabrication process. It requires careful consideration of technological limitations and process requirements to ensure proper

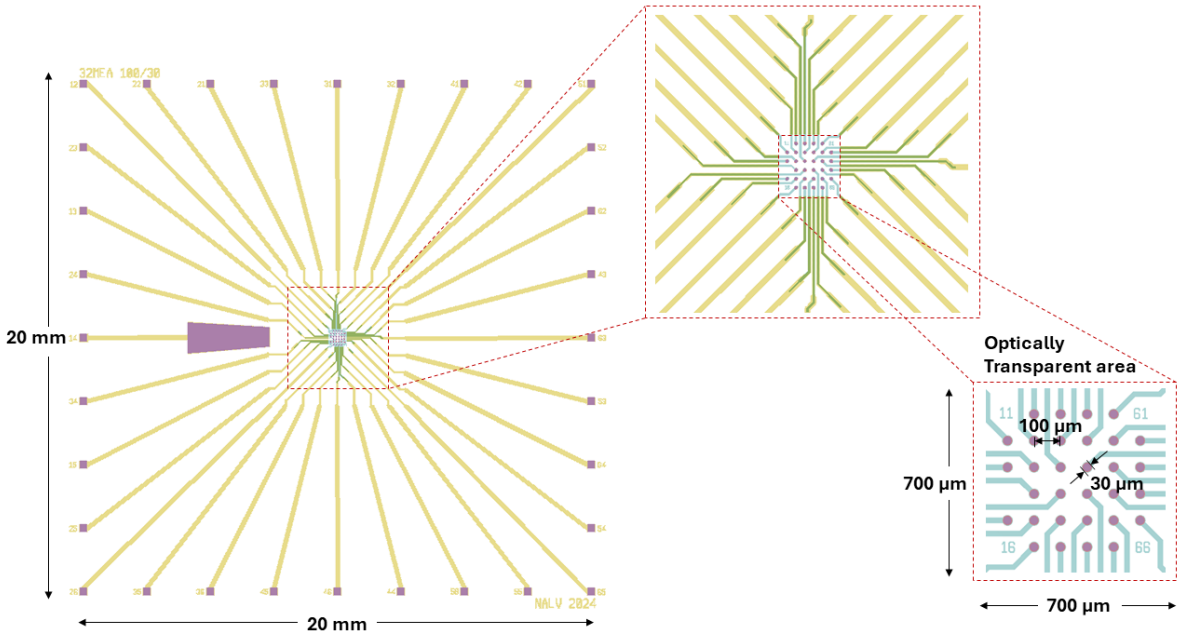

Figure 3.3: 32MEA100/30 electrode layout designed for the brain slice recording test. 31 working electrodes and one reference electrode are arranged in a 6 × 6 layout grid with electrode diameters of 30 µm and interelectrode distances of 100 µm. The optically transparent area, 700 × 700 µm, is designed to be larger than the field of view of the epifluorescence microscope to be used.

integration with the fabrication techniques. In this work, holes in the microelectrode graphene layer were incorporated to provide a better adhesion between the graphene and the sacrificial protective metal layer, Ti/Al, reducing the risk of metal delamination [18]. However, for the 30 µm-diameter electrodes and smaller no holes were required based on the experimental results of León González [20]. As observed in Fig. 3.4, the metal layer on top of the electrode is slightly smaller in diameter than the graphene layer to ensure its complete removal towards the end of the fabrication process. Likewise, the encapsulation openings are smaller to secure the edges of the graphene layer and protect against potential delamination. A minimum margin of 2.5 µm on each side was set between these layers to avoid complications resulting from overetching, isotropic etching and/or poor masking layer performance.

Additionally, the adhesion between Ti/Au and graphene is not very strong. To enhance stability, the Ti/Au tracks were designed to be wider than the graphene tracks by at least 2.5 µm on each side, allowing them to also adhere to the substrate. The length of the overlap was set to approximately 200 µm. There is a trade-off between improving the graphene-Ti contact resistance by increasing the contact area and avoiding high aspect ratio structures that could increase the risk of graphene delamination. The length of the graphene inner tracks was minimized to only the designated field of view to lower the resistivity. The field of view, representing the area for neural imaging, was defined based on both the optical microscope's actual field of view and the area of each electrode design layout. Another way to lower the graphene tracks resistivity is by increasing their width; however, this also reduces the spacing between tracks. Consequently, this could potentially lead to higher electrical crosstalk and compromise the adhesion of the parylene encapsulation layer in narrow spaces. Another design consideration involves the MEA contact pads, defined in the Au layer, which were designed for gold wire-bonding with

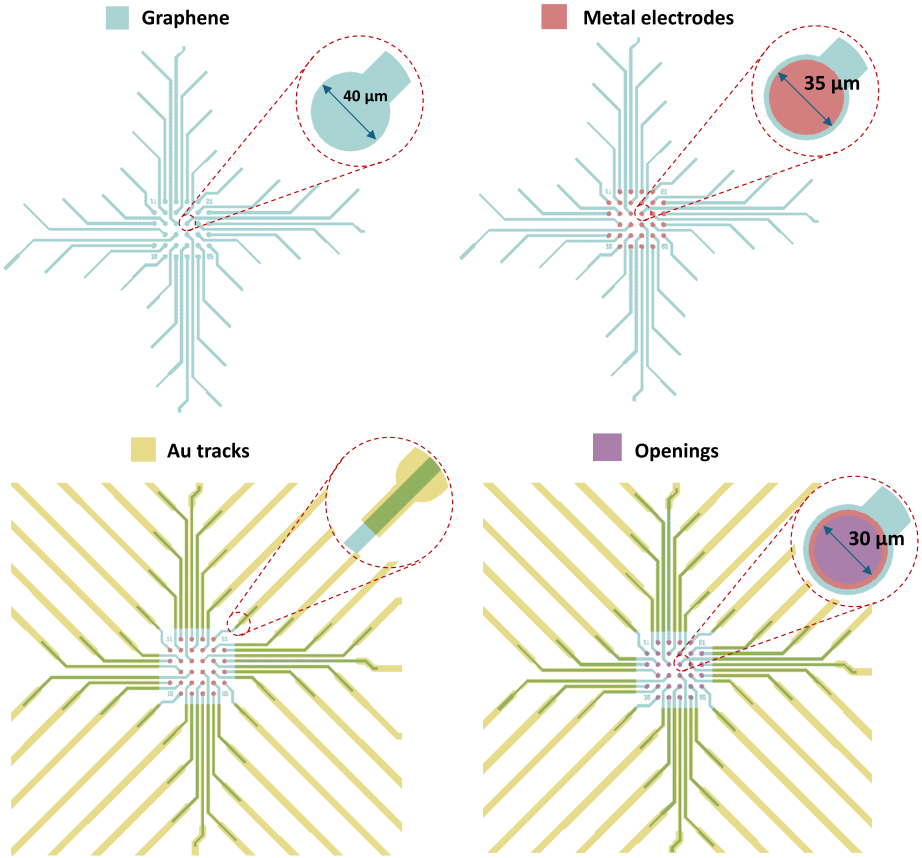

Figure 3.4: Mask layers designed to pattern each of the material layers that constitute the graphene MEAs. The first mask, graphene, corresponds to the Molybdenum (Mo) pattern which will define the graphene growth. The second layer, metal electrodes, defines the pattern for the Ti/Al protective layer on the microelectrodes. The third layer, Au tracks, defines the Ti/Au tracks that extend the graphene inner track to the contact pads. The four and last layer, openings, defines the holes for the microelectrodes, reference electrode and contact pads in the encapsulation layer.

dimensions of 300 x 300 µm (openings: 280 x 280 µm).

4

Device fabrication

This chapter outlines the development and fabrication of two types of graphene-based *in vitro* MEAs: graphene MEA (grMEA) and PEDOT:PSS-coated graphene MEA (grppMEA). The chapter focuses on process development, discussing optimized microfabrication procedures for the integration of transfer-free multilayer graphene technology on *in vitro* MEA, as well as the combination of PEDOT:PSS conductive polymer with graphene microelectrodes.

4.1. Development of graphene MEA

4.1.1. Microfabrication process

Fused silica quartz wafers were used as transparent starting material due to their ability to withstand the high temperatures required for graphene growth, their superior resistance to graphene delamination compared to sapphire substrates, and their ease of dicing in comparison to sapphire [20]. The microfabrication process of the graphene MEA, grMEA, is illustrated in Fig. 4.1. Notice that zero layer alignment marks are of no use in transparent wafers as the marks are not visible. Instead, all layers were aligned to the first mask layer.

MO DEPOSITION, PATTERNING AND GRAPHENE GROWTH

The fabrication started with a 50 nm molybdenum (Mo) layer deposition at 50ºC in the frontside of the

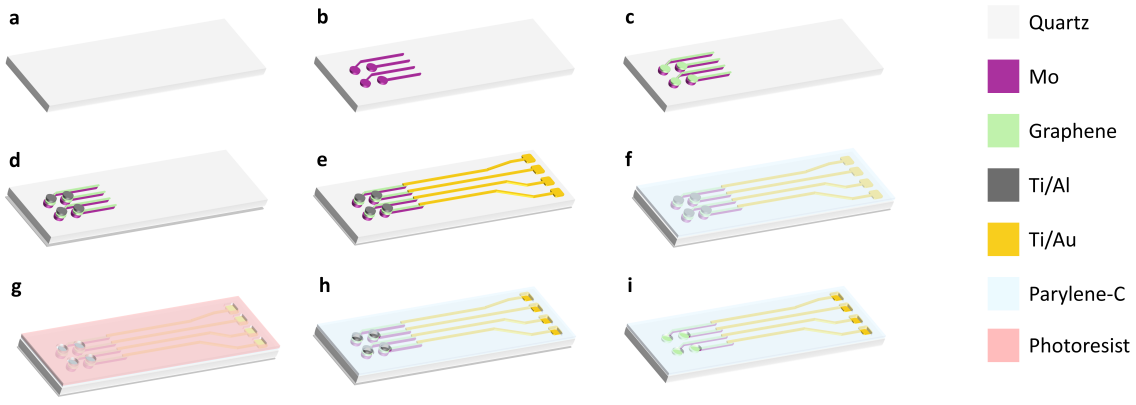

Figure 4.1: Wafer-scale transfer-free fabrication process steps of grMEA electrodes. a. Quartz wafer substrate, **b.** sputtering of 50 nm Mo layer and patterning, **c.** CVD multilayer graphene growth, **d.** Ti/Al deposition and patterning on the microelectrodes, and deposition of a 200 nm Ti layer in the backside (for the later electrostatic clamping in the AMS110 plasma etcher, in step h), **e.** Ti/Au (10/200 nm) evaporation and lift-off, **f.** deposition of 1 µm parylene-C encapsulation layer, **g.** photoresist mask deposition, **h.** parylene plasma etching, **i.** Ti/Al and Mo wet etching on the electrode openings.

wafer via sputtering (using Trikon Sigma 204). The molybdenum serves as the catalyst layer for the subsequent graphene growth. Next, a temporary 50nm Ti layer was sputtered at 50ºC at the backside for the wafer to be optically detected in the metal etcher equipment. After both sputtering processes, lithography steps defined the pattern in the molybdenum layer (Fig. 4.1 b). Lithography steps involved: (1) a initial coating with 1.4 µm SPR2012 positive photoresist with an extended soft bake time so as to compensate for the low thermal conductivity of quartz, (2) exposure with the SUSS MicroTec MA/BA8 contact aligner using the GRAPHENE mask, and (3) development with MF322 developer, with extended post-exposure and hard-bake times. The defined pattern is then transferred by plasma etching of the molybdenum layer in an ICP-RIE etcher, Trikon Omega 201. ICP-RIE etching uses an inductively coupled plasma source to produce high-density plasma, offering precise process control through separate RF and ICP generators. Two different Mo etching recipes were evaluated: one at 25ºC using 50W RF power, 500W ICP power, 5 mTorr pressure, and flows of 30 and 5 sccm for Cl_2 and O_2 gases, respectively; the other at 40ºC with no RF power, 500W ICP power, 5 mTorr pressure, and SF_6 gas at 25 sccm flow. The total etching time in both cases was set to 35 seconds. Following this, the ion bombarded photoresist was stripped using a bath with NI555 solvent solution. Ultrasonication at 80 kHz and elevated temperatures (50-60 ºC) were employed to accelerate the process. However, due to the ion bombardment, NI555 might not be effective enough at completely removing the photoresist. An additional short oxygen plasma cycle (using TePla Plasma 300) could be used to get rid of the residues left. The Ti layer in the backside is then fully wet etched using HF 0.55% bath to avoid any contributions from it during the graphene growth process. Graphene is then selectively grown on the molybdenum structures. The growth was done via chemical vapor deposition (CVD) process (using Aixtron Black Magic Pro tool) at 935ºC with 960, 40 and 25 sccm of Ar, H_2 and CH_4 gases for 20 min.

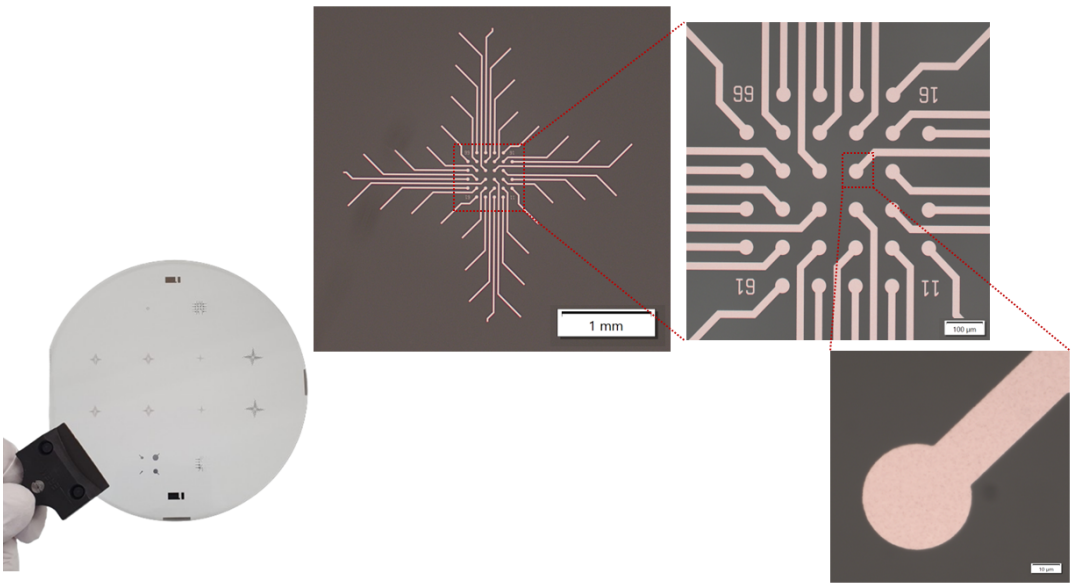

Figure 4.2: Image of a quartz wafer with graphene grown on patterned molybdenum layer. Bright-field optical images of the 32MEA100/30 electrode layout. At the highest magnification, the typical grain-like morphology of graphene is observed.

AL METAL DEPOSITION AND PATTERNING

A Ti/Al metal layer protects the graphene electrodes throughout the fabrication process and in particular, during the plasma etching of the Parylene-C encapsulation layer, which uses O_2 plasma. A stack composed of 50 nm Ti and 100 nm pure Al was sputtered at 50 ºC (using Trikon Sigma 204). At this point of the process, because the Black Magic tool is contaminated with Cu particles, the wafers were considered to be ”contaminated” or not CMOS process compatible, thus, precautions and dedicated procedures and equipment were used. Lithography steps defined the patterns of interest in the Ti/Al layer. For that, manual coating with 3.1 µm-thick AZ3027 positive photoresist followed by baking, exposure in the contact aligner using the METAL ELECTRODES mask and development was conducted. Special caution was taken in the development step as the MF322 developer showed initial signs of at-

tacking the metal layers underneath. This considered, instead of immersing the wafer on the developer, it was gently poured on top of the wafer forming a puddle to have a greater control over the time. An extra baking step for the photoresist was performed in order to make it more resistant to the subsequent wet etching step. The photolithographically defined pattern was then transferred by a wet etch process with 0.55% HF solution (Fig. 4.1 d). Afterwards, the photoresist was removed with acetone followed by IPA.

Alternatively, lift-off technique was performed to address some challenges encountered by wet etching process, described in 4.1.2. For this, wafers were manually coated with negative photoresist, 3.5 µm NLOF-2020, exposed in the contact aligner with the METAL ELECTRODES mask and developed. The negative photoresist covered the entire wafer except for the areas designated for the aluminum. Subsequently, a Ti/Al (10/100 nm) layer was evaporated in CHA Solutions Std. For the patterning of the metal layer, NI555 stripper was used to remove the photoresist and along with the evaporated metal on top, leaving the protective Al structures on the electrodes revealed.

GOLD EVAPORATION AND PATTERNING

Gold, known for its superior conductivity and biocompatibility, was chosen to extend the inner graphene tracks outward and to form contact pads. Before preparing the wafers for Au evaporation, a 200 nm Ti layer was evaporated (using a CHA Solutions Std.) in the backside for the electrostatic clamping in the ICP-RIE plasma etcher process step to come. Since the gold pattern was created by lift-off technique, first thing was to manually coat the wafers with 3.5 µm NLOF-2020 negative photoresist. To this, baking, exposure in the contact aligner with the AU TRACKS mask and development steps were followed. The negative photoresist covered the whole wafer except for the areas where gold was meant to stay. A Ti/Au (10/200 nm) layer was evaporated in CHA Solutions Std. The thin Ti layer serves as an adhesion promoter between gold and the substrate. Controlling deposition rates, substrate heating during deposition and an initial high vacuum is crucial for achieving a strong adhesion of Ti/Au to the substrate. The photoresist was then stripped with NI555 solvent solution overnight so as to leave behind the gold only in the patterned area, directly on the substrate (Fig. 4.1 e).

ENCAPSULATION LAYER

The wafers were coated with a 1-2 µm parylene-C layer (Fig. 4.1 f), which was CVD deposited at room temperature (using a SCS PDS 2010 parylene coater). Parylene-C served as the insulating coating of the MEAs. 3-(trimethoxysilyl)propyl methacrylate (A-174 Silane) was used as an adhesion promoter

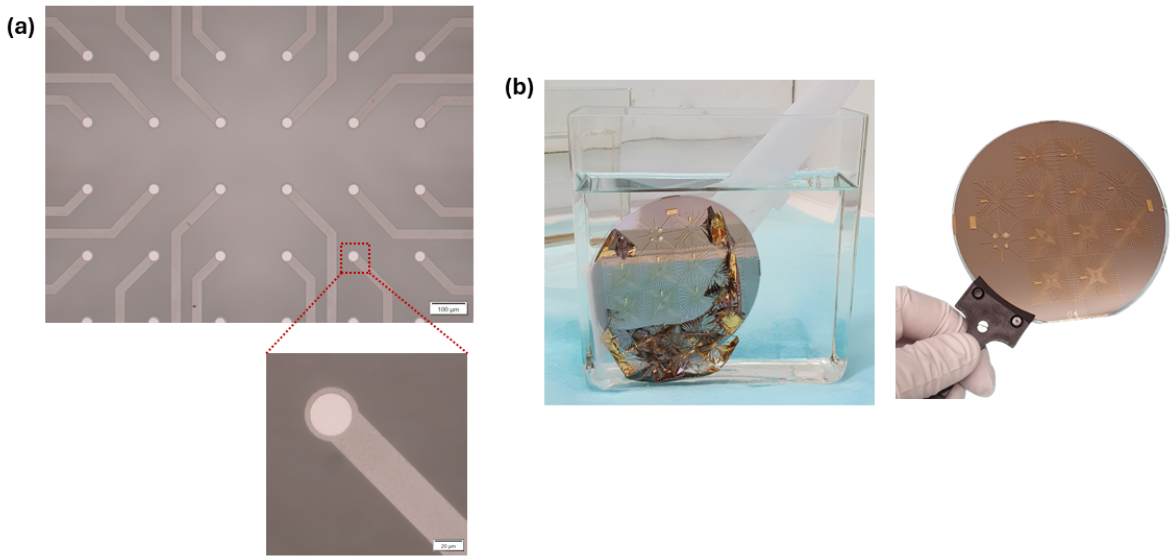

Figure 4.3: **(a)** Bright-field optical images of the 60MEA200/30 electrode layout. The patterned Al protective layer (with a diameter of 35 µm) on top of the graphene is shown. **(b)** Lift-off process for gold patterning.

for parylene on the substrate. A patterned thick photoresist coating was used as the masking layer to expose electrodes and contact pads in the parylene layer. This was achieved by manually coating the wafers with a 6.5 µm-thick AZ 10XT positive photoresist, exposure in the contact aligner with the OPENINGS mask, and subsequent development. A plasma etching step (using AMS110 etcher, Alcatel) created the openings in the parylene-C, landing on the Al protective layer. O_2 and SF_6 gases were used at 185 sccm and 15 sccm flows respectively, and with 40W LF power. The photoresist mask was removed with acetone followed by IPA. Additional cleaning with NI555 was performed to ensure that the ion bombarded photoresist was completely removed.

The parylene etching rate and the selectivity to photoresist in the AMS110 plasma etcher were characterized with Si test wafers prior to performing this step in the final wafers. The parylene to photoresist selectivity was around 1 due to their organic nature. This implies that the bombarded ions would also cause lateral etching of the openings in the photoresist mask, slightly widening them. The experimentally obtained etching rate of parylene with the aforementioned recipe was around 500 nm/min. A slight non-uniformity in the etching process across the wafer was observed.

To minimize the risk of damaging the exposed graphene during the plasma etching process, especially when the Al protective electrodes were overetched, a double photoresist coating approach was used. This involved first applying a photoresist mask and beginning the plasma etching process. Midway through the etching, the initial photoresist mask was stripped away, and a second photoresist mask was applied. This approach helped mitigate the risk of graphene damage or removal by oxygen plasma on the wafers where the Al protective layer was overetched. For the wafers where the Al patterning was done via lift-off, a single photoresist mask was sufficient.

WAFER DICING

Prior to dicing, the whole wafer surface was coated with a thick 4 µm AZ3027 photoresist layer to protect it from the dicing procedure. The quartz wafers were then diced (using a Disco Dicer DAD3240) with a dedicated diamond blade. The microfabricated dies were cleaned in acetone followed by IPA. Thereafter, the Al protective layer on the electrodes as well as the backside Ti layer were fully etched in 0.55% HF solution. And finally, Mo was wet etched by gently covering the electrode area with 31% H_2O_2 forming a puddle (Fig. 4.1 i). An etching time of 3 min was sufficient to remove almost completely the Mo layer underneath without causing graphene detachment. The microfabricated dies were left in vacuum overnight at 80ºC to remove any moisture and ensure a better adhesion in between layers.

4.1.2. Process observations

The presented microfabrication process of grMEA involved numerous processing steps, each requiring careful optimization. Several challenges emerged, particularly when working with non-standard substrates like quartz wafers and integrating delicate materials like graphene.

PROCESSING WITH NON-STANDARD WAFERS

Processing non-standard wafers, such as quartz, introduced unique difficulties. The semiconductor industry is predominantly optimized for Si wafers, which means that adapting established processes to alternative substrates like quartz required some modifications. For instance, many cleanroom tools rely on optical sensors for wafer detection. To address the optical transparency of quartz substrates, temporary metal layers, such as Ti, were deposited on the backside of the wafer to enable detection, or alternatively, the sensors were disabled entirely. Additionally, the lithography process also required adaptation, such as extended bake times, to account for the lower thermal conductivity of quartz. On top of that, quartz wafers showed charging phenomena in scanning electron microscopy (SEM). Due to the fact that quartz does not conduct electricity, when the electron beam of the SEM hits the quartz wafer, the electrons accumulate on the surface and cannot be conducted. SEM is a very useful technique since it allows to qualitatively assess the surface morphology, analyse fine details of microstructures and collect signals that might help identify the different material layers present on the imaging area. However, this charging phenomenon limited the applicability of SEM, complicating surface analysis. Lastly, the limited availability and high cost of quartz wafers restricted testing opportunities, so many process optimizations were first carried out on Si wafers. However, the transition from Si to quartz was

not one-to-one, requiring additional refinements due to the differing material properties.

AL PATTERNING: POLYMERIC RESIDUES AND OVERETCH STRUCTURES

Several observations were done in the Al patterning process. Firstly, the wet etching process was observed to be non-uniform, the etching process was initiated in the patterned structures and gradually extended until the entire wafer surface was etched. This resulted in overetched structures by 1-3 µm and, in some cases, complete removal of the protective Al electrode, severely compromising the functionality of the final MEA devices. Overetched Al patterns led to insufficient graphene surface coverage for the subsequent parylene plasma etching step, causing damage or removal of the exposed graphene areas by the oxygen plasma. Additionally, residues were observed after the Al wet etching step, as shown in Fig. 4.4. These residues persisted even after the complete removal of the Ti/Al layer, depositing on top of the graphene layer. SEM imaging with the sample tilted indicated the presence of a very thin (nm-thick) film, showing some wrinkles and foldings. Raman spectra revealed that these residues were a form of carbon. These polymeric residues were strongly adhered to the graphene surface showing resistance to additional cleaning methods with acetone and NI555 stripper at elevated temperatures and ultrasonication. Ultimately, the residues were removed by manually scrubbing the areas with a Q-tip immersed in acetone.

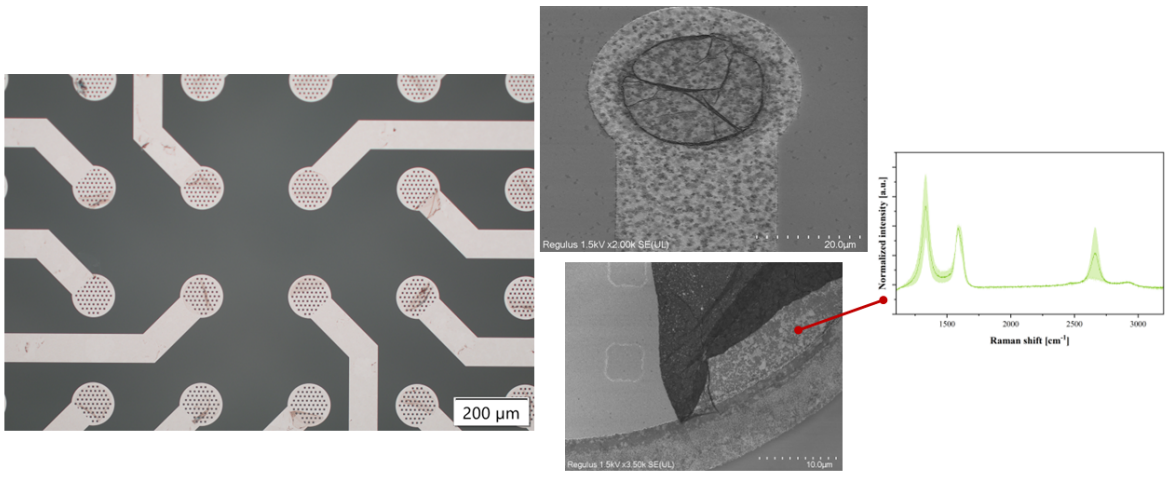

Figure 4.4: Polymeric residues on the electrode area emerging after the Ti/Al patterning process. The optical image shows that even after the complete removal of the Ti/Al layer, the residues were deposited on the graphene layer. SEM imaging with the sample tilted gave indications pointing towards the presence of a very thin (nm-thick) film. Raman spectra revealed that these residues were some kind of C form.

Even though wet etching is a direct patterning technique, it provides less material control partly due to the isotropic nature of the process. Alternative techniques such as lift-off allows for sharper and more precise patterning, thus avoiding the overetched structures resulted from the Al wet etching. Fig. 4.5 reflects the significant differences observed between these two patterning approaches. Al evaporation followed by lift-off was observed to provide greater control over the patterning process, avoiding the non-uniformity and overetching issues associated with wet etching. Fence-like structures, typical from lift-off patterning, were present on the edges of the patterned structures, even so, they did not compromise the functionality of the final MEA devices.

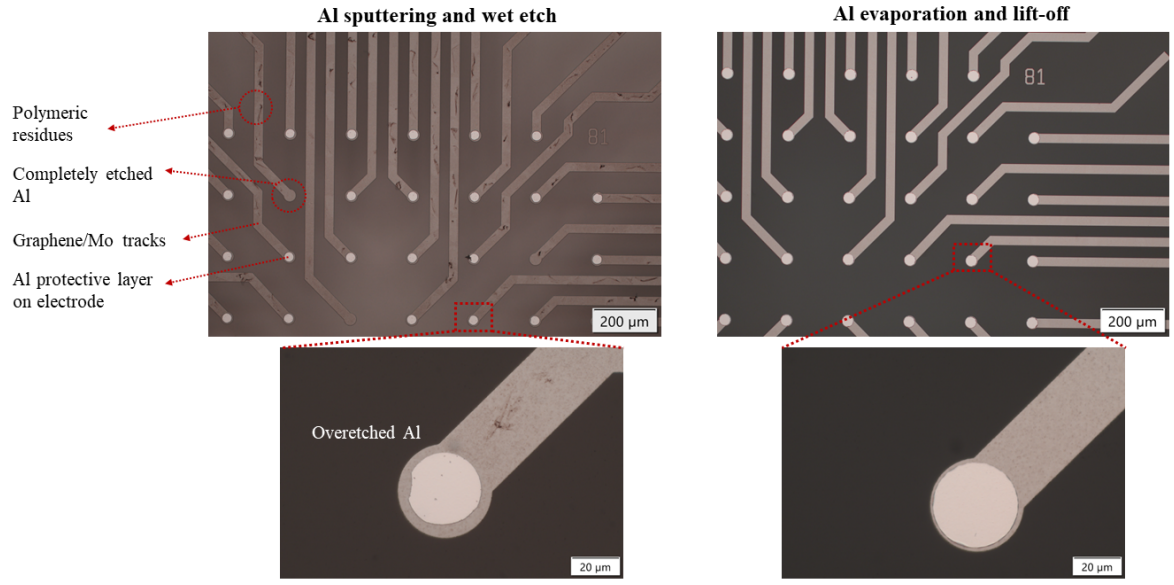

Figure 4.5: Explored Al patterning techniques for protecting graphene electrodes. Two different approaches were explored: sputtering followed by wet etch and evaporation followed by lift-off. Wet etch process posed several challenges, such as polymeric residues post-Al patterning, overetched structures and even complete removal of Al structures in some cases. Lift-off showed greater control over the patterning process.

MO REMOVAL POST-GRAPHENE GROWTH

An exploratory study for complete Mo removal post-graphene growth was conducted in Si test wafers prior to processing the final quartz wafers. The explored methods and obtained results are described in Appendix A.1. Plasma etching poses risks to graphene quality due to potential damage from ion bombardment. Despite efforts to optimize the plasma etching parameters using SF_6 gas and reducing physical sputtering, Raman spectroscopy revealed unavoidable damage to the carbon-carbon (C-C) bonds within the graphene. In contrast, wet etching with hydrogen peroxide (H_2O_2) was tested and found effective in removing Mo without compromising graphene quality. To minimize the risk of graphene detachment, the Mo wet etching was introduced after the patterning of the metal layers. The Ti/Al layer patterned in the microelectrodes and the gold tracks partly overlapping with the graphene inner tracks provided additional support for maintaining the graphene layer in place when etching the underneath Mo layer. Nonetheless, the translation of this wet etching process from Si to final quartz wafers was not successful, as the graphene layer broke and detached during the procedure.

4.2. Development of graphene/PEDOT:PSS MEA

Reducing the electrode impedance and enhancing its ions-to-electrons transduction efficiency while maintaining optical transparency was the main motivation to coat graphene microelectrodes with a conductive PEDOT:PSS polymer layer.

Two different PEDOT deposition techniques were considered: electropolymerization and spin coating. In electropolymerization, PEDOT precursor ions are attracted to the conductive graphene electrode surface by applying a current. This process involves immersing the electrodes to be coated, along with a counter electrode, into a solution containing the ionic form of PEDOT. An electric field induces a reaction that drives the selective deposition of nucleated PEDOT ions onto the conductive surface. The thickness of the PEDOT layer can be controlled by adjusting the applied current and the polymerization time. However, this method is time-consuming, especially for high-density microelectrode arrays, and is sensitive to the uniformity of the graphene layer, such as the presence of C-C defects and Mo residues. Alternatively, PEDOT deposition via spin coating followed by patterning with a peel-off technique offers a promising approach, first developed by George G. Malliaras' group [56]. This method presents several advantages, including ease of application, integration into the microfabrication process, and

reduced sensitivity to graphene non-uniformities. Therefore, this later approach was adopted for the development of graphene/PEDOT:PSS microelectrode arrays, grppMEA, in this current work.

4.2.1. Microfabrication process

The fabrication process steps prior to the parylene encapsulation have been previously described in subsection 4.1.1. These steps are: Mo deposition and patterning, graphene growth, Al metal deposition and patterning, gold evaporation and lift off. At this point, a 1 µm parylene C (ParC) insulation layer was deposited using 3-(trimethoxysilyl)propyl methacrylate (Silane A-174) to promote its adhesion to the substrate. Next, a 3% (v/v) micro-90 soap solution was spin coated at 1000 rpm which acts as an anti-adhesive layer. Subsequently, a second 1 µm ParC sacrificial layer was deposited, together forming the ParC/anti-adhesive/ParC stack (Fig. 4.6 b). Electrode openings and contact pads of the MEA were defined by photolithography using AZ10XT photoresist, followed by plasma etching (using AMS110 etcher, Alcatel) to transfer the pattern to the ParC/anti-adhesive/ParC stack (Fig. 4.6 d). To etch the double parylene, O_2 and SF_6 gases were used at 185 sccm and 15 sccm flows respectively, and with 40W LF power. The photoresist mask was removed with acetone followed by IPA. Additional cleaning with NI555 was performed to ensure that the ion bombarded photoresist was completely removed.

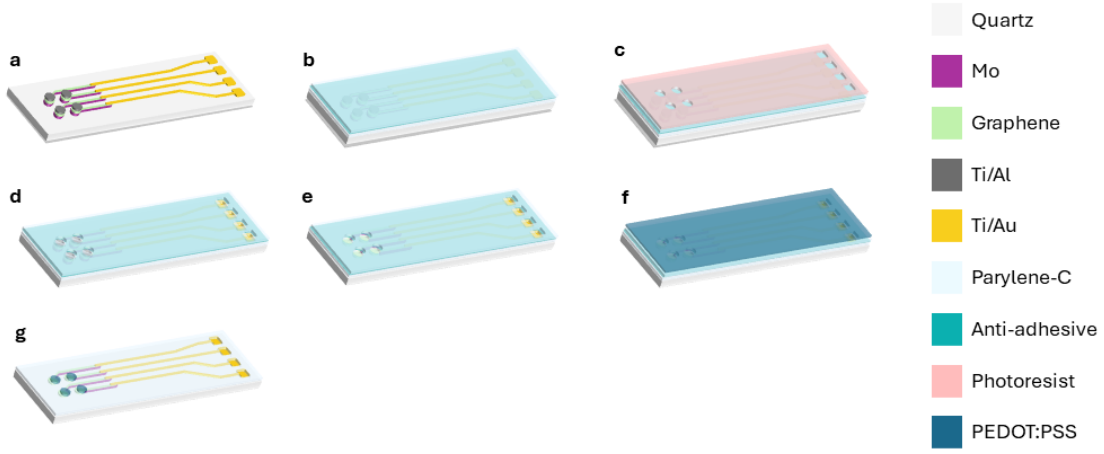

Figure 4.6: Fabrication process steps for the integration of a patterned PEDOT:PSS coating on graphene microelectrode arrays. a. Quartz wafer with graphene grown on Mo, and patterned metallization layers (Ti/Al protective layer on electrodes and gold conductive tracks). **b.** deposition of ParC/anti-adhesive/ParC layer stack consisting of a first 1 µm parylene-C encapsulation layer, anti-adhesive layer (micro-90 soap) and a second 1 µm parylene-C sacrificial layer. **c.** photoresist mask deposition. **d.** Plasma etching of ParC/anti-adhesive/ParC layer stack. **e.** Ti/Al and Mo wet etching on the electrode openings. **f.** PEDOT:PSS spin coating (at 1000 rpm). **g.** Patterning of the PEDOT:PSS layer by peeling off ParC sacrificial layer.

The quartz wafers were then diced using a Disco Dicer DAD3240, protected by a photoresist layer. The dicing parameters were carefully optimized by reducing the feed speed (from 3 mm/s to 1 mm/s) and lowering the water influx (from 0.5 L/min to 0.2 L/min) to prevent the second sacrificial parylene layer from getting delaminated. The processing of the MEA dies continued with the removal of the Ti/Al protective layer using a 0.55% HF wet etching solution, followed by an additional wet etching step to remove the Mo from the electrode openings with 31% H_2O_2 (Fig. 4.6 e). At this point, graphene was the only material remaining on the electrodes. Next, PEDOT:PSS solution was spin coated at 1000 rpm, and soft baked at 95 ºC for 2 min. The conductive polymer solution was prepared by adding 5 vol% ethylene glycol (EG), 0.002 vol% dodecylbenzene sulfonic acid (DBSA) and 1 wt% of 3-Glycidyloxypropyltrimethoxysilane (GOPS) to the PEDOT:PSS solution. The sacrificial ParC layer was then gently peeled off with a scotch tape, facilitated by the poor adhesion provided by the soap. This selectively removed PEDOT:PSS from non-electrode areas, leaving it only on electrodes and contact pads. Subsequently, PEDOT:PSS was cleaned off the contact pads and gold reference electrode

with a Q-tip dipped in DI water. A final hard bake step at 140 ºC for 1h ensured complete crosslinking of GOPS from the PEDOT film, thereby improving its adhesion to the substrate and film's stability. Lastly, the completed dies were immersed in DI water overnight to remove any remaining anti-adhesive residues and low molecular weight compounds from the PEDOT.

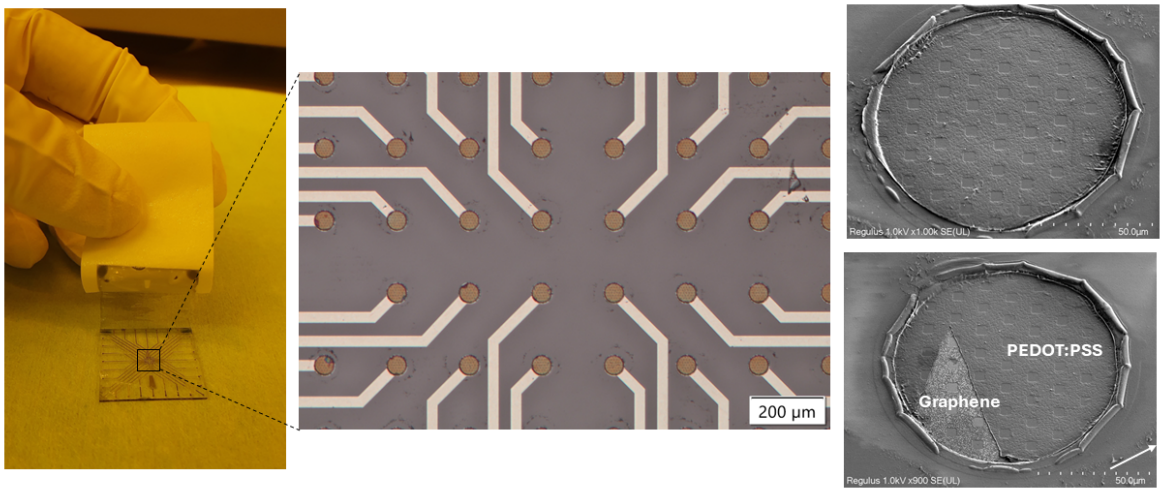

Figure 4.7: PEDOT:PSS patterning on graphene MEAs. The sacrificial ParC layer was mechanically peeled off, selectively leaving PEDOT:PSS only on electrodes. The successful patterning of the PEDOT:PSS layer can be observed with optical microscopy by the coloured electrodes, as well as in SEM technique. It should be noted that the peel-off process requires delicate handling and that in some cases, part of the PEDOT can be unintentionally removed from the electrode.

4.2.2. Process observations

Observations regarding the integration of PEDOT:PSS conductive coating on the graphene electrodes were done and are discussed in this section.

DICING OPTIMIZATION

The dicing after the ParC/anti-adhesive/ParC patterning step was performed for two main reasons. First, performing dicing before the PEDOT:PSS spin coating ensures more uniform polymer deposition at the die level, which is preferable over wafer-level coating. Additionally, the subsequent parylene peel-off process is more manageable on individual dies. Second, dicing is a mechanically aggressive process; conducting it while the graphene electrodes are still protected by the Al layer and securely adhered to the Mo layer minimizes the risk of damage to the microelectrodes.

Dicing was encountered to be a critical step in the process flow. Dicing quartz wafers with a ParC/anti-adhesive/ParC stack poses a significant challenge due to the risk of delamination of the sacrificial ParC layer. This risk arises from the mechanical stress and vibrations generated by the high-speed rotating blade used in the dicing process, coupled with a continuous influx of water. The sacrificial ParC layer is particularly vulnerable because of its intentionally weak adhesion to adjacent layers, especially the anti-adhesive layer. To prevent delamination of the sacrificial layer, dicing lines were incorporated into the parylene mask layer to ensure that the dicing blade does not directly cut through the parylene, thereby minimizing the mechanical stress exerted on this layer. Additionally, the dicing parameters were carefully optimized by reducing the feed speed (from 3 mm/s to 1 mm/s) and lowering the water influx (from 0.5 L/min to 0.2 L/min).

PARYLENE PEEL-OFF TECHNIQUE

The spin coating deposition and patterning of PEDOT:PSS via parylene peel-off technique presents several advantageous features, particularly its compatibility with microfabrication processes, high reproducibility of surface characteristics, and the ability to achieve precise patterning without the use of chemicals or ion bombardment. This method, however, requires delicate handling to avoid tearing

the film during the process, especially with thin sacrificial parylene layers. The use of a thin sacrificial layer is especially desirable, as it promotes more uniform spreading of the conductive polymer solution over the electrode openings. The thickness of the pre-patterned double parylene stack significantly influences the distribution of the conductive polymer, with high aspect ratio electrode openings being prone to less homogeneous coating. Additionally, since the peel-off technique is performed manually, variability between users is an inherent challenge, and achieving consistent control over the process demands practice and careful handling.

In the current work, a high yield of successfully patterned PEDOT:PSS on graphene electrodes was achieved. Despite this, several observations were made using optical microscopy and SEM analysis. Small residues of parylene, depicted in Fig. 4.8, were detected within the electrode array region in some of the devices, likely originated from the peel-off process. Importantly, these residues were positioned outside the active sensing area of the electrodes and thus did not interfere with device performance in the intended application. Furthermore, slight variations in electrode color were noted, suggesting uneven thickness of the PEDOT:PSS coating on some electrodes. In a few cases, the conductive polymer was partially or completely removed from certain electrodes, indicating inadequate adhesion between the conductive polymer and the substrate. These observations highlight the need for further refinement of the adhesion process, i.e., surface activation treatments, to ensure more reliable and consistent results across all electrodes. Despite this, the technique remains promising for applications where precise patterning and integration of conductive polymers are essential.

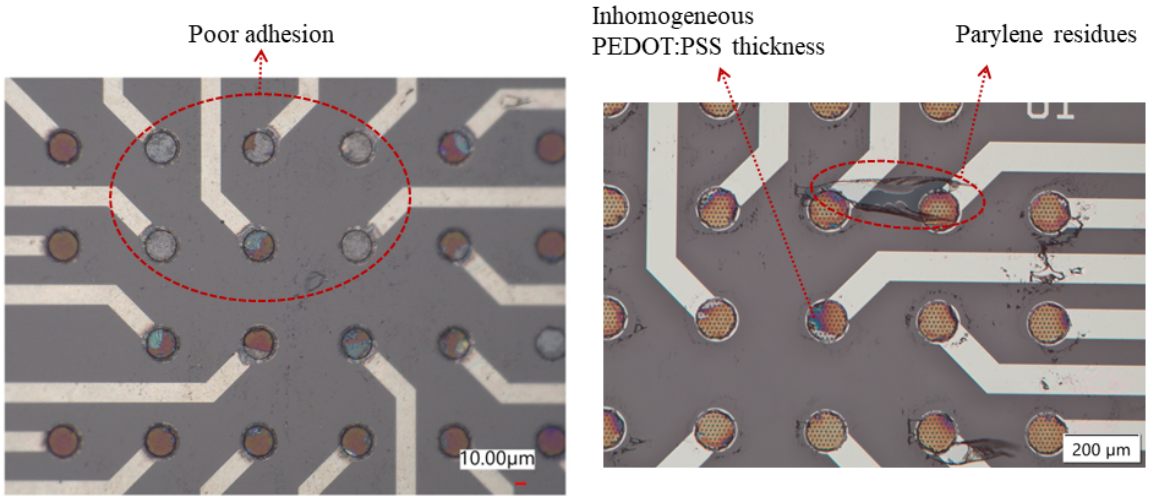

Figure 4.8: Observations regarding the parylene peel-off technique. Small parylene residues outside the active electrode area, variations in the PEDOT:PSS thickness and, partial and complete removal of the conductive polymer, likely due to poor adhesion to the substrate, were observed in few cases.

4.3. Device assembly

The microfabricated dies, each measuring 20 x 20 mm, were integrated onto a custom-designed printed circuit board (PCB) to facilitate electrode characterization and ensure efficient interfacing with commercially available electrophysiology recording systems. The PCB, measuring 49 x 49 mm, was designed with a double ring pad configuration. In this configuration, the inner ring pads, which were wirebonded to the contact pads on the die, were electrically connected to the outer ring pads. The design of the outer ring pads, including their placement, size, and pitch, was specifically optimized to be compatible with Multichannel Systems MEAs featuring 60 electrodes. This configuration also ensured compatibility with other commercial electrophysiology systems, such as the MZ60 MicroElectrode Array interface from TDT.

Prior to wirebonding, the microfabricated dies were attached to the PCB at the corners using a non-conductive epoxy adhesive (EPO-TEK 301-2FL). This epoxy was chosen for its thermal curability, which offers advantages over UV-curable alternatives, as UV exposure may adversely affect the optical

and mechanical properties of the parylene encapsulation. To prevent any unintentional coverage of the contact pads during the gluing process, careful handling was required when applying the epoxy. Additionally, the edges of the dies were sealed from the backside by filling the gaps with the same epoxy to ensure mechanical stability and protection. The devices were subsequently wirebonded, using gold ball bonding technique, to create the electrical interconnection between the microfabricated dies and the PCB.

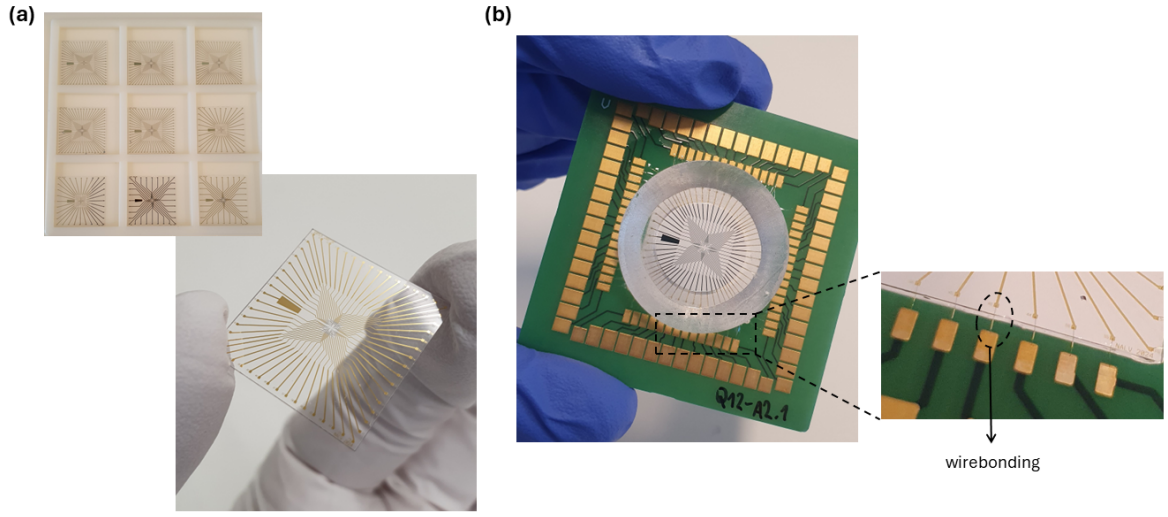

Figure 4.9: (a) Overview of the finalized microfabricated dies. From each wafer, a total of 12 MEA dies, 20 x 20 mm in size, with different electrode layouts were obtained. The quartz substrate enabled for optical transparency on the electrode region determining the field of view. **(b) Assembled grMEA device**. The microfabricated die was coupled to a PCB, 49 x 49 mm in size, designed to be compatible with commercially available *in vitro* electrophysiology recording systems. Au gold wire ball bonding created the electrical interconnection between the pads from the die and the PCB. An inverted cone shape 3D printed well was designed to host PBS solution or culture medium.

To contain the phosphate-buffered saline (PBS) solution or culture medium during experiments, inverted cone-shaped wells were designed and fabricated using an Asiga3D printer. A biocompatible resin, Detax Freeprint Ortho [72], was selected for 3D printing the wells to minimize the risk of cytotoxicity or other adverse biological responses when in contact with cells or tissue slice cultures. The 3D-printed wells were securely adhered to the surface of the MEA device using the same non-conductive epoxy (EPO-TEK 301-2FL), which also served to cover the wirebonds, providing additional mechanical protection against physical damage during handling and use. Fig. 4.9b shows a completely fabricated and assembled grMEA device.

4.4. Summary

The device fabrication of graphene MEAs involved a complex microfabrication process optimized for using fused silica quartz wafers, which provided a transparent substrate for multimodal *in vitro* platforms. This process included multiple steps such as the deposition of a Mo catalyst layer, CVD graphene growth, various lithography techniques for metal patterning and parylene encapsulation. Observations during fabrication revealed issues with non-uniform etching and polymeric residue formation during Al patterning, which posed risks to graphene integrity. The use of alternative lift-off techniques improved patterning control compared to wet etching, avoiding overetching and residue problems. Additionally, while methods for removing the Mo layer post-graphene growth were explored, they highlighted the risks of damaging the graphene. The complete removal of Mo remains an unresolved challenge.

On top of that, the conductive polymer PEDOT:PSS was integrated into graphene MEAs using spin coating and a parylene peel-off technique. The process involved meticulous microfabrication steps and dicing optimization to prevent delamination of layers, with challenges observed in achieving uni-

form PEDOT:PSS deposition, as well as occasional residue and adhesion issues during the peel-off technique. Despite these challenges, high yield and precise patterning were achieved. Furthermore, the assembly of the microfabricated dies onto a custom-designed PCB allowed for seamless integration with standard electrophysiological recording systems. Overall, the successful implementation of these techniques emphasizes the potential of graphene and PEDOT:PSS composites in advancing the field of electrophysiology, for applications in neural interfaces and biosensing technologies. Further optimization of adhesion processes and coating uniformity will be essential for maximizing the performance and reliability of these devices.

5

Device characterization

This chapter describes the methods used to characterize the graphene layer throughout the fabrication process, along with techniques to evaluate the device's optical transparency and electrochemical performance. The results are then presented and discussed, comparing the electrochemical properties of graphene, grMEA, and graphene/PEDOT:PSS, grppMEA, devices with each other and with those of state-of-the-art transparent neural interfaces.

5.1. Raman spectroscopy

Raman spectroscopy is a non-destructive material characterization technique which provides information about the chemical structure, molecular composition, and interactions within a sample. The basis of Raman principle relies on inelastic scattering effect; when a monochromatic laser light source interacts with the sample of interest, a small fraction of phonons is scattered with a shift in wavelength. This shift, known as Raman shift, is specific to the chemical bonds in the sample [73].

In this current work, Raman spectroscopy was employed to confirm the presence of graphene, extract information about the type of graphene (i.e., monolayer, multilayer), quality and amount of defects present in the grown layer. The Raman spectrum of graphene fundamentally consists of three distinct peaks: D peak, G peak and 2D peak, observed within the 1100 to 3200 cm^{-1} range of wavelength shifts. The G peak, located around 1582 cm^{-1}, is a first-order Raman mode originating from the in-plane vibrations of sp^2-bonded carbon atoms (C-C bonds), thus being present in all graphite-based materials [73]. The 2D peak, appearing at approximately 2700 cm^{-1}, is a second-order Raman mode resulting from a two-phonon, double-resonance process. The shape, position, and intensity of the 2D peak are particularly useful for distinguishing between single-layer graphene (SLG) and multilayer graphene (MLG) [74]. In particular, the ratio of the intensities of the 2D peak to the G peak (I_{2D}/I_G) provides an indication of the number of graphene layers present. A higher I_{2D}/I_G ratio (typically > 1) is indicative of monolayer graphene, while a lower ratio (typically < 1) suggests the presence of multiple layers. The D peak, found around 1350 cm^{-1}, is associated with the breathing modes of sp^2 atoms in rings and is disorder-induced, requiring a defect for its activation [74]. The intensity of the D peak relative to the G peak (I_D/I_G ratio) serves as an indicator of the amount of defects or disorder within the graphene layer. A higher I_D/I_G ratio signifies a greater number of defects.

For this research work, a Renishaw inVia Raman system with a red laser of 633 nm was employed. The spectrum was acquired with 50% laser power and 20 s of exposure time to achieve an adequate signal-to-noise ratio. Several point measurements from each sample were taken, and then post-processed in Matlab. The Matlab script extracted the baseline using a non-linear least squares fit function, normalized the data with respect to G peak, and averaged multiple measurements from the same sample. Raman spectra at different stages along the fabrication process were obtained to monitor the presence and quality of graphene. To improve the Raman signal in quartz wafers, a silicon wafer was placed underneath. The silicon substrate can help in reflecting the laser light back into the quartz wafer, increasing the molecular interaction and thereby, enhancing the Raman signal intensity.

Fig. 5.1 shows the Raman spectra of the transfer-free multilayer graphene on quartz substrate obtained at different stages of the process. Each graph line shows the average and standard deviation of 5 point measurements. The obtained Raman ratios from these spectra are shown in Table 5.1. The I_D/I_G ratio, indicative of the amount of defects, is low, I_D/I_G = 0.35, right after graphene growth on 50 nm Mo catalyst layer on a quartz substrate. The number of defects increases as the graphene layer is post-processed. In particular, the I_D/I_G ratio increases during the Al patterning step. This step corresponds to the appearance of polymeric residues during the Al patterning process via sputtering and wet etching, as explained in section 4.1.2. The removal of these residues by scrabbing the surface might have caused slight damage to the graphene layer. The I_{2D}/I_G ratio is, in all cases, lower than 1, confirming the presence of multilayer graphene. Additionally, the single-peaked nature of the 2D peak strongly suggests that the graphene layers are turbostratic, as they do not exhibit the complex splitting of more ordered stacking [75]. Turbostratic graphene refers to a type of multilayer graphene with random or misordered stacking, leading to a weaker interlayer interactions.

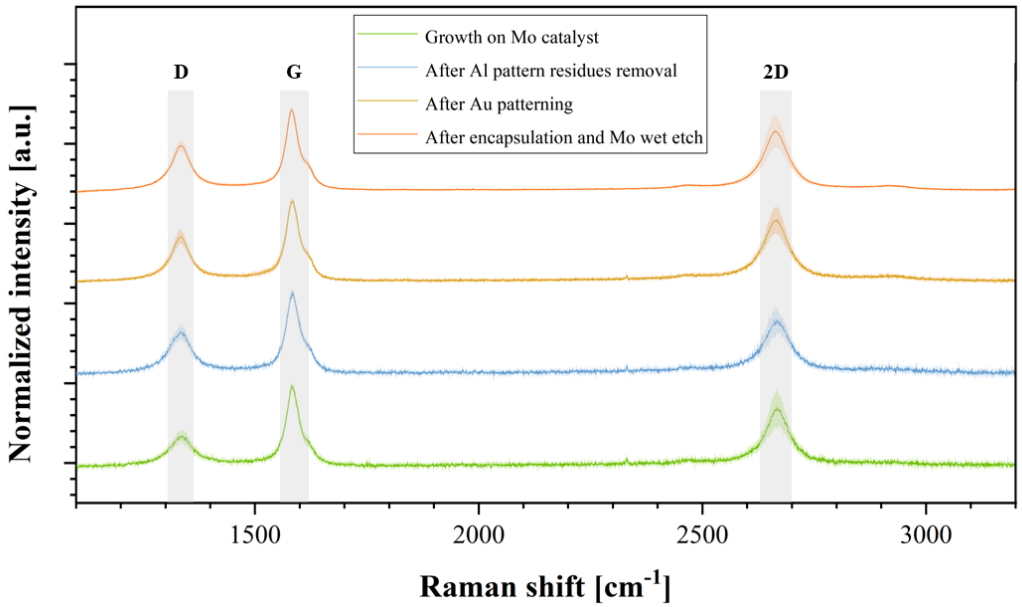

Figure 5.1: Raman spectra of the transfer-free multilayer graphene obtained at different stages of the process. Each graph line shows the average and standard deviation of 5 point measurements.

Process stage	I_D/I_G *ratio*	I_{2D}/I_G *ratio*
Growth on Mo catalyst	0.35 ± 0.09	0.72 ± 0.25
After Al pattern residues removal	0.49 ± 0.11	0.64 ± 0.21
After Au patterning	0.55 ± 0.14	0.78 ± 0.19
After encapsulation and Mo etch	0.50 ± 0.08	0.68 ± 0.10

Table 5.1: Raman ratios of transfer-free multilayer graphene obtained from the spectra at different stages of the process.

On top of that, Raman spectroscopy was used to reveal the presence of PEDOT:PSS coating on graphene microelectrodes. PEDOT:PSS Raman fingerprint has been previously reported, showing peaks between 1200 to 1600 cm^{-1}. In particular, vibration modes attributed to the symmetric and asymmetric C-C double bonds, C_α=C_β, stretching appear at 1425 cm^{-1} and 1536 cm^{-1}, respectively. The intra-thiophene ring stretching is reflected at 1369 cm^{-1}, whereas the inter-ring vibration corresponds to the 1260 cm^{-1} peak [76, 77].

After the microfabrication process was completed, Raman spectra were obtained in both graphene

and PEDOT:PSS-coated graphene electrodes. Fig. 5.2 shows the obtained average spectra from 5 point measurements in each electrode type. PEDOT:PSS-coated graphene electrodes show additional peaks between 1200 to 1600 cm^{-1} confirming the presence of PEDOT:PSS, which correlates with the Raman spectra reported in literature [76, 77].

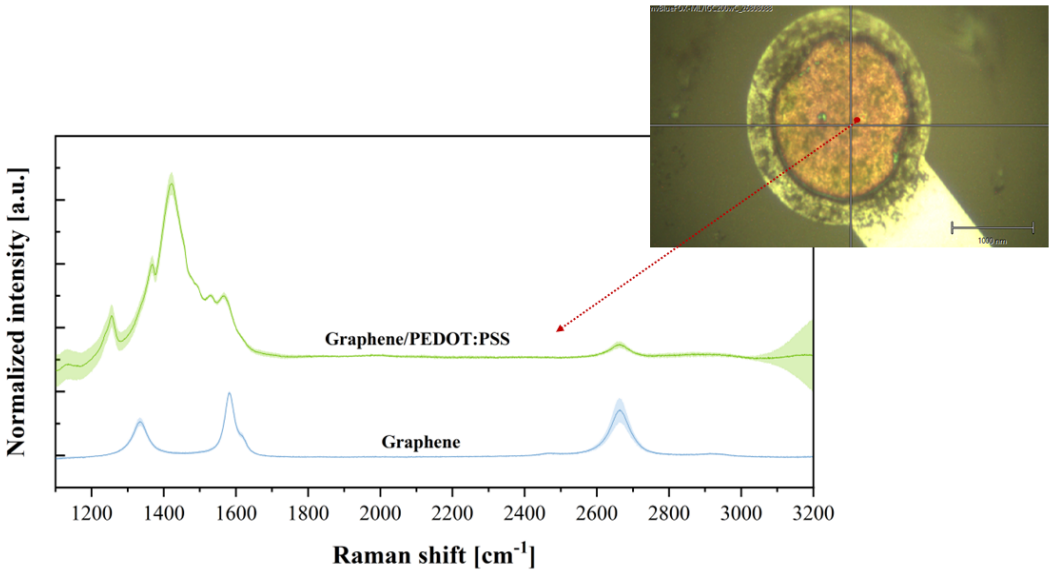

Figure 5.2: Raman spectra on the electrode openings of the fabricated MEA devices revealed graphene/PEDOT:PSS and graphene material compositions. Each graph line shows the average and standard deviation of 5 point measurements.

5.2. Sheet resistance and optical transparency analysis

The electrical and optical properties of the grown graphene material were also studied in this research work.

SHEET RESISTANCE MEASUREMENTS

Van der Pauw (VdP) structures were included in the mask design in order to characterize the electrical conductivity of the graphene tracks. VdP structures, used as a four point measurement method, allow to determine the sheet resistance of the material of interest with no contribution from the needles contact resistance. Fig. 5.3 b shows an image of a VdP structure with the probe needles landed on the contact pads. A Cascade Microtech probe station with a parameter analyzer was used for the measurements. A sweeping voltage from -0.5 to 0.5V was forced in the contact A, and contact B was clamped to GND, thereby forcing a current over contacts A and B. The voltage drop between the contact pads C and D was measured, and the resulting resistance, $R_{AB,CD}$, was obtained. The sheet resistance, R_s, from a symmetrical VdP structure can be calculated through the expression below [78]:

$$R_s = \frac{\pi}{ln2} R_{AB,CD}$$

The sheet resistance of multilayer graphene was previously evaluated by Romijn et al. [79] and reported to be around 900 Ω/sq. In this current work, the conductivity of multilayer graphene on Mo was measured, reflecting the expected conductivity for the Mo/graphene inner tracks. Fig. 5.3c shows the average of four sheet resistivity measurements. An average value of 11.37 Ω/sq was obtained. This suggests that the conductivity of Mo predominantly contributes to the overall track resistance. It is important to note that this value may not be reliable for long-term use, as the molybdenum layer is prone to biodegradation. However, this is not a significant concern for the present study, which focuses on acute recordings. In electrode recording systems, signal sensitivity is typically governed by impedance rather than the sheet resistance of the tracks, especially when highly conductive metals like gold are used. In this case, however, the biodegradability of the molybdenum track could lead to instability in electrical properties over time. Therefore, a thorough analysis of the electrochemical and

long-term stability of the molybdenum track would be critical for ensuring the overall reliability of the MEA devices.

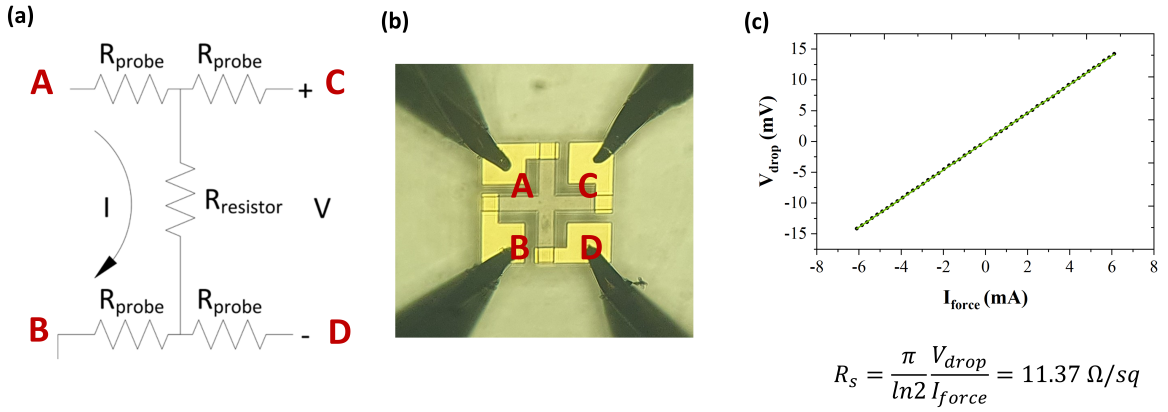

Figure 5.3: (a) Four-point measurement configuration. There is no contribution from the needles contact resistance due to their high impedances that prevent the passage of current through them. **(b)** Microscope image of a Van der pauw (VdP) structure with the probe needles landed on the pads. The Ti/Au square contact pads allow the sheet resistance measurement of graphene on Mo. **(c)** Measured I-V response of graphene/Mo test structures and resulted average sheet resistance value, reflecting the expected conductivity for the MEA inner tracks.

OPTICAL TRANSMITTANCE ANALYSIS

Transparency is a desirable property for neural interfaces that are targeting optogenetic applications or optical imaging of neural tissue. Among other characteristics, graphene was selected for its high optical transparency. Specifically, monolayer graphene is known to absorb only 2.3% of incident light [80]. In this study, CVD-grown multilayer graphene is used due to the capabilities of the CVD reactor and transfer-free graphene technology. To investigate the level of transparency of the final device, optical transmittance measurements were conducted. For these measurements, the graphene layer was transferred onto a 2 x 2 cm glass substrate. The details of the graphene transfer process are thoroughly described in Appendix subsection A.2.2.

PerkinElmer Lambda 1050+ UV/VIS/NIR spectrometer was used to evaluate the optical transmit-

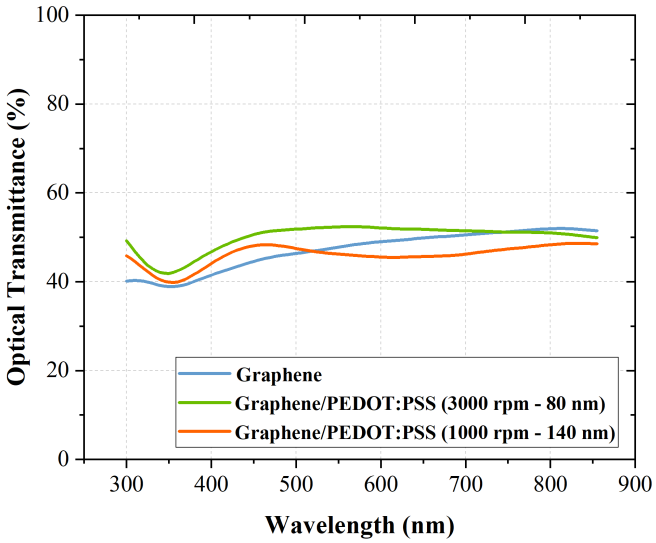

Figure 5.4: Optical transmittance measurements of transfered graphene and PEDOT:PSS-coated graphene sheets. The contribution from the glass substrate is removed. PEDOT:PSS was spin coated at 3000 and 1000 rpm, leading to a thickness of 80 and 140 nm, respectively. See Fig. A.3 in Appendix for the specific PEDOT:PSS thickness calibration curve.

tance of graphene and graphene/PEDOT:PSS samples. Transmittance data over a wide range of wavelengths, from 300 nm to 860 nm, was obtained. Measurements were taken for graphene and graphene/PEDOT:PSS samples, as well as only glass sample, allowing the isolation of the glass's contribution.

The measured optical transmittance values for graphene and PEDOT:PSS-coated graphene samples are depicted in Fig. 5.4. Across the entire spectrum, transparency levels of approximately 50% were recorded. At a wavelength of 550 nm, a transmittance of 47.5% was obtained, corresponding to an absorbance of 52.5%. Given that a single graphene layer absorbs 2.3% of light [80], a linear approximation was used to estimate the total number of graphene layers. Based on this calculation, the graphene sample was estimated to consist of approximately 23 layers. Previous reports using the same CVD reactor, catalyst layer, and growth recipe indicated thinner graphene stacks with around 7 layers, achieving transparency values of 83.5% [18]. Part of this variation could be attributed to the use of different substrates (quartz instead of silicon), though this does not fully account for the significant increase in layer thickness. One potential contributing factor could be the aging of the quartz tube, among other variables. Over time, the quartz tube may accumulate residues from previous runs or undergo surface degradation, subtly impacting gas flow dynamics and heat transfer within the reactor. These changes can, in turn, affect the CVD process and influence the quality and thickness of the graphene stack. A systematic review of the reactor's thermal profile, gas flow system, and the condition of the quartz tube would help ensure consistent and reproducible graphene growth.

Interestingly, PEDOT:PSS-coated graphene sheets spun at 3000 rpm exhibited a slight increase in transmittance in the lower wavelength range. This may be due to optical interference caused by variations in the refractive indices of the materials. Nevertheless, the graphene/PEDOT measurements remain consistent, as greater polymer thicknesses resulted in a small reduction in transparency (a 6.12% decrease at 550 nm when the thickness increased from 80 nm to 140 nm).

5.3. Electrochemical impedance spectroscopy (EIS)

Electrochemical impedance spectroscopy (EIS) was used to evaluate the electrochemical performance of the electrodes. The measurements were performed with a three-electrode setup and using phosphate-buffered saline (PBS), PBS 1X pH 7.4, as the electrolyte solution. The three-electrode setup consisted

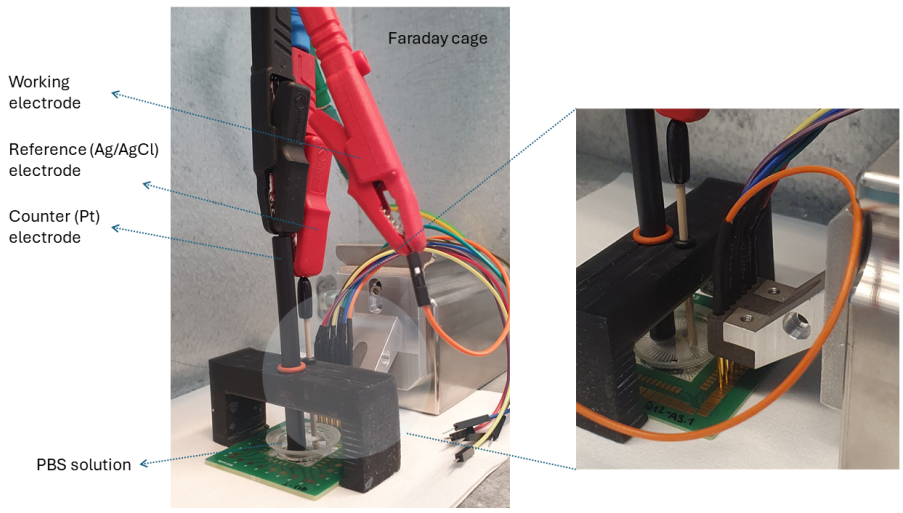

Figure 5.5: Three-electrode setup. A Pt electrode (3 mm diameter (BASI Inc.)) was used as a counter electrode, a leakless miniature silver/silver chloride (Ag/AgCl) (eDAQ) as a reference electrode, and the fabricated grMEA and grppMEA electrodes as the working electrodes. The connection to the working electrodes was established through spring-loaded pins, ensuring efficient contact with the MEA pads.

of: a working electrode (WE) where the reaction occurs, a counter electrode (CE) which creates a return path for the current, and a reference electrode (RE) which provides a stable potential for accurate measurement. A Pt electrode (3 mm diameter (BASI Inc.)) served as the CE, a leakless miniature silver/silver chloride (Ag/AgCl) (eDAQ) as RE, and the fabricated grMEA and grppMEA electrodes as the WE. The connection to the working electrodes was established through spring-loaded pins, ensuring efficient contact with the MEA pads. All the electrodes were connected to a potentiostat (Autolab PGSTAT302N) and kept inside a Faraday cage, as illustrated in Fig. 5.5. A 10 mV sine-wave voltage was applied between the WE and RE, and the current between the WE and CE was measured. The impedance magnitude and phase over a range of frequencies (from 1 Hz to 100 kHz) was recorded.

EIS measurements were performed on 10 electrodes with 50 µm diameter, for each case, grMEA and grppMEA, and the obtained averaged graphs can be found in Fig. 5.6. The EIS magnitude graph of grppMEA follows typical impedance behaviour of neural recording electrodes, with an increase in impedance magnitude at higher frequencies (resistance-dominated region) and capacitive-like behaviour at lower frequencies. In the case of grppMEA electrodes, a substantial reduction in the impedance magnitude is observed across the whole frequency range. Average impedance magnitude at 1 kHz, which is the typical frequency range of neural activity, was reduced from 247.21 kΩ for grMEA to 12.65 kΩ for grppMEA. This can be attributed to the volumetric capacitive behaviour of the PEDOT:PSS layer, providing a larger effective surface area and lower interface impedance for charge transfer. At lower frequencies impedance goes high because the double layer capacitance dominates the overall impedance.

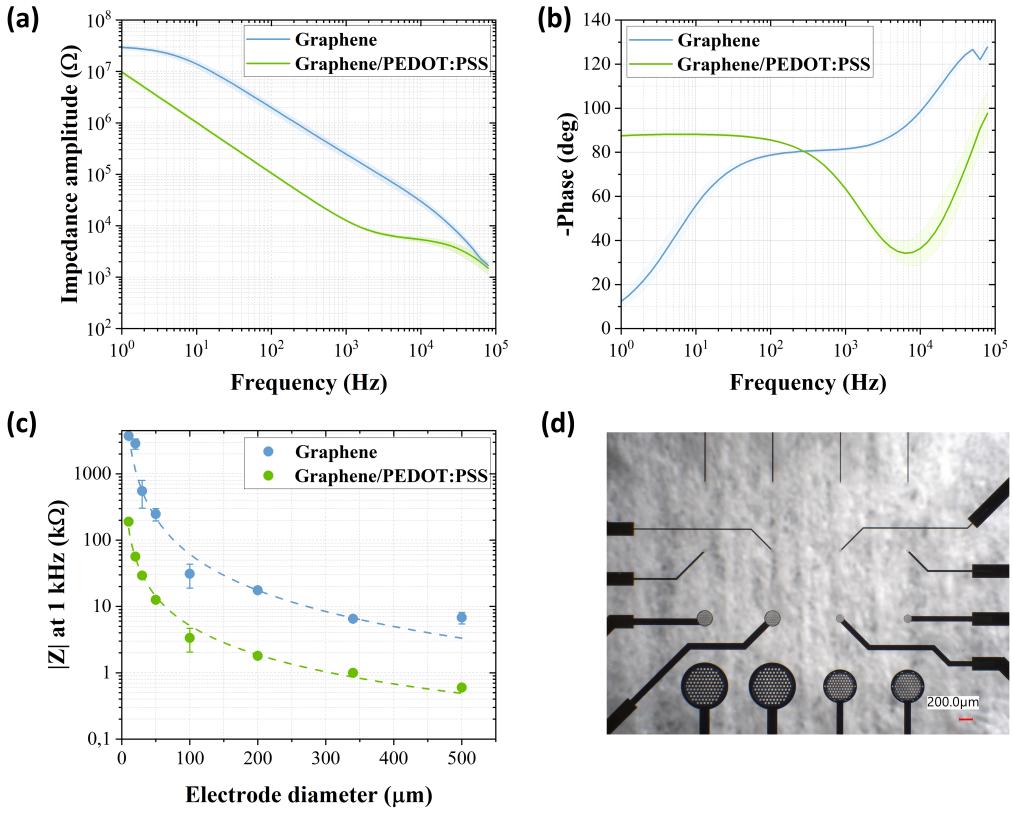

Figure 5.6: Electrochemical impedance spectroscopy (EIS) data of grMEA and grppMEA electrodes. **(a) EIS magnitude.** The measurements correspond to an average of 10 electrodes with a size of 50 µm diameter. **(b) EIS phase** The measurements correspond to an average of 10 electrodes with a size of 50 µm diameter. **(c)** Impedance magnitude at 1 kHz of various electrode sizes, ranging from 10 µm to 500 µm in diameter. The dotted lines represent the fitting functions of the data points. Further details on the fitting function are provided in Appendix B.1. **(d)** Optical image of the *Test MEA* featuring electrodes of different sizes.

In the impedance phase graph (Fig. 5.6b), the capacitive and resistive properties of the electrode material are more clearly observed. In case of grppMEA electrodes, the phase shift at lower frequencies is approximately -90 degrees, suggesting a pure capacitive behaviour, in contrast to the more resistive behaviour of multilayer graphene electrodes, with the phase shift dropping down to almost 0. However, such behaviour can be originated from several factors: (1) that the resistive component of the impedance is larger than the capacitive component at low frequencies, leading to a situation where the overall impedance behaves primarily as a resistor. (2) There could be several resistive and capacitive components interacting within the system, contributing to the overall impedance. The averaging of different contributions could result in a net phase angle that approaches 0° without necessarily indicating that the system is purely resistive. Additionally, the upward shift in EIS phase at high-frequencies may be attributed to artifacts from the instrumentation setup, such as cables and voltage or current amplifiers, which can introduce phase distortions resembling inductive behavior [81, 82]. An equivalent circuit model fitted to the obtained experimental results would be needed to fully describe the observed impedance characteristics.

	Impedance magnitude at $1kHz$ $(k\Omega)$							
Electrode diameter (μm)	10*	20*	30	50	100	200*	340*	500*
Graphene	3724.82 ± 286.14	2861.98 ± 501.16	550.23 ± 246.63	247.21 ± 52.31	31.13 ± 12.18	17.59 ± 0.10	6.51 ± 0.14	6.78 ± 1.35
$Graphene/PEDOT:PSS$	189.83	56.65 ± 0.05	29.05 ± 0.79	12.65 ± 0.81	3.36 ± 1.31	1.81 ± 0.17	1.04	0.61 ± 0.06

Table 5.2: Impedance magnitude at 1 kHz $(k\Omega)$ of grMEA and grppMEA electrodes of various sizes. * The average and standard deviation are calculated from only 1-2 electrode measurements, limited by the number of electrodes available on the *Test MEA*. Measurements for 30, 50 and 100 µm, instead, correspond to the average of 10 electrodes.

The impedance dependency on electrode size was also studied, by measuring the EIS response of different sizes of grMEA and grppMEA electrodes, ranging from 10 to 500 µm in diameter. Fig. 5.6c shows the average impedance magnitude at 1 kHz plotted against the electrode diameter. The impedance magnitude decreases with increasing electrode size, as expected, following an inverse relationship. The corresponding numerical values are summarized in Table 5.2. Moreover, the data points were fitted into a power function, described in Appendix B.1. It should be noted that the average and standard deviation of some of the electrodes were calculated from only 1-2 electrode measurements, limited by the number of electrodes available on the *Test MEA* (see Fig. 5.6d). For a more conclusive evaluation, a larger sample size would be required.

On top of that, the volumetric capacitance of PEDOT:PSS-coated graphene electrodes, grppMEA, was analyzed, which shows a quantitative measure of ion uptake from the electrolyte through the conductive polymer. The volumetric capacitance was extracted based on the impedance data at the lowest frequency point, 0.1 Hz. At this frequency, the total impedance is dominated by the double-layer capacitance at the electrode-electrolyte interface. The following equation was employed to calculate the capacitance:

$$Z = Z_C = \frac{1}{j2\pi fC} \rightleftharpoons C = \frac{1}{j2\pi fZ}$$

where Z denotes the complex impedance, f represents the frequency (0.1 Hz), and C is the capacitance. The capacitance values were normalized to the volume of the electrode, which was determined by multiplying the electrode area by the thickness of the PEDOT:PSS layer. The thickness was estimated based on the spin-coating speed, as illustrated in Fig. A.3 in Appendix. A spin speed of 1000 rpm produced a polymer thickness of approximately 140 nm. Volumetric capacitance values were calculated for electrodes of varying sizes, with the results presented in Fig. 5.7. The resulting volumetric capacitance for the grppMEA electrodes was 55.7 F/cm^3. The linear relationship between the capacitance and electrode volume suggests that the ionic charge uptaken from the electrolyte is uniformly distributed within the PEDOT:PSS layer. PEDOT:PSS electrodes reported in literature showed a volumetric capacitance of 39 F/cm^3 [83, 84].

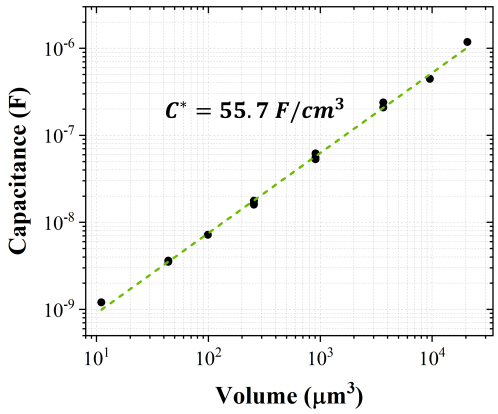

Figure 5.7: Volumetric capacitance of PEDOT:PSS-coated graphene electrodes, grppMEA. Capacitance values from the EIS data at the lowest frequency point, 0.1 Hz, were extracted at different electrode volumes. The volume was determined by multiplying the electrode area by the thickness of the PEDOT:PSS layer, 140 nm. The resulting capacitance was 55.7 F/cm^3.

5.4. Cyclic voltammetry (CV)

Cyclic voltammetry technique was used to assess the reversibility of the electrochemical reactions on the electrode of interest and to determine the amount of charge that can be stored reversibly. The same three-electrode setup, as shown in Fig. 5.5, was used for these measurements. The water window, which defines the potential range within which water remains stable and avoids electrolysis, was experimentally determined and adapted for each MEA device. CV measurements at several scan rates were taken: at 0.1, 0.2, 0.6 and 1 V/s. The scan rate plays a role in the formation of a diffusion layer in the electrode-electrolyte interface and thus, the electrons transfer and current response of the electrode. The I-V curve was recorded and from it, the charge storage capacity (CSC) was computed.

The CV results for grMEA and grppMEA electrodes are displayed in Fig. 5.8. At lower scan rates,

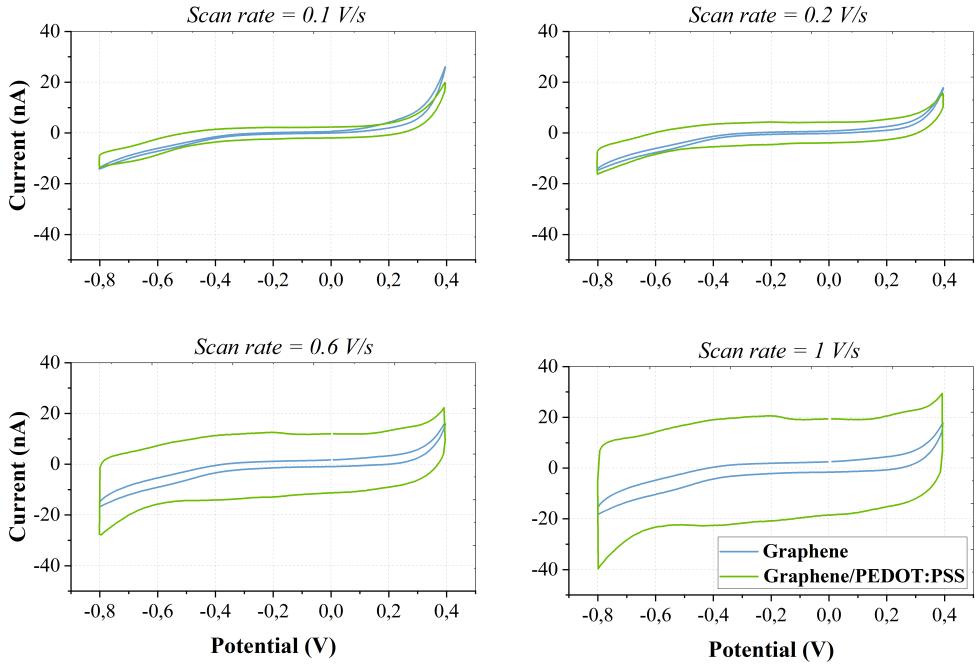

Figure 5.8: Cyclic voltammetry (CV) curves of graphene and graphene/PEDOT:PSS electrodes. Electrodes with a diameter of 50 µm were characterized with scan rates of 0.1, 0.2, 0.6 and 1 V/s.

the diffusion layer becomes thicker as more ions diffuse to the electrode surface, decreasing the concentration of reactants at the interface and consequently lowering the current response. In contrast, higher scan rates result in a thinner diffusion layer, allowing for greater current densities. The current dependency on scan rate is further analyzed in Appendix Fig. B.3. The capacitive behavior of the PEDOT:PSS coating is more prominent at higher scan rates, where the CV curve adopts a box-like shape, in contrast to the more elongated CV profile of bare graphene, which is indicative of faradaic processes. The water window was maintained between -0.8 V and 0.4 V to prevent undesirable electrochemical reactions. The charge storage capacity (CSC) for each electrode was calculated by integrating the area under the CV curve within this water window. The average CSC values for the grMEA and grppMEA electrodes are provided in Table 5.3.

	$CSC\ total\ (\mu C/cm^2)$			
	0.1 V/s	0.2 V/s	0.6 V/s	1 V/s
$Graphene$	2585	1106	430	297
$Graphene/PEDOT:PSS$	5576	3304	2620	2544

Table 5.3: Total CSC values for grMEA and grppMEA electrodes, with a diameter of 50 µm, obtained at different scan rates.

A comparison of previously reported transparent electrodes for neural interfaces with the grMEA and grppMEA electrodes reported in this current work is provided in Table 5.4.

Electrode material	*Electrode surface area* (μm^2)	*Impedance at 1kHz* ($k\Omega$)	*Area − normalized impedance* ($\Omega \cdot cm^2$)	*Transparency* (%)	*Reference*
Monolayer graphene doped with acid nitric	2500 (50x50)	541	13.5	90	Kuzum et al. 2014 [38]
Four-layer graphene	31416 (D=200)	215.7 ± 120.4	67.76 ± 37.82	90	Park et al. 2018 [36]
Two-layer graphene doped with acid nitric	2500 (50x50)	908	22.7	90	Driscoll et al. 2021 [45]
Interlayer-doped double-layer graphene with Pt NPs	314 (D=20)	250 ± 56	0.78 ± 0.18	90	Ramezani et al. 2024 [40]
Transfer-free multilayer CVD graphene (on quartz substrate)	707 (D=30)	3200 - 9890	21.11 - 69.91	80	León González et al. 2023 [20]
Transfer-free multilayer CVD graphene (on Si substrate)	68320 (D=340)	27.4 ± 7.5	18.72 ± 5.23	83.5	Babaroud et al. 2022 [18]
Transfer-free multilayer CVD graphene with 40% Pt NPs	68320 (D=340)	7.26 ± 0.95	4.96 ± 0.61	∼ 70	Babaroud et al. 2023 [48]
Monolayer graphene coated with PEDOT:PSS	707 (D=30)	166 ± 13	1.17 ± 0.09	84	Kshirsagar et al. 2019 [47]
PEDOT:PSS	707 (D=30)	56 ± 8	0.39	75	Middya et al. 2021 [85]
Transfer-free multilayer CVD graphene	1825 (D=50)	247.21 ± 52.31	4.51 ± 0.95	50	This work
Transfer-free multilayer CVD graphene coated with PEDOT:PSS	1825 (D=50)	12.65 ± 0.81	0.23 ± 0.01	50	This work

Table 5.4: Transparent neural recording arrays. Comparison of previously reported transparent electrodes with the graphene and PEDOT:PSS-coated graphene electrodes reported in the present work.

5.4.1. Electrochromism and Delamination

Conductive polymers exhibit redox states with different electronic absorption spectra [86]. Upon applying a potential, the conductive polymer can undergo reversible oxidation (loss of electrons) and reduction (gain of electrons) leading to changes in the optical gap, which translates into a reversible color change. This phenomenon is known as *electrochromism*, and it has been used to monitor doping/dedoping effects in conducting polymer films [87, 88], as well as to study the ion mobility within the polymer matrix [89].

During electrochemical measurements (EIS and CV), visual color changes on the grppMEA electrodes were observed, as shown in Fig. 5.9. The passage of current changed the electrochemical doping state of the PEDOT:PSS film, inducing a reversible color variation. The color changes were also observed just by immersing the electrodes in the PBS electrolyte, indicating that the polymer film is sensitive to the ionic environment.

In addition to the electrochromic effect, signs of partial delamination of the PEDOT:PSS film from the graphene surface were observed during electrochemical cycling. The non-uniform color distribution across the electrode surface suggested that the polymer film experienced partial detachment, likely due to mechanical instability during cycling. This delamination can be attributed to inadequate adhesion between the graphene and PEDOT:PSS layers. Several factors are critical for ensuring proper adhesion of PEDOT:PSS coatings to substrates, including the preparation of the PEDOT:PSS solution, surface activation of the substrate (such as oxygen plasma treatment) prior to coating, and appropriate thermal annealing after deposition. Oxygen plasma treatment, commonly used to introduce -OH groups on the surface, enhances hydrophilicity and promotes strong covalent bonding between the silane groups in GOPS, the crosslinking agent in PEDOT, and the substrate. However, in the present study, no surface activation techniques were employed, as oxygen plasma can degrade or even completely etch the graphene layer. This omission likely compromised the long-term stability of the PEDOT:PSS films. Exploring alternative surface activation methods, such as UV ozone treatment, may offer a viable approach to improving adhesion at the graphene-PEDOT:PSS interface without compromising the integrity of the graphene.

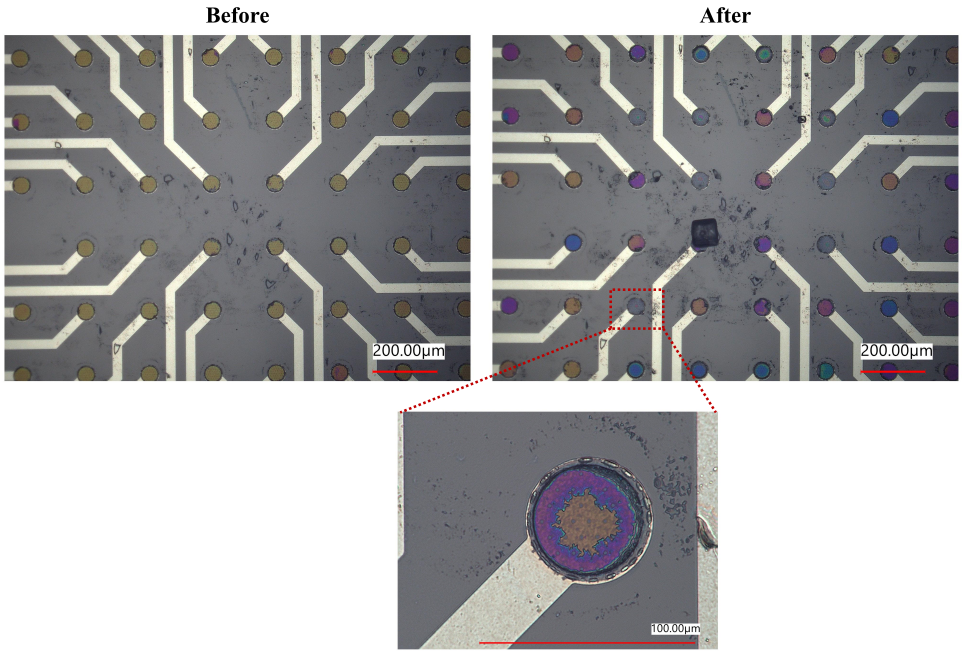

Figure 5.9: Optical images of PEDOT:PSS-coated graphene electrodes before and after electrochemical measurements. A visual color change on the electrodes after electrochemical cycling was observed, partially attributed to the electrochromic nature of PEDOT:PSS polymer. The non-uniform color distribution across the electrode surface suggested that the polymer film experienced partial delamination, likely due to poor adhesion to the graphene layer.

5.5. Summary

Raman spectroscopy confirmed the presence of multilayer graphene with increasing defects (I_D/I_G ratio) as the fabrication process progressed, particularly after Al patterning, while the I_{2D}/I_G ratio remained below 1, indicating multilayer graphene. Additionally, Raman analysis revealed the successful coating of PEDOT:PSS on graphene microelectrodes, identified by characteristic peaks between 1200 and 1600 cm^{-1}. The sheet resistance of multilayer graphene on Mo tracks was measured at 11.37 Ω/sq, with Mo contributing significantly to conductivity, though its biodegradability may impact long-term stability. Optical transmittance measurements showed that transparency remained around 50% across the entire spectrum, and the PEDOT:PSS coating did not significantly affect the transparency.

EIS demonstrated that grppMEA electrodes exhibited a substantial reduction by 10-20 times in impedance magnitude compared to grMEA electrodes, due to the capacitive properties of the PEDOT:PSS layer. Impedance decreased further with increasing electrode size, following an inverse relationship. Additionally, the volumetric capacitance of the grppMEA electrodes was calculated to be 55.7 F/cm^3 at 0.1 Hz, indicating high ion uptake from the electrolyte. CV revealed that the incorporation of PEDOT:PSS significantly increased the CSC values, with grppMEA electrodes achieving a CSC of 5576 µC/cm² at 0.1V/s, more than double that of grMEA electrodes, which had a CSC of 2585 $\mu C/cm^2$. Visual observations during electrochemical measurements indicated reversible color changes in the electrodes, likely resulting from a combination of electrochromism and partial delamination of the PEDOT:PSS layer. Overall, the results obtained in this study are comparable to state-of-the-art findings for transparent neural interfaces.

6

Electrophysiological recordings of neuronal activity

In *in vitro* and *ex vivo* applications, MEAs are widely used to investigate a variety of neurophysiological processes, from understanding basic synaptic function to studying complex network dynamics. In *in vitro* systems, MEAs facilitate the study of neuronal cultures, where they are commonly used to track the development of neural networks, assess synaptic plasticity, and evaluate the effects of pharmacological agents on neuronal firing patterns, among other applications. In *ex vivo* settings, MEAs are frequently employed to study acute brain slices or organotypic cultures, where the preserved architecture of the neural tissue allows for detailed exploration of brain region-specific activity. This chapter delves into the application of the fabricated MEA devices for registering extracellular activity from cerebellum brain slices. For this purpose, a custom-made interface that effectively connects the MEA devices to specific recording system and enables the acquisition of neural signals is first presented. Then, the electrophysiological recording capabilities of the fabricated grMEA and grppMEA devices is evaluated.

6.1. MEA electrophysiology recording system

The fabricated MEA devices enable the transduction of ionic currents generated by neural activity into electrical signals. However, these bioelectrical signals require real-time amplification, filtering, and digitization across multiple channels to be accurately recorded and analyzed. While there are numerous commercially available systems for electrophysiological signal acquisition, such as the TDT neurophysiology system and the Intan Technologies recording system, their designs are not always optimized for seamless integration with MEA platforms. To address this challenge, a custom-designed interface was developed to effectively connect the MEA devices to commercially available recording hardware from Intan Technologies.

The complete acquisition setup, illustrated in Figure Fig. 6.1a, comprises a custom-printed circuit board (PCB) designed to interface the MEA pads with Omnetics connectors compatible with the Intan system. Two 32-channel Intan recording headstages (RHD2132 chips) are connected to the Omnetics connectors, which in turn interface with the RHD USB Interface Board. This board is subsequently connected to a computer running RHX Data Acquisition Software, enabling real-time data collection and analysis.

The custom PCB is a four-layer board, incorporating dedicated grounding for noise reduction and signal integrity. It supports up to 60 recording channels and is designed to be compatible with both the fabricated graphene-based MEAs (grMEA and grppMEA) as well as standard 60-channel commercial MEAs from Multichannel Systems. Spring-loaded pins, which are soldered to the custom PCB, ensure reliable electrical contact with the MEA pads and route these connections to the Omnetics connectors, facilitating communication with the two Intan 32-channel headstages. Additionally, the PCB includes a power delivery circuit with a buffered reference, designed for stimulation applications. Although this

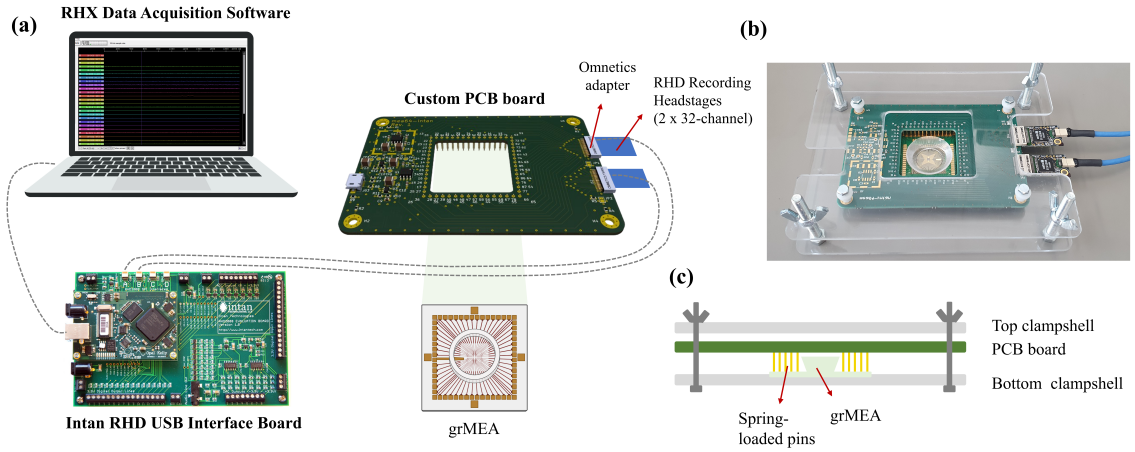

Figure 6.1: Overview of the MEA acquisition system setup. (a) Schematic representation of the connections between the custom PCB board and the Intan recording system. The custom PCB board allows to couple the MEA electrodes, up to a total of 64, to the recording channels from Intan headstages. Spring-loaded pins, soldered to the custom PCB, effectively contact with the MEA pads and route these connections to the Omnetics adapter pads, and in turn to the Intan recording headstage pins. **(b)** Image of the assembled MEA-to-Intan interface. **(c)** Cross-sectional illustration of the MEA-to-Intan interface. The mechanical parts (top and bottom clampshells) ensure a good contact between the spring-loaded pins from the custom PCB and the MEA pads.

feature was implemented, it was not utilized in the present work. The custom PCB board was designed by Lukas Holzapfel from the TU Delft - Fraunhofer IZM research group.

To ensure stable mechanical coupling between the MEA and the custom PCB, laser-cut components were fabricated from 2 mm-thick plexiglass sheets. These components were designed to securely host the MEA while maintaining proper alignment between the MEA pads and the spring-loaded pins on the PCB. By applying pressure through screws mounted on the assembly, the spring-loaded pins are pressed against the MEA pads, ensuring reliable and consistent electrical contact. Fig. 6.1b,c provides an image of the fully assembled MEA-to-Intan interface, along with a cross-sectional schematic of the system.

6.2. Cerebellar brain slice recordings

The *in vitro* performance of the grMEA and grppMEA devices was evaluated by recording neural activity from acute mouse cerebellar brain slices. The cerebellum was selected as a model system due to its well-characterized spontaneous spiking activity patterns, which are dominated by the firing of Purkinje cells. These cells exhibit regular and rhythmic spikes at a relatively constant and high frequency of around 30 to 50 Hz [90]. Given the predictable spiking activity of Purkinje cells, assessing the sensitivity of the fabricated grMEA and grppMEA devices to capture their electrical signals can be feasibly achieved. Moreover, the relatively short lifetime of these cells, approximately 4-5 hours post-slicing, is advantageous for our purposes, as it minimizes the duration that the microfabricated device is subjected to physiological conditions, reducing the likelihood of failure. The brain slice culture activity recording test was done in collaboration with the Erasmus MC Neuroscience Department.

The MEA-to-Intan interface system described in the previous section was used to acquire extracellular recordings from the acute cerebellar brain slices. The complete setup was placed inside a Faraday cage to minimize electromagnetic interference. The ground pin of the Intan RHD USB Interface Board was connected to the Faraday cage to establish a common ground reference. Prior to recording from a slice, a baseline signal was acquired for several minutes to assess the noise level of the system. Subsequently, a slice was carefully positioned onto the grMEA or grppMEA surface. To ensure close contact between the slice and the MEA, a slice anchor with parallel nylon fibers was gently pressed onto the tissue. Artificial cerebrospinal fluid (aCSF) was manually perfused over the slice to maintain tissue viability. Extracellular recordings were performed at a sampling rate of 20 kHz per channel.

The acquired data was post-processed with a custom Matlab script to filter and analyze the neural signals. The first step involved filtering the signals using a second-order Butterworth filter, with a passband ranging from 5 Hz to 1000 Hz, effectively isolating the frequency components relevant to neuronal activity. To eliminate any phase distortion introduced by the filtering process, a phase-correction algorithm was applied, ensuring that the temporal integrity of the neural signals was preserved. Next, spike detection was performed using a thresholding method based on the median absolute deviation (MAD) of the filtered signal. The MAD is a measure of variation that reflects the mean of the absolute amplitude values of deviation of each time point relative to the median. A detection threshold was set at 6 times the MAD. To avoid detecting multiple spikes within the same action potential event, a refractory period of 2.5 ms was applied. The refractory period of a neuron refers to the period after an action potential during which the neuron is unable, or less able, to fire another action potential. Finally, the signal-to-noise ratio (SNR) was computed by calculating the ratio of the maximum peak-to-peak amplitude of the neural spikes, $V_{pp,max,signal}$, to the standard deviation of the noise in the baseline signal, $V_{std,noise}$, as shown in the expression below:

$$SNR = 20 \cdot log \frac{V_{pp,max,signal}}{V_{std,noise}}$$

This metric provided a quantitative assessment of the recording quality, confirming the sensitivity of the grMEA and grppMEA devices in capturing neural activity.

Multiple recordings were performed using the grMEA devices, with electrodes of 30 µm and 50 µm in diameter, to evaluate their performance in capturing spontaneous neural activity from acute cerebellar brain slices. The characteristic spiking patterns of Purkinje cells and other neuronal populations were successfully recorded, as illustrated in Fig. 6.2c. A colormap representation of the SNR, Fig. 6.2d, was employed to spatially correlate the recorded signals to individual electrodes across the MEA array. This representation allows for the visualization of the peak neural activity areas within the cerebellar slice, allowing precise localization of more active neuronal regions.

In situ impedance measurements at 1 kHz were conducted on the device electrodes using the dedicated Intan hardware function. Artificial cerebrospinal fluid (aCSF) was used as the electrolyte. Measurements revealed impedance values of 526 $\pm$ 12.3 $k\Omega$ and 239 $\pm$ 20.6 $k\Omega$ at 1 kHz for 30 µm and 50 µm diameter electrodes, respectively. Electrodes with an impedance higher than 1 $M\Omega$, were considered as damaged and consequently excluded from the analysis. The average SNR values for functional grMEA electrodes were 19.38 $\pm$ 7.21 dB for the 30 µm diameter electrodes and 20.58 $\pm$ 6.10 dB for the 50 µm electrodes. The distribution of the obtained SNR values are depicted in Fig. 6.4. Despite the difference in electrode size, the SNR values in grMEA devices were found to be similar. This could be attributed to the inherent properties of smaller electrodes: while they are capable of detecting neural signals with higher amplitude likely due to less spatial averaging effect, they are also more susceptible to increased levels of noise. The averaging effect of the activity from multiple neurons over the whole electrode area is more prominent in large electrodes (i.e., with diameters greater than 100 µm) [91, 92]. This balance between heightened signal amplitude and noise likely explains the comparable SNR values across the two electrode sizes.

The recorded signals revealed that neural activity from a single neuron was often detected by neighboring electrodes, suggesting that the neuronal activity propagated across multiple electrodes. Additionally, variations in spike amplitude were observed within individual electrode recordings, indicating that multiple nearby neurons were being captured simultaneously, each contributing spikes of different magnitudes. These findings highlight the high spatial resolution of the MEA array, demonstrating its capability to detect and differentiate the activity of neurons located in close proximity.

It was also observed that the SNR was strongly dependent on the physical distance between the active neurons and the recording electrodes. For optimal SNR, it is crucial that the brain slice remains in tight contact with the MEA surface. However, during the experiments, the slice was found to gradually detach from the electrode surface due to the perfusion of artificial cerebrospinal fluid (aCSF). While the slice was anchored by a metal ring, slight lifting of the tissue from the MEA surface led to a reduction

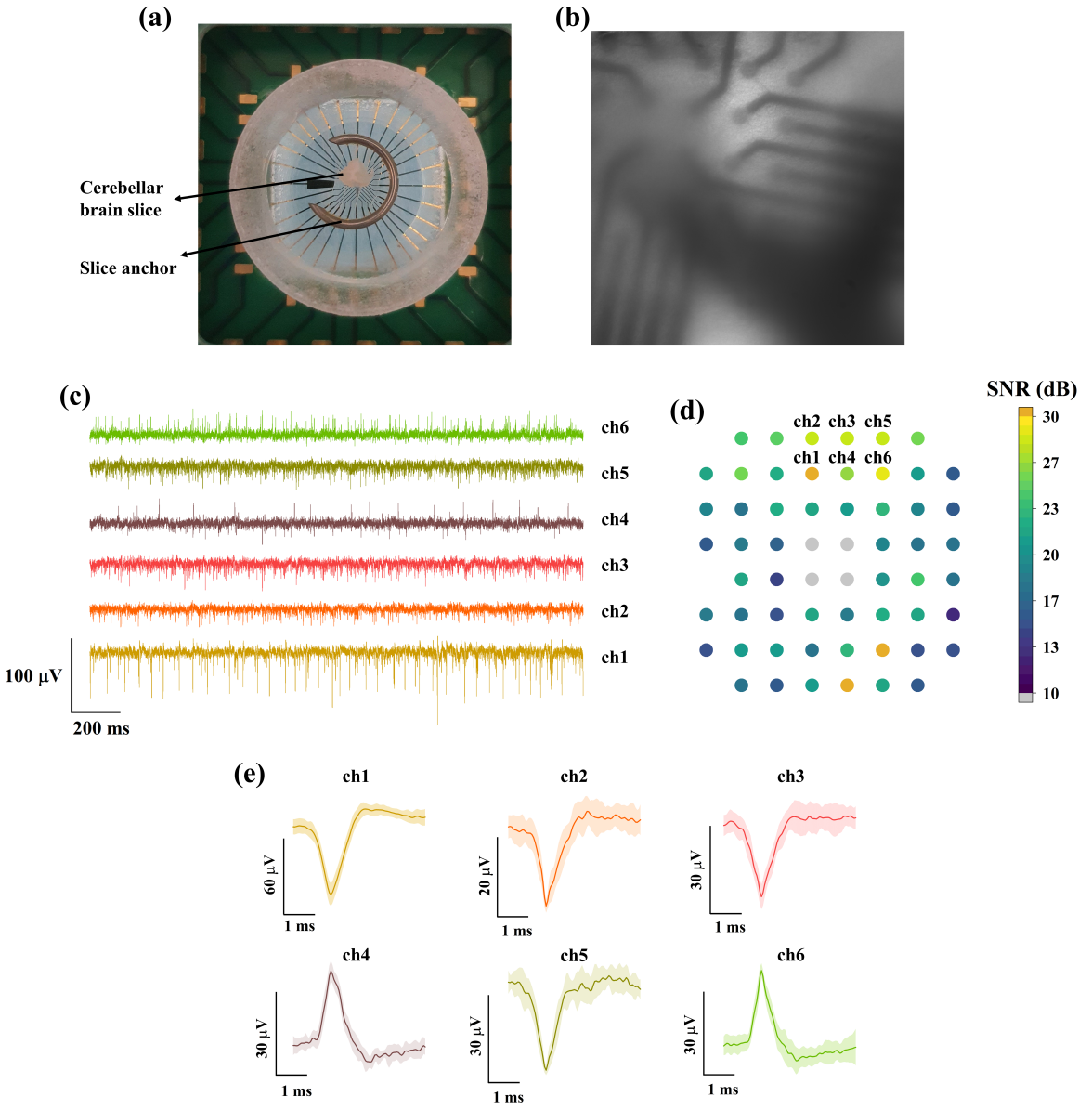

Figure 6.2: Electrophysiological recordings of neuronal activity from cerebellar brain slices. **(a)** Cerebellar brain slice mounted on the grMEA device. **(b)** High-resolution optical image of the edge of the brain slice positioned over the MEA, captured using an epifluorescence microscope. **(c)** Neural activity recorded by grMEA electrodes with a diameter of 50 µm, showing the activity of six distinct channels. **(d)** Colormap representation of calculated signal-to-noise ratio (SNR) values by grMEA electrodes with a diameter of 50 µm overlaid on the MEA. Electrodes marked in grey indicate damaged ones, defined by an impedance magnitude greater than 1 $M\Omega$ at 1 kHz. **(e)** Averaged detected spike waveforms corresponding to the recordings shown in (c).

in signal quality. On one occasion, immediately after placing the cerebellar slice onto the MEA with an initial drop of aCSF, a prominent spike with a peak amplitude reaching the mV range was observed, showcasing the high sensitivity and recording capabilities of the electrodes. This high-amplitude signal rapidly diminished, with subsequent spikes showing a marked decrease in amplitude, likely due to the gradual distribution of the fluid within the cell-electrode interface. This observation underscores the importance of effective neuron-electrode coupling. As the cells detach from the electrodes, the interspace, referred to as the *cleft*, increases and is filled by extracellular medium and thereby impacting the electrical properties of the interface. Specifically, the seal resistance decreases, which is the resistance to current leakage from the cell to the surrounding medium at the cell-electrode interface. This

results in a reduction in the amplitude of the recorded electrophysiological signal. Seal resistance is influenced by cleft distance, the resistivity of the electrolyte solution, and the coverage percentage (i.e., the fraction of the electrode surface in direct contact with neurons) [93].

Additionally, the brain slicing process, performed using a vibratome, may have contributed to a lack of uniformity in cell contact with the electrodes. The vibratome's slicing action, which detaches cells rather than making a clean cut, creates surface topography that likely further inhibited consistent contact between the cells and electrodes. This finding highlights the importance of electrode-tissue proximity. Ensuring tight and stable contact between the neuronal tissue and the electrodes is crucial for achieving high SNR and reliable neural recordings.

The recordings with the 30 µm diameter PEDOT:PSS-coated graphene electrodes, grppMEA, successfully captured some spikes, demonstrating their potential for detecting neural activity. However, the overall observations with both 30 µm and 50 µm diameter grppMEA electrodes revealed challenges in detecting individual spikes, despite the relatively low impedance of the electrodes. For instance, the 50 µm diameter grppMEA showed a significantly low impedance value of around 15 $k\Omega$ at 1 kHz, but during the recording experiments, individual spikes were not discernible. Even though the baseline noise levels were lower than those observed with the non-coated graphene MEA (grMEA) electrodes, the spike signals themselves were more difficult to isolate. This concept is reflected in Fig. 6.3. This raises questions about the interplay between electrode impedance and neural signal sensitivity in these coated electrodes.

One plausible explanation for these observations is that the grppMEA electrodes, while minimizing thermal noise due to lower impedances, may have heightened sensitivity to biological noise, particularly the collective activity of multiple neurons within the surrounding tissue. The PEDOT coating enhances the electrode's capacitive behavior, improving ionic-electronic interactions, but this may also lead to the detection of signals from a broader area of the brain slice. Consequently, the recorded signals could be a composite of local field potentials (LFPs) and the activity of nearby neurons, resulting in spatial averaging across the electrode surface [92], and thus, a loss on individual spike detection resolution. The larger 50 µm electrodes are particularly susceptible to this effect, as their increased surface area allows them to capture signals from a wider region, further contributing to the loss of spike resolution. While the SNR was relatively high in grppMEA electrodes, this calculation primarily reflects a reduction in thermal noise and does not account for biological noise.

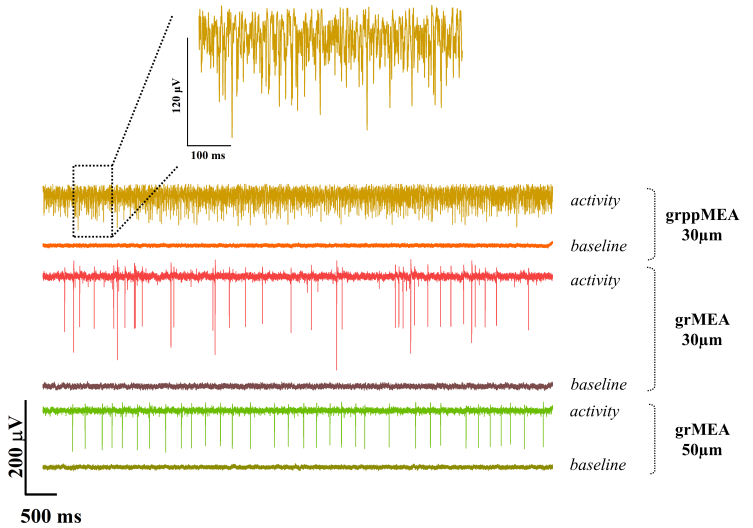

	Baseline V_{std}	Activity $V_{pp,max}$	SNR
$grppMEA\ 30\mu m$	± 1.2 µV	140 µV	41.3 dB
$grMEA\ 30\mu m$	± 2.6 µV	295 µV	41.3 dB
$grMEA\ 50\mu m$	± 1.8 µV	134 µV	37.3 dB

Figure 6.3: Baseline and neural activity recorded from grMEA and grppMEA devices with different electrode diameters. Representative channels from graphene-based MEAs (grMEA) and PEDOT:PSS-coated graphene MEA (grppMEA) displaying spontaneous activity with high and comparable SNR values are shown, along with the quality metrics for each recorded signal.

Several acute recordings of extracellular activity in cerebellar slices were conducted to assess signal quality across devices. The distribution of averaged SNR values obtained from these recordings is presented in Fig. 6.4, alongside the mean SNR for each tested MEA device. Overall, the grppMEA devices showed a higher average SNR, 29.31 ± 5.75 dB, compared to grMEA. This difference can likely be attributed to the ultralow impedance of the grppMEA electrodes, which enables them to detect collective neural activity from a broader area, increasing the likelihood of capturing spikes from both nearby neurons with high amplitude signals and more distant neurons with lower amplitude signals. In contrast, the higher impedance of grMEA electrodes confers greater selectivity for activity from neurons in closer proximity. This selectivity enhances the probability of detecting distinct, high-amplitude signals from nearby neurons while reducing the overall likelihood of capturing signals from more distant sources. Consequently, while grMEA devices may achieve clearer individual spike detection, the grppMEA's lower impedance allows for higher SNR through the integration of neural signals across a wider spatial area.

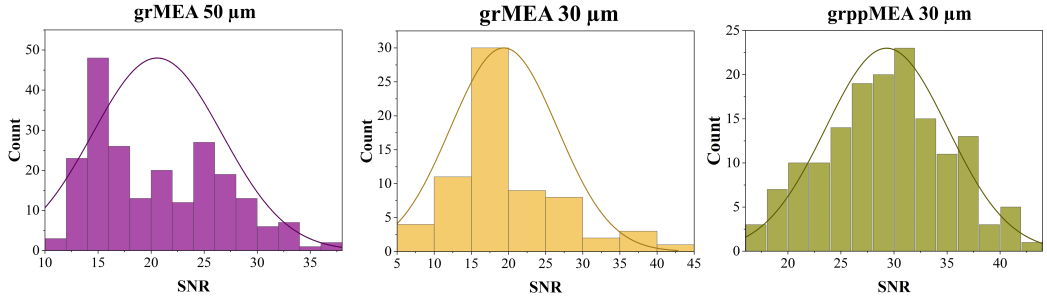

	$Average\ SNR\ (dB)$
$grMEA\ 50\mu m$	20.58 ± 6.10
$grMEA\ 30\mu m$	19.38 ± 7.21
$grppMEA\ 30\mu m$	29.31 ± 5.75

Figure 6.4: Histograms showing the distribution of SNR values for each tested MEA device type: grMEA with 30 µm and 50 µm diameter electrodes, and grppMEA with 30 µm diameter electrodes, recorded from cerebellar slice cultures. The accompanying table displays the average SNR values for each MEA device.

6.3. Summary

The fabricated graphene-based microelectrode arrays, grMEA and grppMEA devices, successfully captured spontaneous neuronal activity from acute mouse cerebellar brain slices, capturing the characteristic spiking patterns of Purkinje cells. The MEA-to-Intan interface allowed for real-time acquisition of extracellular neural signals. Recordings from grMEA electrodes resulted in average SNR values of 19.38 ± 7.21 dB and 20.58 ± 6.10 dB for 30 µm and 50 µm electrodes, respectively, and 29.31 ± 5.75 dB for grppMEA 30 µm electrodes, showcasing their sensitivity. While the grppMEA electrodes demonstrated lower impedance values (around 15 kΩ), they struggled to isolate individual spikes due to increased sensitivity to biological noise. Testing smaller grppMEA electrodes, such as those with a 10 µm diameter, may prove promising for better spike resolution by reducing the influence of nearby neuronal activity. Additionally, maintaining tight contact between the neuronal tissue and the electrodes was observed to be essential for optimal signal quality. Overall, the performed recordings underscore the potential of graphene and PEDOT:PSS-coated graphene electrodes to acquire electrophysiological signals with high sensitivity, paving the way for high-density recordings with single-cell resolution.

7

Conclusions and future prospects

7.1. Conclusions

In vitro MEA technology has become an essential tool for studying neural networks in cell cultures and brain slices, offering a non-invasive, long-term, and high-throughput platform for electrophysiological recordings. Although optical imaging techniques have been applied to gain more spatial information, they face challenges in capturing the rapid temporal dynamics of neuronal spiking activity. This study aimed to develop an optically transparent *in vitro* MEA platform through advanced microfabrication methods to support multimodal neural interfacing, while assessing its recording performance with neuronal cells. Novel microelectrode materials and architectures were explored to enhance the performance, applicability of MEA-based neural recording systems, as well as compatibility with optical techniques.

This work presented wafer-scale microfabrication processes to fabricate CVD multilayer graphene-based microelectrode arrays, grMEA, on a transparent substrate. Even though maintaining the integrity of graphene layer along the fabrication process is a challenge, Raman spectra analysis confirmed the presence of good quality graphene layer after the patterning and encapsulation steps. Electrochemical characterization of grMEA devices demonstrated low area-normalized impedance and relatively high CSC, indicating their suitability for neural recording applications.

To overcome the high impedance limitation when scaling down electrode size, an innovative hybrid electrode approach composed of graphene and a PEDOT:PSS conductive polymer coating, grppMEA, was developed. Besides enhancing the effective area of the electrode, the polymer coating provided increased ions-to-electrons transduction efficiency. A technique to selectively pattern the polymer layer on the microelectrode areas was presented based on parylene lift-off technique. The resulting grppMEA devices showed an impedance reduction by 10-20 times (e.g., from 247 kΩ to 13 kΩ for 50 µm diameter electrodes) and increased CSC values by more than the double compared to grMEA electrodes, enabling more efficient electrical coupling with neural tissue. Additionally, the volumetric capacitance of the graphene/PEDOT:PSS composite, comparable to that of PEDOT:PSS electrodes, indicated a high ion uptake from electrolyte.

The neural recording performance of graphene-based MEAs was validated through acute *in vitro* experiments using mouse cerebellar brain slices. Both grMEA and grppMEA devices were able to detect spontaneous extracellular neuronal spiking activity from neural cells with a high signal-to-noise ratio ($\sim$ 30 dB). The recorded signal quality was found to be more limited by the electrode-tissue proximity than the MEA technology itself. Ensuring tight and stable contact between the neuronal tissue and the electrodes was crucial for achieving high SNR and reliable neural recordings. In addition, the ultralow impedance of grppMEA electrodes minimized thermal noise but, due to their larger size relative to individual neurons, posed challenges for isolating single spikes. This was attributed to increased sensitivity to biological noise from nearby neurons. In contrast, grMEA devices with higher impedance proved more effective in resolving individual spikes. Smaller grppMEA electrodes that match single-

cell dimensions may offer improved spike resolution in future studies, reducing interference from surrounding neural activity. This finding highlights the need for a balanced electrode design to optimize impedance for both noise reduction and single-neuron resolution in *in vitro* electrophysiology.

7.2. Future prospects

The developed graphene-based microelectrode array technologies open up several exciting opportunities for future work:

Molybdenum removal post-graphene growth. While the Mo layer initially acts as a catalyst for graphene growth, it is undesirable for the final device due to its lack of optical transparency and biodegradable nature, which degrades over time and affects electrical performance. Although an exploratory study was carried out, further work is needed to establish a method to completely etch Mo after graphene growth. Xenon difluoride (XeF_2) vapor etch could be an area of exploration. XeF_2 is a purely chemical etching process, and since it is very reactive, it does not need a plasma source to react with some materials. XeF_2 has been reported to etch Mo rapidly and selectively [94].

Ensuring reproducible graphene growth. Graphene growth reproducibility is critical for the reliability of graphene-based MEAs, as graphene functions as the core sensing layer of the device. Achieving consistent control over graphene layer characteristics, such as thickness and number of layers, directly impacts key performance factors like optical transparency, impedance, and charge storage capacity. In the present work, the multilayer graphene grown exhibited considerable variation in optical transmittance and electrochemical properties compared to previously reported results, despite utilizing the same CVD reactor, catalyst layer, and growth recipe. These findings highlight the need for a thorough examination of the CVD growth parameters to identify and control variables that may influence graphene layer uniformity. Implementing rigorous monitoring protocols for the CVD reactor conditions as well as careful optimization of process parameters are essential to achieve the desired layer properties reproducibly. Developing a comprehensive understanding of how each parameter affects the graphene's structural and electrochemical properties will be crucial in standardizing the growth process and enhancing device consistency across fabrication batches.

Reducing graphene sheet resistance. The sheet resistance of the graphene tracks is still relatively high, which could limit the scalability and electrode density of the MEA devices. Enhanced conductivity of the graphene layer could be achieved by chemical doping with acic nitric (HNO_3) or engineering the graphene growth process to minimize defects and maximize carrier mobility.

Improving PEDOT:PSS adhesion to graphene. A big concern of using a polymer coating is its adhesion strength to the substrate, which conditions its long-term stability. Oxygen plasma treatment is commonly used for activating the surface and improving the strength of chemical bonds between the substrate and the coating. However, this method is not suited for graphene-based devices as it can cause severe damage to the graphene layer. Alternative surface pretreatment approaches would need to be explored. One promising route could be the investigation UV ozone treatment, which does not affect the structural integrity of graphene.

Further understanding on the graphene/PEDOT:PSS interface. Further investigation is required to understand the interfacial charge-transport mechanisms at the graphene-PEDOT:PSS junction. What happens in terms of the electrons and ions transfer at the interface needs to be studied. This would enable rational design of the grppMEA electrodes to maximize the synergistic effects between the two materials for improved electrochemical performance and neural recording quality. In addition, an equivalent circuit model adapted to the obtained EIS graphs could help to understand the contribution of each material layer.

Long-term stability of MEA devices. Enhancing the long-term stability of MEA devices requires a thorough investigation into the durability of the PEDOT:PSS film on the graphene substrate. Over time, mechanical and chemical degradation of the PEDOT:PSS film can compromise device performance, making it essential to understand its stability when interfaced with graphene. Additionally, the effective-

ness of parylene as a barrier layer for extended use in physiological environments needs to be properly evaluated. Recent studies have shown that combining atomic layer deposited (ALD) Al_2O_3-TiO_2 with CVD parylene in a multilayer coating can significantly improve encapsulation, offering enhanced barrier properties and device longevity. Future work could focus on exploring these multilayer coatings to extend the operational lifespan of MEA devices.

Advancing MEA precision with high-density, single-cell resolution arrays. Scaling MEA arrays to higher densities and reducing electrode sizes are essential steps toward achieving greater spatial resolution and selectivity at the single-cell level. High-density arrays enable finer spatial mapping, allowing neuroscientists to capture more detailed neural activity across complex tissue structures. Reducing electrode dimensions to the size of individual cells enhances selectivity, allowing signals to be isolated from single cells within a densely packed environment. However, miniaturization poses challenges such as increased impedance and potential losses in signal fidelity. Future work could focus on optimizing materials and electrode designs to address these challenges, enabling MEAs with both high spatial density and single-cell selectivity, ultimately advancing the precision of neural recording.

Integrating electrophysiology and optical imaging for enhanced insights into neural dynamics. Combining MEA-based electrophysiology with optical methods like voltage-sensitive dye imaging offers a promising approach for deeper insights into neural network activity. By capturing simultaneous electrical and fluorescence signals, researchers can correlate real-time electrical recordings with spatially resolved optical signals from multiple neurons, allowing for an integrated view of neural dynamics. This correlation between the electrical and fluorescence signals has yet to be explored at the Erasmus MC Neuroscience Department in cerebellar slice studies, where it could extend the understanding of neural connectivity.

References

[1] Sarah Malmquist and Kristina Prescott. *1.8 Cells of the Nervous System*.

[2] Karen Birmingham et al. “Bioelectronic medicines: a research roadmap”. In: *Nature Reviews Drug Discovery 2014 13:6* 13.6 (May 2014), pp. 399–400. ISSN: 1474-1784. DOI: 10.1038/nrd4351. URL: https://www.nature.com/articles/nrd4351.

[3] Vasiliki Giagka and Wouter A. Serdijn. “Realizing flexible bioelectronic medicines for accessing the peripheral nerves – technology considerations”. In: *Bioelectronic Medicine* 4.1 (Dec. 2018), pp. 1–10. ISSN: 23328886. DOI: 10.1186/S42234-018-0010-Y/FIGURES/2. URL: https://bioelecmed.biomedcentral.com/articles/10.1186/s42234-018-0010-y.

[4] Milin Zhang et al. “Electronic neural interfaces”. In: *Nature Electronics 2020 3:4* 3.4 (Apr. 2020), pp. 191–200. ISSN: 2520-1131. DOI: 10.1038/s41928-020-0390-3. URL: https://www.nature.com/articles/s41928-020-0390-3.

[5] Michael Z. Lin and Mark J. Schnitzer. “Genetically encoded indicators of neuronal activity”. In: *Nature Neuroscience 2016 19:9* 19.9 (Aug. 2016), pp. 1142–1153. ISSN: 1546-1726. DOI: 10.1038/nn.4359. URL: https://www.nature.com/articles/nn.4359.

[6] Weijian Yang and Rafael Yuste. “Holographic imaging and photostimulation of neural activity”. In: *Current opinion in neurobiology* 50 (June 2018), pp. 211–221. ISSN: 1873-6882. DOI: 10.1016/J.CONB.2018.03.006. URL: https://pubmed.ncbi.nlm.nih.gov/29660600/.

[7] Aaron B. Wong and J. Gerard G. Borst. “Tonotopic and non-auditory organization of the mouse dorsal inferior colliculus revealed by two-photon imaging”. In: *eLife* 8 (Oct. 2019), pp. 1–50. ISSN: 2050084X. DOI: 10.7554/ELIFE.49091.

[8] Xindong Song et al. “A silent two-photon imaging system for studying in vivo auditory neuronal functions”. In: *Light: Science & Applications 2022 11:1* 11.1 (Apr. 2022), pp. 1–13. ISSN: 2047-7538. DOI: 10.1038/s41377-022-00783-y. URL: https://www.nature.com/articles/s41377-022-00783-y.

[9] Takamitsu Egashira et al. “In vivo two-photon calcium imaging of cortical neurons in neonatal mice”. In: *STAR Protocols* 4.2 (June 2023), p. 102245. ISSN: 2666-1667. DOI: 10.1016/J.XPRO.2023.102245.

[10] Jordan E. Pomeroy et al. “Genetically Encoded Photoactuators and Photosensors for Characterization and Manipulation of Pluripotent Stem Cells”. In: *Theranostics* 7.14 (2017), pp. 3539–3558. ISSN: 1838-7640. DOI: 10.7150/THNO.20593. URL: http://www.thno.org.

[11] Greg C. Carlson and Douglas A. Coulter. “In vitro functional imaging in brain slices using fast voltage-sensitive dye imaging combined with whole-cell patch recording”. In: *Nature Protocols 2008 3:2* 3.2 (Jan. 2008), pp. 249–255. ISSN: 1750-2799. DOI: 10.1038/nprot.2007.539. URL: https://www.nature.com/articles/nprot.2007.539.

[12] Fritjof Helmchen and Winfried Denk. “Deep tissue two-photon microscopy”. In: *Nature Methods 2005 2:12* 2.12 (Nov. 2005), pp. 932–940. ISSN: 1548-7105. DOI: 10.1038/nmeth818. URL: https://www.nature.com/articles/nmeth818.

[13] A. Ustione and D. W. Piston. “A simple introduction to multiphoton microscopy”. In: *Journal of Microscopy* 243.3 (Sept. 2011), pp. 221–226. ISSN: 1365-2818. DOI: 10.1111/J.1365-2818.2011.03532.X. URL: https://onlinelibrary.wiley.com/doi/full/10.1111/j.1365-2818.2011.03532.x%20https://onlinelibrary.wiley.com/doi/abs/10.1111/j.1365-2818.2011.03532.x%20https://onlinelibrary.wiley.com/doi/10.1111/j.1365-2818.2011.03532.x.

[14] Ritchie Chen, Andres Canales, and Polina Anikeeva. “Neural recording and modulation technologies”. In: *Nature Reviews Materials 2017 2:2* 2.2 (Jan. 2017), pp. 1–16. ISSN: 2058-8437. DOI: 10.1038/natrevmats.2016.93. URL: https://www.nature.com/articles/natrevmats201693.

[15] Yichen Lu, Xin Liu, and Duygu Kuzum. “Graphene-based neurotechnologies for advanced neural interfaces”. In: *Current Opinion in Biomedical Engineering* 6 (June 2018), pp. 138–147. ISSN: 2468-4511. DOI: 10.1016/J.COBME.2018.06.001.

[16] Aleksandra Badura et al. “Fast calcium sensor proteins for monitoring neural activity”. In: *Neurophotonics* 1.2 (Oct. 2014), p. 025008. ISSN: 2329-423X. DOI: 10.1117/1.NPH.1.2.025008. URL: https://pubmed.ncbi.nlm.nih.gov/25558464/.

[17] Christoph Stosiek et al. “In vivo two-photon calcium imaging of neuronal networks”. In: *Proceedings of the National Academy of Sciences of the United States of America* 100.12 (June 2003), pp. 7319–7324. ISSN: 0027-8424. DOI: 10.1073/PNAS.1232232100. URL: https://pubmed.ncbi.nlm.nih.gov/12777621/.

[18] Nasim Bakhshaee Babaroud et al. “Multilayer CVD graphene electrodes using a transfer-free process for the next generation of optically transparent and MRI-compatible neural interfaces”. In: *Microsystems & Nanoengineering 2022 8:1* 8.1 (Sept. 2022), pp. 1–14. ISSN: 2055-7434. DOI: 10.1038/s41378-022-00430-x. URL: https://www.nature.com/articles/s41378-022-00430-x.

[19] Young Uk Cho et al. “Transparent neural implantable devices: a comprehensive review of challenges and progress”. In: *npj Flexible Electronics 2022 6:1* 6.1 (June 2022), pp. 1–18. ISSN: 2397-4621. DOI: 10.1038/s41528-022-00178-4. URL: https://www.nature.com/articles/s41528-022-00178-4.

[20] Gonzalo León González. *Transfer-free Fabrication and Assessment of Transparent Multilayer CVD Graphene MEAs for in-vitro Optogenetic Studies*. 2024. URL: https://repository.tudelft.nl/islandora/object/uuid%3A109888a8-05de-4bb6-afd2-f5e7048a3ed9.

[21] Michael Mierzejewski et al. “The noise and impedance of microelectrodes”. In: *Journal of Neural Engineering* 17.5 (Oct. 2020), p. 052001. ISSN: 1741-2552. DOI: 10.1088/1741-2552/ABB3B4. URL: https://iopscience.iop.org/article/10.1088/1741-2552/abb3b4%20https://iopscience.iop.org/article/10.1088/1741-2552/abb3b4/meta.

[22] Michael R Neuman. *Biopotential electrodes*. 2010, pp. 189–240.

[23] Christian Boehler et al. “Tutorial: guidelines for standardized performance tests for electrodes intended for neural interfaces and bioelectronics”. In: *Nature Protocols 2020 15:11* 15.11 (Oct. 2020), pp. 3557–3578. ISSN: 1750-2799. DOI: 10.1038/s41596-020-0389-2. URL: https://www.nature.com/articles/s41596-020-0389-2.

[24] Stuart F. Cogan. “Neural stimulation and recording electrodes”. In: *Annual review of biomedical engineering* 10 (2008), pp. 275–309. ISSN: 1523-9829. DOI: 10.1146/ANNUREV.BIOENG.10.061807.160518. URL: https://pubmed.ncbi.nlm.nih.gov/18429704/.

[25] Vasiliki Giagka. “Flexible Active Electrode Arrays For Epidural Spinal Cord Stimulation”. In: *Doctoral thesis, UCL (University College London)*. (Jan. 2015).

[26] Magnus Berggren and George G. Malliaras. “How conducting polymer electrodes operate”. In: *Science* 364.6437 (Apr. 2019), pp. 233–234. ISSN: 10959203. DOI: 10.1126/SCIENCE.AAW9295/ASSET/F4FD44B7-10D3-4CE8-B62F-9CC5B06FBEFE/ASSETS/GRAPHIC/364{_}233{_}F1.JPEG. URL: https://www.science.org/doi/10.1126/science.aaw9295.

[27] Hengxing Ji et al. “Capacitance of carbon-based electrical double-layer capacitors”. In: *Nature Communications 2014 5:1* 5.1 (Feb. 2014), pp. 1–7. ISSN: 2041-1723. DOI: 10.1038/ncomms4317. URL: https://www.nature.com/articles/ncomms4317.

[28] K. S. Novoselov et al. “A roadmap for graphene”. In: *Nature 2012 490:7419* 490.7419 (Oct. 2012), pp. 192–200. ISSN: 1476-4687. DOI: 10.1038/nature11458. URL: https://www.nature.com/articles/nature11458.

[29] Mohammad Karbalaei Akbari et al. “Functional Two-Dimensional Materials for Bioelectronic Neural Interfacing”. In: *Journal of Functional Biomaterials* 14.1 (Jan. 2023). ISSN: 20794983. DOI: 10.3390/JFB14010035.

[30] Weichen Wei and Xuejiao Wang. “Graphene-Based Electrode Materials for Neural Activity Detection”. In: *Materials (Basel, Switzerland)* 14.20 (Oct. 2021). ISSN: 1996-1944. DOI: 10.3390/MA14206170. URL: https://pubmed.ncbi.nlm.nih.gov/34683762/.

[31] Zhongfan Liu et al. “CVD Synthesis of Graphene”. In: *Thermal Transport in Carbon-Based Nanomaterials* (Jan. 2017), pp. 19–56. DOI: 10.1016/B978-0-32-346240-2.00002-9.

[32] Mingyu Sang et al. “Electronic and Thermal Properties of Graphene and Recent Advances in Graphene Based Electronics Applications”. In: *Nanomaterials 2019, Vol. 9, Page 374* 9.3 (Mar. 2019), p. 374. ISSN: 2079-4991. DOI: 10.3390/NANO9030374. URL: https://www.mdpi.com/2079-4991/9/3/374/htm%20https://www.mdpi.com/2079-4991/9/3/374.

[33] Diep Nguyen et al. “Novel Graphene Electrode for Retinal Implants: An in vivo Biocompatibility Study”. In: *Frontiers in Neuroscience* 15 (Mar. 2021). ISSN: 1662453X. DOI: 10.3389/FNINS.2021.615256/FULL. URL: /pmc/articles/PMC7969870/%20/pmc/articles/PMC7969870/?report=abstract%20https://www.ncbi.nlm.nih.gov/pmc/articles/PMC7969870/.

[34] Dong Wook Park et al. “Graphene-based carbon-layered electrode array technology for neural imaging and optogenetic applications”. In: *Nature Communications 2014 5:1* 5.1 (Oct. 2014), pp. 1–11. ISSN: 2041-1723. DOI: 10.1038/ncomms6258. URL: https://www.nature.com/articles/ncomms6258.

[35] Dong Wook Park et al. “Fabrication and utility of a transparent graphene neural electrode array for electrophysiology, in vivo imaging, and optogenetics”. In: *Nature Protocols 2016 11:11* 11.11 (Oct. 2016), pp. 2201–2222. ISSN: 1750-2799. DOI: 10.1038/nprot.2016.127. URL: https://www.nature.com/articles/nprot.2016.127.

[36] Dong Wook Park et al. “Electrical Neural Stimulation and Simultaneous in Vivo Monitoring with Transparent Graphene Electrode Arrays Implanted in GCaMP6f Mice”. In: *ACS Nano* 12.1 (Jan. 2018), pp. 148–157. ISSN: 1936086X. DOI: 10.1021/ACSNANO.7B04321/SUPPL{_}FILE/NN7B04321{_}SI{_}003.AVI. URL: https://pubs.acs.org/doi/abs/10.1021/acsnano.7b04321.

[37] Robert V. Shannon. “A Model of Safe Levels for Electrical Stimulation”. In: *IEEE Transactions on Biomedical Engineering* 39.4 (1992), pp. 424–426. ISSN: 15582531. DOI: 10.1109/10.126616.

[38] Duygu Kuzum et al. “Transparent and flexible low noise graphene electrodes for simultaneous electrophysiology and neuroimaging”. In: *Nature Communications 2014 5:1* 5.1 (Oct. 2014), pp. 1–10. ISSN: 2041-1723. DOI: 10.1038/ncomms6259. URL: https://www.nature.com/articles/ncomms6259.

[39] Yichen Lu et al. “Ultralow Impedance Graphene Microelectrodes with High Optical Transparency for Simultaneous Deep Two-Photon Imaging in Transgenic Mice”. In: *Advanced Functional Materials* 28.31 (Aug. 2018), p. 1800002. ISSN: 1616-3028. DOI: 10.1002/ADFM.201800002. URL: https://onlinelibrary.wiley.com/doi/full/10.1002/adfm.201800002%20https://onlinelibrary.wiley.com/doi/abs/10.1002/adfm.201800002%20https://onlinelibrary.wiley.com/doi/10.1002/adfm.201800002.

[40] Mehrdad Ramezani et al. “High-density transparent graphene arrays for predicting cellular calcium activity at depth from surface potential recordings”. In: *Nature Nanotechnology 2024 19:4* 19.4 (Jan. 2024), pp. 504–513. ISSN: 1748-3395. DOI: 10.1038/s41565-023-01576-z. URL: https://www.nature.com/articles/s41565-023-01576-z.

[41] Clement Hébert et al. “Flexible Graphene Solution-Gated Field-Effect Transistors: Efficient Transducers for Micro-Electrocorticography”. In: *Advanced Functional Materials* 28.12 (Mar. 2018), p. 1703976. ISSN: 1616-3028. DOI: 10.1002/ADFM.201703976. URL: https://onlinelibrary.wiley.com/doi/full/10.1002/adfm.201703976%20https://onlinelibrary.wiley.com/doi/abs/10.1002/adfm.201703976%20https://onlinelibrary.wiley.com/doi/10.1002/adfm.201703976.

[42] Sergi Brosel-Oliu et al. “Single-Step Functionalization Strategy of Graphene Microtransistor Array with Chemically Modified Aptamers for Biosensing Applications”. In: *Small* (2023), p. 2308857. ISSN: 1613-6829. DOI: 10.1002/SMLL.202308857. URL: https://onlinelibrary.wiley.com/doi/full/10.1002/smll.202308857%20https://onlinelibrary.wiley.com/doi/abs/10.1002/smll.202308857%20https://onlinelibrary.wiley.com/doi/10.1002/smll.202308857.

[43] Damià Viana et al. “Nanoporous graphene-based thin-film microelectrodes for in vivo high-resolution neural recording and stimulation”. In: *Nature Nanotechnology 2024 19:4* 19.4 (Jan. 2024), pp. 514–523. ISSN: 1748-3395. DOI: 10.1038/s41565-023-01570-5. URL: https://www.nature.com/articles/s41565-023-01570-5.

[44] Fikret Taygun Duvan et al. “Graphene-based microelectrodes with bidirectional functionality for next-generation retinal electronic interfaces”. In: *Nanoscale Horizons* (2024). ISSN: 2055-6764. DOI: 10.1039/D4NH00282B. URL: https://pubs.rsc.org/en/content/articlehtml/2024/nh/d4nh00282b%20https://pubs.rsc.org/en/content/articlelanding/2024/nh/d4nh00282b.

[45] Nicolette Driscoll et al. “Multimodal in vivo recording using transparent graphene microelectrodes illuminates spatiotemporal seizure dynamics at the microscale”. In: *Communications Biology 2021 4:1* 4.1 (Jan. 2021), pp. 1–14. ISSN: 2399-3642. DOI: 10.1038/s42003-021-01670-9. URL: https://www.nature.com/articles/s42003-021-01670-9.

[46] Berit Körbitzer et al. “Electrochemical Characterization of Graphene Microelectrodes for Biological Applications”. In: *ChemNanoMat* 5.4 (Apr. 2019), pp. 427–435. ISSN: 2199-692X. DOI: 10.1002/CNMA.201800652. URL: https://onlinelibrary.wiley.com/doi/full/10.1002/cnma.201800652%20https://onlinelibrary.wiley.com/doi/abs/10.1002/cnma.201800652%20https://onlinelibrary.wiley.com/doi/10.1002/cnma.201800652.

[47] Pranoti Kshirsagar et al. “Transparent Graphene/PEDOT:PSS Microelectrodes for Electro- and Optophysiology”. In: *Advanced Materials Technologies* 4.1 (Jan. 2019), p. 1800318. ISSN: 2365-709X. DOI: 10.1002/ADMT.201800318. URL: https://onlinelibrary.wiley.com/doi/full/10.1002/admt.201800318%20https://onlinelibrary.wiley.com/doi/abs/10.1002/admt.201800318%20https://onlinelibrary.wiley.com/doi/10.1002/admt.201800318.

[48] Nasim Bakhshaee Babaroud et al. “Surface modification of multilayer graphene neural electrodes by local printing of platinum nanoparticles using spark ablation†”. In: *bioRxiv* (Aug. 2023), p. 2023.07.30.551155. DOI: 10.1101/2023.07.30.551155. URL: https://www.biorxiv.org/content/10.1101/2023.07.30.551155v1%20https://www.biorxiv.org/content/10.1101/2023.07.30.551155v1.abstract.

[49] Filiberto Ricciardella et al. “Wafer-scale transfer-free process of multi-layered graphene grown by chemical vapor deposition”. In: *Materials Research Express* 7.3 (Mar. 2020), p. 035001. ISSN: 2053-1591. DOI: 10.1088/2053-1591/AB771E. URL: https://iopscience.iop.org/article/10.1088/2053-1591/ab771e%20https://iopscience.iop.org/article/10.1088/2053-1591/ab771e/meta.

[50] Allison Hess-Dunning and Christian A. Zorman. “Electrical interfaces for recording, stimulation, and sensing”. In: *Implantable Biomedical Microsystems: Design Principles and Applications* (Jan. 2015), pp. 13–38. DOI: 10.1016/B978-0-323-26208-8.00002-9.

[51] Amal Kasry et al. “Chemical doping of large-area stacked graphene films for use as transparent, conducting electrodes”. In: *ACS Nano* 4.7 (July 2010), pp. 3839–3844. ISSN: 19360851. DOI: 10.1021/NN100508G/SUPPL{_}FILE/NN100508G{_}SI{_}001.PDF. URL: https://pubs.acs.org/doi/full/10.1021/nn100508g.

[52] Hongtao Liu, Yunqi Liu, and Daoben Zhu. “Chemical doping of graphene”. In: *Journal of Materials Chemistry* 21.10 (Feb. 2011), pp. 3335–3345. ISSN: 1364-5501. DOI: 10.1039/C0JM02922J. URL: https://pubs.rsc.org/en/content/articlehtml/2011/jm/c0jm02922j%20https://pubs.rsc.org/en/content/articlelanding/2011/jm/c0jm02922j.

[53] Zixuan Lu et al. “Organic microelectrode arrays for bioelectronic applications”. In: *Materials Science and Engineering: R: Reports* 153 (May 2023), p. 100726. ISSN: 0927-796X. DOI: 10.1016/J.MSER.2023.100726.

[54] Hui Shi et al. “Effective Approaches to Improve the Electrical Conductivity of PEDOT:PSS: A Review”. In: *Advanced Electronic Materials* 1.4 (Apr. 2015), p. 1500017. ISSN: 2199-160X. DOI: 10.1002/AELM.201500017. URL: https://onlinelibrary.wiley.com/doi/full/10.1002/aelm.201500017%20https://onlinelibrary.wiley.com/doi/abs/10.1002/aelm.201500017%20https://onlinelibrary.wiley.com/doi/10.1002/aelm.201500017.

[55] Daniele Mantione et al. “Poly(3,4-ethylenedioxythiophene) (PEDOT) Derivatives: Innovative Conductive Polymers for Bioelectronics”. In: *Polymers 2017, Vol. 9, Page 354* 9.8 (Aug. 2017), p. 354. ISSN: 2073-4360. DOI: 10.3390/POLYM9080354. URL: https://www.mdpi.com/2073-4360/9/8/354/htm%20https://www.mdpi.com/2073-4360/9/8/354.

[56] Michele Sessolo et al. “Easy-to-Fabricate Conducting Polymer Microelectrode Arrays”. In: *Advanced Materials* 25.15 (Apr. 2013), pp. 2135–2139. ISSN: 1521-4095. DOI: 10.1002/ADMA.201204322. URL: https://onlinelibrary.wiley.com/doi/full/10.1002/adma.201204322%20https://onlinelibrary.wiley.com/doi/abs/10.1002/adma.201204322%20https://onlinelibrary.wiley.com/doi/10.1002/adma.201204322.

[57] Ben J. Woodington et al. “Flexible circumferential bioelectronics to enable 360-degree recording and stimulation of the spinal cord”. In: *Science Advances* 10.19 (May 2024), p. 1230. ISSN: 23752548. DOI: 10.1126/SCIADV.ADL1230/SUPPL{_}FILE/SCIADV.ADL1230{_}SM.PDF. URL: https://www.science.org/doi/10.1126/sciadv.adl1230.

[58] Christina Hassler, Tim Boretius, and Thomas Stieglitz. “Polymers for neural implants”. In: *Journal of Polymer Science Part B: Polymer Physics* 49.1 (Jan. 2011), pp. 18–33. ISSN: 1099-0488. DOI: 10.1002/POLB.22169. URL: https://onlinelibrary.wiley.com/doi/full/10.1002/polb.22169%20https://onlinelibrary.wiley.com/doi/abs/10.1002/polb.22169%20https://onlinelibrary.wiley.com/doi/10.1002/polb.22169.

[59] Christine P. Tan and Harold G. Craighead. “Surface Engineering and Patterning Using Parylene for Biological Applications”. In: *Materials* 3.3 (2010), p. 1803. ISSN: 19961944. DOI: 10.3390/MA3031803. URL: /pmc/articles/PMC5445890/%20/pmc/articles/PMC5445890/?report=abstract%20https://www.ncbi.nlm.nih.gov/pmc/articles/PMC5445890/.

[60] Poppy Oldroyd and George G. Malliaras. “Achieving long-term stability of thin-film electrodes for neurostimulation”. In: *Acta Biomaterialia* 139 (Feb. 2022), pp. 65–81. ISSN: 1742-7061. DOI: 10.1016/J.ACTBIO.2021.05.004.

[61] Juan Ordonez et al. “Thin films and microelectrode arrays for neuroprosthetics”. In: *MRS Bulletin* 37.6 (June 2012), pp. 590–598. ISSN: 08837694. DOI: 10.1557/MRS.2012.117/FIGURES/5. URL: https://link.springer.com/article/10.1557/mrs.2012.117.

[62] Maria Vomero et al. “Conformable polyimide-based μECoGs: Bringing the electrodes closer to the signal source”. In: *Biomaterials* 255 (Oct. 2020), p. 120178. ISSN: 0142-9612. DOI: 10.1016/J.BIOMATERIALS.2020.120178.

[63] Andreas Schander et al. “Towards long-term stable polyimide-based flexible electrical insulation for chronically implanted neural electrodes”. In: *Micromachines* 12.11 (Nov. 2021), p. 1279. ISSN: 2072666X. DOI: 10.3390/MI12111279/S1. URL: https://www.mdpi.com/2072-666X/12/11/1279/htm%20https://www.mdpi.com/2072-666X/12/11/1279.

[64] Sander van den Driesche et al. “A Simple Method to Allow Parylene-C Coatings on Gold Substrates”. In: *Proceedings 2017, Vol. 1, Page 299* 1.4 (Aug. 2017), p. 299. ISSN: 2504-3900. DOI: 10.3390/PROCEEDINGS1040299. URL: https://www.mdpi.com/2504-3900/1/4/299/htm%20https://www.mdpi.com/2504-3900/1/4/299.

[65] Kyungjin Kim et al. “Extended Barrier Lifetime of Partially Cracked Organic/Inorganic Multilayers for Compliant Implantable Electronics”. In: *Small* 17.40 (Oct. 2021), p. 2103039. ISSN: 1613-6829. DOI: 10.1002/SMLL.202103039. URL: https://onlinelibrary.wiley.com/doi/full/10.1002/smll.202103039%20https://onlinelibrary.wiley.com/doi/abs/10.1002/smll.202103039%20https://onlinelibrary.wiley.com/doi/10.1002/smll.202103039.

[66] Maurizio Gulino et al. “Tissue response to neural implants: The use of model systems toward new design solutions of implantable microelectrodes”. In: *Frontiers in Neuroscience* 13.JUL (July 2019), p. 454701. ISSN: 1662453X. DOI: 10.3389/FNINS.2019.00689/BIBTEX. URL: www.frontiersin.org.

[67] Amel Bendali et al. “Purified Neurons can Survive on Peptide-Free Graphene Layers”. In: *Advanced Healthcare Materials* 2.7 (July 2013), pp. 929–933. ISSN: 2192-2659. DOI: 10.1002/ADHM.201200347. URL: https://onlinelibrary.wiley.com/doi/full/10.1002/adhm.201200347%20https://onlinelibrary.wiley.com/doi/abs/10.1002/adhm.201200347%20https://onlinelibrary.wiley.com/doi/10.1002/adhm.201200347.

[68] Deshdeepak Sahni et al. “Biocompatibility of pristine graphene for neuronal interface: Laboratory investigation”. In: *Journal of Neurosurgery: Pediatrics* 11.5 (May 2013), pp. 575–583. ISSN: 1933-0715. DOI: 10.3171/2013.1.PEDS12374. URL: https://thejns.org/pediatrics/view/journals/j-neurosurg-pediatr/11/5/article-p575.xml.

[69] Sung Young Park et al. “Enhanced Differentiation of Human Neural Stem Cells into Neurons on Graphene”. In: *Advanced Materials* 23.36 (Sept. 2011), H263–H267. ISSN: 1521-4095. DOI: 10.1002/ADMA.201101503. URL: https://onlinelibrary.wiley.com/doi/full/10.1002/adma.201101503%20https://onlinelibrary.wiley.com/doi/abs/10.1002/adma.201101503%20https://onlinelibrary.wiley.com/doi/10.1002/adma.201101503.

[70] Alessandra Fabbro et al. “Graphene-Based interfaces do not alter target nerve cells”. In: *ACS Nano* 10.1 (Jan. 2016), pp. 615–623. ISSN: 1936086X. DOI: 10.1021/ACSNANO.5B05647/SUPPL{_}FILE/NN5B05647{_}SI{_}001.PDF. URL: https://pubs.acs.org/doi/abs/10.1021/acsnano.5b05647.

[71] Adam H. Marblestone et al. “Physical principles for scalable neural recording”. In: *Frontiers in Computational Neuroscience* 7.OCT (Oct. 2013), p. 61935. ISSN: 16625188. DOI: 10.3389/FNCOM.2013.00137/BIBTEX.

[72] Ralf Bürgers et al. “Cytotoxicity of 3D-printed, milled, and conventional oral splint resins to L929 cells and human gingival fibroblasts”. In: *Clinical and Experimental Dental Research* 8.3 (June 2022), pp. 650–657. ISSN: 2057-4347. DOI: 10.1002/CRE2.592. URL: https://onlinelibrary.wiley.com/doi/full/10.1002/cre2.592%20https://onlinelibrary.wiley.com/doi/abs/10.1002/cre2.592%20https://onlinelibrary.wiley.com/doi/10.1002/cre2.592.

[73] S. Vollebregt et al. “Influence of the growth temperature on the first and second-order Raman band ratios and widths of carbon nanotubes and fibers”. In: *Carbon* 50.10 (Aug. 2012), pp. 3542–3554. ISSN: 0008-6223. DOI: 10.1016/J.CARBON.2012.03.026.

[74] Andrea C. Ferrari and Denis M. Basko. “Raman spectroscopy as a versatile tool for studying the properties of graphene”. In: *Nature Nanotechnology 2013 8:4* 8.4 (Apr. 2013), pp. 235–246. ISSN: 1748-3395. DOI: 10.1038/nnano.2013.46. URL: https://www.nature.com/articles/nnano.2013.46.

[75] Daniel R. Lenski and Michael S. Fuhrer. “Raman and optical characterization of multilayer turbostratic graphene grown via chemical vapor deposition”. In: *Journal of Applied Physics* 110.1 (July 2011). ISSN: 00218979. DOI: 10.1063/1.3605545/989327. URL: /aip/jap/article/110/1/013720/989327/Raman-and-optical-characterization-of-multilayer.

[76] Achilleas Savva, Shofarul Wustoni, and Sahika Inal. “Ionic-to-electronic coupling efficiency in PEDOT:PSS films operated in aqueous electrolytes”. In: *Journal of Materials Chemistry C* 6.44 (Nov. 2018), pp. 12023–12030. ISSN: 20507526. DOI: 10.1039/C8TC02195C. URL: https://pubs.rsc.org/en/content/articlehtml/2018/tc/c8tc02195c%20https://pubs.rsc.org/en/content/articlelanding/2018/tc/c8tc02195c.

[77] William W. Chiu et al. “Studies of dopant effects in poly(3,4-ethylenedi-oxythiophene) using Raman spectroscopy”. In: *Journal of Raman Spectroscopy* 37.12 (Dec. 2006), pp. 1354–1361. ISSN: 1097-4555. DOI: 10.1002/JRS.1545. URL: https://onlinelibrary.wiley.com/doi/full/10.1002/jrs.1545%20https://onlinelibrary.wiley.com/doi/abs/10.1002/jrs.1545%20https://analyticalsciencejournals.onlinelibrary.wiley.com/doi/10.1002/jrs.1545.

[78] Mira Naftaly et al. “Sheet Resistance Measurements of Conductive Thin Films: A Comparison of Techniques”. In: *Electronics 2021, Vol. 10, Page 960* 10.8 (Apr. 2021), p. 960. ISSN: 2079-9292. DOI: 10.3390/ELECTRONICS10080960. URL: https://www.mdpi.com/2079-9292/10/8/960/htm%20https://www.mdpi.com/2079-9292/10/8/960.

[79] Joost Romijn et al. “A Wafer-Scale Process for the Monolithic Integration of CVD Graphene and CMOS Logic for Smart MEMS/NEMS Sensors”. In: *Proceedings of the IEEE International Conference on Micro Electro Mechanical Systems (MEMS)* 2019-January (Jan. 2019), pp. 260–263. ISSN: 10846999. DOI: 10.1109/MEMSYS.2019.8870741.

[80] Kin Fai Mak et al. “Measurement of the opptical conductivity of graphene”. In: *Physical Review Letters* 101.19 (Nov. 2008), p. 196405. ISSN: 00319007. DOI: 10.1103/PHYSREVLETT.101.196405/FIGURES/4/MEDIUM. URL: https://journals.aps.org/prl/abstract/10.1103/PhysRevLett.101.196405.

[81] Irene Franzetti et al. “Parasitic Effects in Impedance Spectrum of PEM Water Electrolysis Cells: Case Study of High-Frequency Inductive Effects”. In: *Energy Technology* 11.12 (Dec. 2023), p. 2300375. ISSN: 2194-4296. DOI: 10.1002/ENTE.202300375. URL: https://onlinelibrary.wiley.com/doi/full/10.1002/ente.202300375%20https://onlinelibrary.wiley.com/doi/abs/10.1002/ente.202300375%20https://onlinelibrary.wiley.com/doi/10.1002/ente.202300375.

[82] Collins Erinmwingbovo and Fabio La Mantia. “Estimation and correction of instrument artefacts in dynamic impedance spectra”. In: *Scientific Reports 2021 11:1* 11.1 (Jan. 2021), pp. 1–10. ISSN: 2045-2322. DOI: 10.1038/s41598-020-80468-x. URL: https://www.nature.com/articles/s41598-020-80468-x.

[83] Jonathan Rivnay et al. “High-performance transistors for bioelectronics through tuning of channel thickness”. In: *Science Advances* 1.4 (May 2015). ISSN: 23752548. DOI: 10.1126/SCIADV.1400251/SUPPL{_}FILE/1400251{_}SM.PDF. URL: https://www.science.org/doi/10.1126/sciadv.1400251.

[84] Christopher M. Proctor, Jonathan Rivnay, and George G. Malliaras. “Understanding volumetric capacitance in conducting polymers”. In: *Journal of Polymer Science Part B: Polymer Physics* 54.15 (Aug. 2016), pp. 1433–1436. ISSN: 1099-0488. DOI: 10.1002/POLB.24038. URL: https://onlinelibrary.wiley.com/doi/full/10.1002/polb.24038%20https://onlinelibrary.wiley.com/doi/abs/10.1002/polb.24038%20https://onlinelibrary.wiley.com/doi/10.1002/polb.24038.

[85] Sagnik Middya et al. “Microelectrode Arrays for Simultaneous Electrophysiology and Advanced Optical Microscopy”. In: *Advanced Science* 8.13 (July 2021), p. 2004434. ISSN: 2198-3844. DOI: 10.1002/ADVS.202004434. URL: https://onlinelibrary.wiley.com/doi/full/10.1002/advs.202004434%20https://onlinelibrary.wiley.com/doi/abs/10.1002/advs.202004434%20https://onlinelibrary.wiley.com/doi/10.1002/advs.202004434.

[86] Roger J. Mortimer, Aubrey L. Dyer, and John R. Reynolds. “Electrochromic organic and polymeric materials for display applications”. In: *Displays* 27.1 (Jan. 2006), pp. 2–18. ISSN: 0141-9382. DOI: 10.1016/J.DISPLA.2005.03.003.

[87] Koichi Aoki, Tetsuya Aramoto, and Yoshimasa Hoshino. “Photographic measurements of propagation speeds of the conducting zone in polyaniline films during electrochemical switching”. In: *Journal of Electroanalytical Chemistry* 340.1-2 (Nov. 1992), pp. 127–135. ISSN: 1572-6657. DOI: 10.1016/0022-0728(92)80293-D.

[88] Xuezheng Wang, Benjamin Shapiro, and Elisabeth Smela. “Visualizing Ion Currents in Conjugated Polymers”. In: *Advanced Materials* 16.18 (Sept. 2004), pp. 1605–1609. ISSN: 1521-4095. DOI: 10.1002/ADMA.200400188. URL: https://onlinelibrary.wiley.com/doi/full/10.1002/adma.200400188%20https://onlinelibrary.wiley.com/doi/abs/10.1002/adma.200400188%20https://onlinelibrary.wiley.com/doi/10.1002/adma.200400188.

[89] Eleni Stavrinidou et al. “Direct Measurement of Ion Mobility in a Conducting Polymer”. In: *Advanced Materials* 25.32 (Aug. 2013), pp. 4488–4493. ISSN: 1521-4095. DOI: 10.1002/ADMA.201301240. URL: https://onlinelibrary.wiley.com/doi/full/10.1002/adma.201301240%20https://onlinelibrary.wiley.com/doi/abs/10.1002/adma.201301240%20https://onlinelibrary.wiley.com/doi/10.1002/adma.201301240.

[90] Fernando R. Fernandez, Jordan D.T. Engbers, and Ray W. Turner. “Firing dynamics of cerebellar Purkinje cells”. In: *Journal of Neurophysiology* 98.1 (July 2007), pp. 278–294. ISSN: 00223077. DOI: 10.1152/JN.00306.2007/ASSET/IMAGES/LARGE/Z9K0070782900010.JPEG. URL: https://journals.physiology.org/doi/10.1152/jn.00306.2007.

[91] Luis A. Camuñas-Mesa and Rodrigo Quian Quiroga. “A Detailed and Fast Model of Extracellular Recordings”. In: *Neural Computation* 25.5 (May 2013), pp. 1191–1212. ISSN: 0899-7667. DOI: 10.1162/NECO{_}A{_}00433. URL: https://dx.doi.org/10.1162/NECO_a_00433.

[92] Vijay Viswam et al. “Optimal electrode size for multi-scale extracellular-potential recording from neuronal assemblies”. In: *Frontiers in Neuroscience* 13.APR (Apr. 2019), p. 453606. ISSN: 1662453X. DOI: 10.3389/FNINS.2019.00385/BIBTEX.

[93] Ugo Bruno, Anna Mariano, and Francesca Santoro. “A systems theory approach to describe dynamic coupling at the cell-electrode interface”. In: *APL Materials* 9.1 (Jan. 2021). ISSN: 2166532X. DOI: 10.1063/5.0025293/279679. URL: /aip/apm/article/9/1/011103/279679/A-systems-theory-approach-to-describe-dynamic.

[94] Özgür Çelík. “Surface and thin film studies of the etching of molybdenum by xenon difluoride”. In: (2010). DOI: 10.7282/T3PZ58WT.

[95] Artem A. Osipov et al. “Highly Selective Plasma Etching Technique for Molybdenum”. In: *Plasma Chemistry and Plasma Processing* 43.3 (May 2023), pp. 697–707. ISSN: 15728986. DOI: 10.1007/S11090-023-10318-X/FIGURES/8. URL: https://link.springer.com/article/10.1007/s11090-023-10318-x.

[96] Wei Feng et al. “Two-Dimensional Fluorinated Graphene: Synthesis, Structures, Properties and Applications”. In: *Advanced Science* 3.7 (July 2016), p. 1500413. ISSN: 2198-3844. DOI: 10.1002/ADVS.201500413. URL: https://onlinelibrary.wiley.com/doi/full/10.1002/advs.201500413%20https://onlinelibrary.wiley.com/doi/abs/10.1002/advs.201500413%20https://onlinelibrary.wiley.com/doi/10.1002/advs.201500413.

[97] M. Baraket et al. “The functionalization of graphene using electron-beam generated plasmas”. In: *Applied Physics Letters* 96.23 (June 2010), p. 231501. ISSN: 00036951. DOI: 10.1063/1.3436556/892416. URL: /aip/apl/article/96/23/231501/892416/The-functionalization-of-graphene-using-electron.

[98] Huaichao Yang et al. “Preferential and reversible fluorination of monolayer graphene”. In: *Journal of Physical Chemistry C* 115.34 (Sept. 2011), pp. 16844–16848. ISSN: 19327447. DOI: 10.1021/JP204573Z/ASSET/IMAGES/LARGE/JP-2011-04573Z{_}0002.JPEG. URL: https://pubs.acs.org/doi/full/10.1021/jp204573z.

[99] Rahul R. Nair et al. “Fluorographene: A Two-Dimensional Counterpart of Teflon”. In: *Small* 6.24 (Dec. 2010), pp. 2877–2884. ISSN: 1613-6829. DOI: 10.1002/SMLL.201001555. URL: https://onlinelibrary.wiley.com/doi/full/10.1002/smll.201001555%20https://onlinelibrary.wiley.com/doi/abs/10.1002/smll.201001555%20https://onlinelibrary.wiley.com/doi/10.1002/smll.201001555.

[100] Jaegeon Ryu et al. “Fundamental Understanding of Nanostructured Si Electrodes: Preparation and Characterization”. In: *ChemNanoMat* 4.4 (Apr. 2018), pp. 319–337. ISSN: 2199-692X. DOI: 10.1002/CNMA.201700362. URL: https://onlinelibrary.wiley.com/doi/full/10.1002/cnma.201700362%20https://onlinelibrary.wiley.com/doi/abs/10.1002/cnma.201700362%20https://aces.onlinelibrary.wiley.com/doi/10.1002/cnma.201700362.

A

Chapter 4: Supplementary Information

A.1. Molybdenum removal post-graphene growth

Graphene selectively grows on the molybdenum (Mo) catalyst layer, conforming to the surface topography. Prior to CVD graphene growth, a 50 nm Mo layer is sputtered and patterned to create desired structures. While the Mo layer initially acts as a catalyst for graphene growth, it is undesirable for the final device due to its lack of optical transparency and biodegradable nature, which degrades over time and affects electrical performance. Therefore, a robust method for complete removal of molybdenum post-graphene growth is necessary. In this work, several approaches to remove Mo have been explored:

PLASMA ETCHING

Plasma etching techniques are capable of selectively etching molybdenum, yet they pose a significant challenge in the present of graphene as ion bombardment may induce structural defects in the graphene layer. The energetic ions in the plasma can disrupt the carbon-carbon bonds within the graphene lattice, leading to the formation of vacancies, defects, or damage to the graphene structure. As a result, the pristine properties of the graphene layer may be compromised. Considering this, the approach followed in this work was to create an optimized plasma etching recipe that uses minimal physical energy while allowing ions to diffuse and chemically react with Mo layer.

For this purpose, an oxidized Si test wafer was processed with graphene grown on a patterned Mo layer. AMS110 etcher (Alcatel), a ICP-RIE system, was used. SF_6 gas (650 sccm flow) was used for the plasma-chemical etching of molybdenum. To minimize the physical sputtering of the graphene layer, no bias voltage (no chuck power) was applied to the substrate. The technological process parameters that were studied were: ICP power (ranging from 1000 W to 2800 W) and pressure (0.05 mbar and 0.1 mbar). The etch time was adjusted for each test. Additionally, increasing the temperature to 40 ºC was explored, motivated by the increased etch rate of molybdenum reported in [95]. Raman spectroscopy and SEM-EDX techniques, energy dispersive X-ray spectroscopy, were performed to assess the quality of graphene and the composition of the sample after plasma etching process. Obtained Raman spectrums are shown in Fig. A.1.

Plasma sources with fluorine radicals, such as SF_6, have previously shown to fluorinate graphene [96, 97, 98]. During this plasma fluorination process, the fluorine radicals generated by the plasma absorb onto graphene structure and form C-F bonds. The Raman spectra of fluorinated monolayer graphene is characterized by a high intensity D peak (at 1350 cm^{-1}) and an additional D' peak (at 1620 cm^{-1}), which are related to the level of disorder and defects and are not present in pristine graphene. Recovery of pristine graphene from fluorinated graphene by thermal annealing has been previously shown [97, 98, 99]. Baraket et al. [97] synthetized fluorinated graphene by plasma fluorination and showed that C-F bonds could be reverted to original C-C bonds by removing F atoms via rapid thermal

annealing at 500 °C in Ar (2 Torr) for 10 min. Less literature about fluorinated multilayer graphene was found. Yang et al. [98] demonstrated that there is a preferential fluorination and reversibility towards monolayer graphene while showing a higher resistance to fluorination in bilayer and trilayer graphene. This considering, a thermal annealing test at 300 ºC in Ar and H2 gases for 1h was performed in one of the samples in Aixtron Black Magic Pro tool.

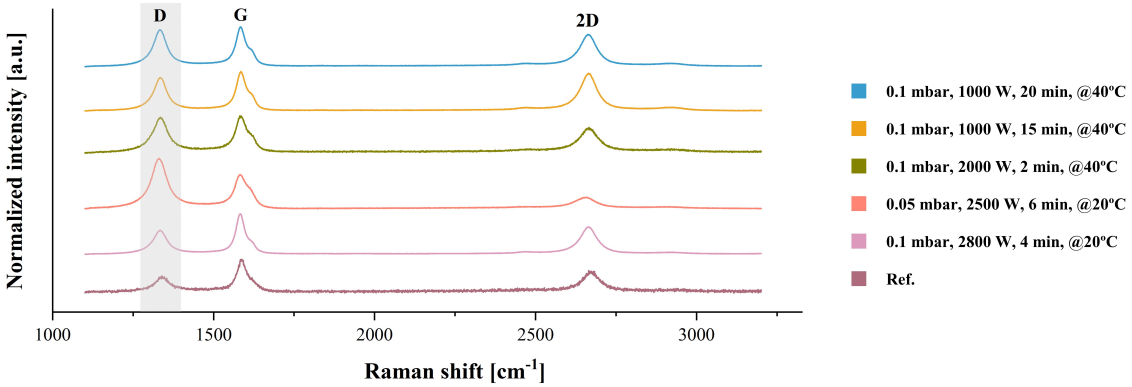

Figure A.1: Raman spectrum of CVD-grown multilayer graphene after various Mo dry etching recipes. The technological process parameters that were studied were: ICP power (ranging from 1000 W to 2800 W) and pressure (0.05 mbar and 0.1 mbar). The etch time was adjusted for each test.

WET ETCHING

Ricciardella et al. [49] presented a method to etch Mo underneath multilayer graphene with hydrogen peroxide (H_2O_2) solution, and they showed that H_2O_2 solution can remove Mo without compromising the quality of graphene. However, graphene tends to delaminate and detach from the substrate as Mo is being etched away. To prevent this, in microfabricated transfer-free graphene electrodes proposed by Babaroud et al. [18], Mo wet etch process was done after the encapsulating polymer is deposited on the frontside of the wafer, thus providing an adherence surface to graphene. After a DRIE process on the backside of the Si wafer and oxide removal, the Mo layer is exposed and wet etched with H_2O_2. This process is tailored specifically for fully realized graphene flexible implants and cannot be adopted for a rigid graphene MEA due to the inability to perform a DRIE process at the backside of the wafer. Therefore, a robust method to completely remove Mo while preventing graphene detachment from the substrate should be found.

The underlying motivation of testing Mo wet etch came from the observation that graphene grown on a patterned Mo layer seemed to form stronger bonds to the substrate at its edges. This is because graphene growth reaction is also mediated by the sidewalls of the Mo-C structures, which can provide additional growth sites. In order to further mitigate the risk of graphene detachment, the wet etch step was tested after the metal (Ti/Al) protective layer and gold tracks deposition. The metal layer patterned in the microelectrodes and the gold tracks partly overlapping with the graphene inner tracks provided additional support for maintaining the graphene layer in place when etching the underneath Mo layer. Prior to incorporating this step into the final quartz wafers, Si test wafers were processed up to the gold tracks deposition and patterning step. At this point, the wafer was covered with 31% H_2O_2 solution forming a puddle. Two different etch times were tested: 5 and 8 mins. The samples were subsequently heated up in a vacuum oven at 200 °C for 1h to remove any remaining moisture and enhance the adhesion of the graphene layer to the substrate. Once the optimal etching process was identified, it was adopted for the final quartz wafers.

An etch time of 8 min resulted in a complete removal of Mo up to the point that the graphene tracks lost the anchor points to the substrate and detached, as observed in Fig. A.2a. This detachment is likely attributed to intercalation of the peroxide solution between the graphene surface and the

substrate, which significantly weakened the van der Waals forces, ultimately causing graphene delamination. When the etching time was reduced to 5 minutes, no delamination of the graphene layer was observed, and the etching of Mo was partially completed. The transparency of the graphene layer allowed the underlying silicon oxide color to show through, as seen in Fig. A.2a. Although some Mo residues were still optically visible, Energy Dispersive X-ray (EDX) mapping conducted on a small area of the graphene tracks did not reveal any Mo peak, as demonstrated in Fig. A.2c. Additionally, Raman spectroscopy performed before and after the Mo etching process, in Fig. A.2b, showed no significant impact on the quality of the graphene layer. In conclusion, an etching time of 5 minutes with a 31% H_2O_2 solution was determined to be an optimal balance for the test silicon wafers, effectively removing most of Mo while preserving the integrity of the graphene layer.

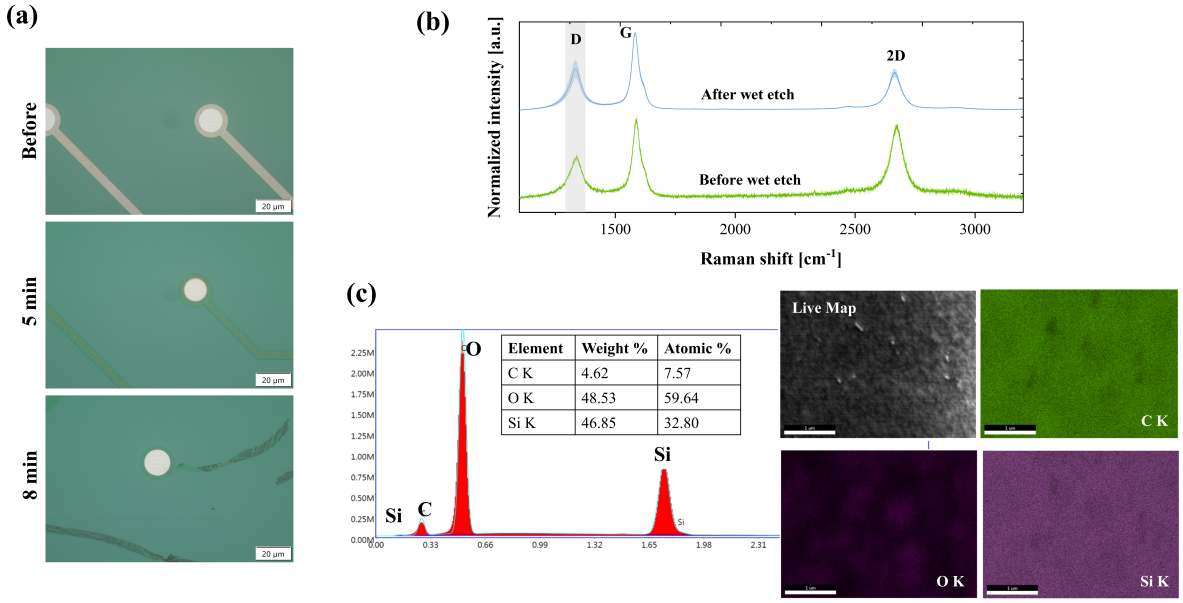

Figure A.2: **(a)** Optical images showing the effect of Mo wet etching process on graphene layer. Graphene microelectrodes are protected by a metal layer. Mo layer underneath graphene is etched with H_2O_2 solution with two different etch times: 5 and 8 mins. **(b)** Raman spectrum of CVD grown multilayer graphene before and after Mo wet etching process. **(c)** EDX mapping (5 keV) of multilayer graphene on oxidized Si wafer after Mo removal.

A.2. PEDOT:PSS coating

A.2.1. PEDOT:PSS thickness curve

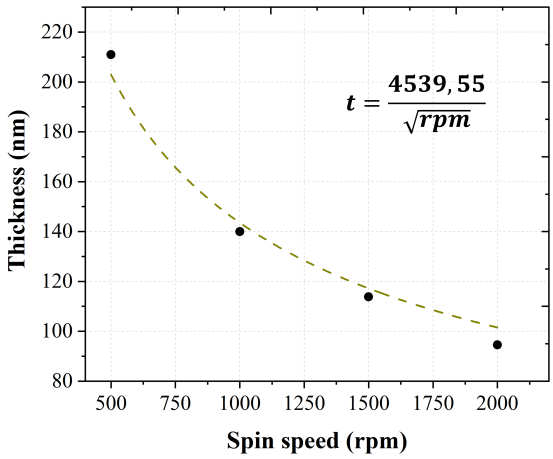

Figure A.3: Calibration curve for the thickness of PEDOT:PSS polymer. The thickness is inversely proportional to the spin coating velocity. A function was fitted to the measured data points, and the resulting equation is shown in the image. This formula enables the calculation of the thickness (in nm) based on a constant parameter and the spin speed (in rpm).

A.2.2. PEDOT:PSS coating on non-patterned graphene

Prior to the integration of PEDOT:PSS on graphene microelectrodes, the electrochemical performance of graphene/PEDOT:PSS composite was studied through some test samples. The samples consisted of a glass substrate with non-patterned CVD grown multilayer graphene layer and coated with PEDOT:PSS. Sample preparation involved depositing a 50 nm non-patterned layer of Mo onto a Si wafer, which served as the catalyst for CVD graphene growth, using Aixtron Black Magic Pro tool. The same graphene growth process intended for the final MEA devices was employed. Following growth, the Si wafer was cleaved into smaller samples for the purpose of transferring a small graphene layer area to a 2x2 cm glass sample. The piece of wafer was covered with 31% hydrogen peroxide (H_2O_2) forming a puddle. After 8 min, the piece of wafer was gently immersed in a DI water filled beaker allowing the graphene layer to slowly detach from the substrate and float on the liquid surface. The floating graphene was then scooped on the glass slide. The graphene transfer process is illustrated in Fig. A.4 a.

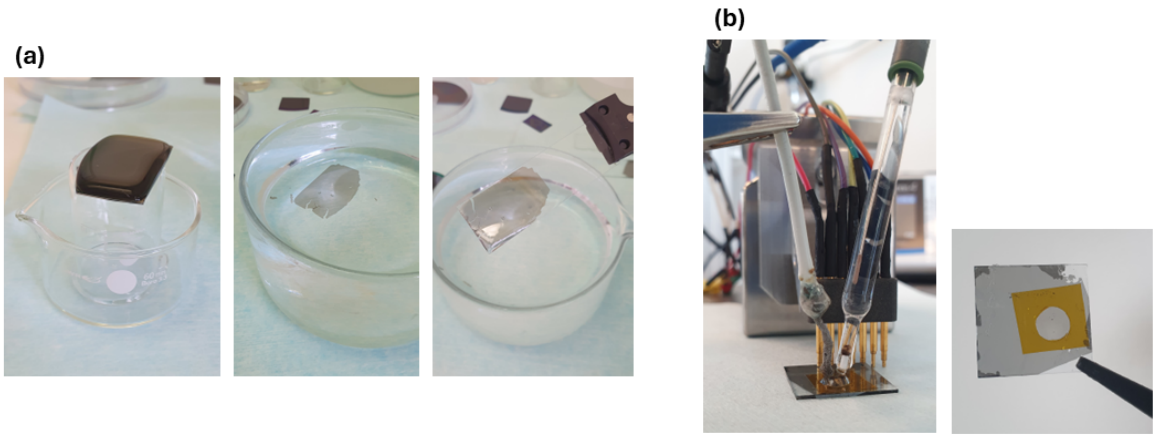

Figure A.4: (a) Graphene transfer process using H_2O_2. **(b)** Three-electrode setup for electrochemical characterization. A Kapton tape with a 0.6 cm diameter hole defined the area of the working electrode.

The conductive polymer solution was prepared by adding 5 vol% ethylene glycol (EG), 0.002 vol% dodecylbenzene sulfonic acid (DBSA) and 1 wt% of 3-Glycidyloxypropyltrimethoxysilane (GOPS) to the PEDOT:PSS solution [76]. EG helps to improve the conductivity, DBSA is a sulfanctant which improves the wettability so that the solution spreads better along the surface. GOPS is the crosslinker and it also enhances the adhesion and stability of PEDOT:PSS films in aqueous environments [56]. For the spin coating procedure, a drop of PEDOT:PSS solution was placed on the area of interest. The samples were spin coated at 1000 and 3000 rpm. A step of annealing at 140ºC for 1h ensured the stability of the coating on the graphene surface.

Electrochemical characterization of the PEDOT:PSS spin coated samples as well as the bare graphene samples was conducted. A three-electrode setup consisting of a Ag/AgCl reference electrode (RE), Pt mesh counter electrode (CE) and the sample of interest as the working electrode (WE) coupled to the Palmsens4 potentiostat was prepared. A Kapton tape with a 0.6 cm diameter hole defined the area of the WE. A droplet of phosphate-buffered saline (PBS) serving as the electrolyte was placed and constraint within that area forming a spherical shape due to the surface tension. The WE was coupled to a gold spring-loaded pin in contact with the material of interest, while the RE and CE were superficially immersed in the PBS droplet. The three-electrode setup is illustrated in Fig. A.4 b. Impedance spectra, EIS, were recorded from 1 Hz to 1 MHz, and averaged from 5 measurements. Using the same setup, cyclic voltammograms, CV, were conducted with an experimentally determined potential limit range from -0.3 V to 0.8 V. A scan rate of 0.1 V/s was used. The obtained EIS and CV curves are depicted in Fig. A.5.

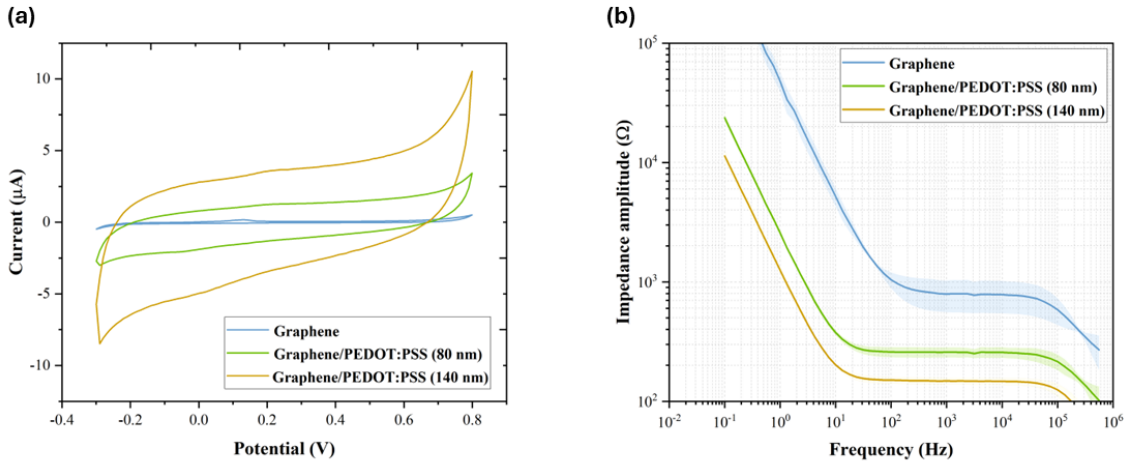

Figure A.5: Cyclic voltammetry (CV) and electrochemical impedance spectroscopy (EIS) measurements of graphene and graphene/PEDOT:PSS test samples. PEDOT:PSS was spin coated at 1000 and 3000 rpm to achieve a thickness of 140 nm and 80 nm, respectively. A Kapton tape with a 0.6 cm diameter hole defined the area of the working electrode. **a.** CV curves for bare graphene and graphene/PEDOT:PSS electrodes. A scan rate of 0.1 V/s was used and a water window of -0.3 V to 0.8 V. **b.** EIS curves for bare graphene and graphene/PEDOT:PSS electrodes.

B

Chapter 5: Supplementary Information

B.1. Electrochemical impedance spectroscopy

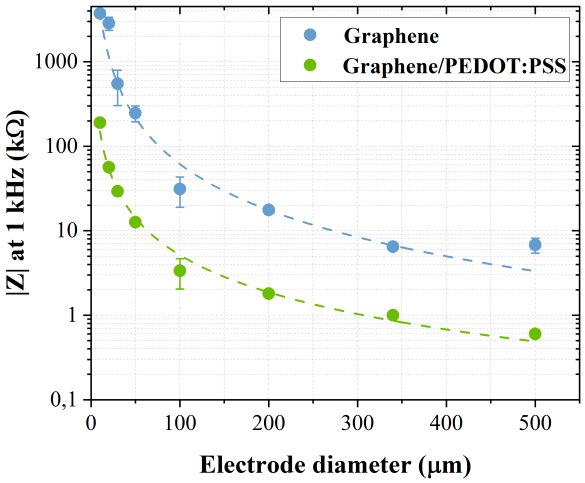

Figure B.1: Impedance dependence on electrode size for graphene and PEDOT:PSS-coated graphene electrodes.

The inverse relationship between impedance and electrode size is illustrated in Fig. B.1. The data points were fitted using the following power function:

$$Z = aD^b$$

where Z denotes the impedance (in $k\Omega$), D is the electrode diameter (in µm) and a and b are fitting parameters.

	Fitting parameters	
	a	b
$Graphene$	261765	-1.81
$Graphene/PEDOT:PSS$	4375	-1.46

Table B.1: Fitted parameters to the impedance-electrode size equation.

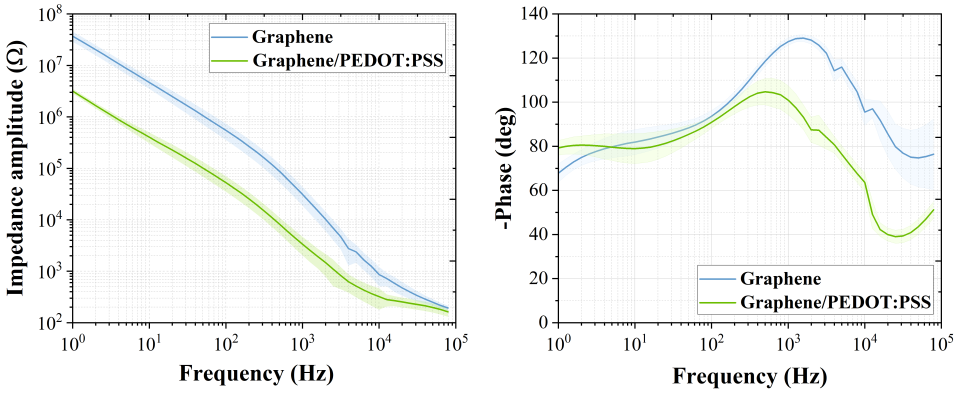

Figure B.2: EIS magnitude and phase of graphene and graphene/PEDOT:PSS electrodes. The measurements correspond to an average of 10 electrodes with a size of 100 µm diameter.

B.2. Cyclic voltammetry

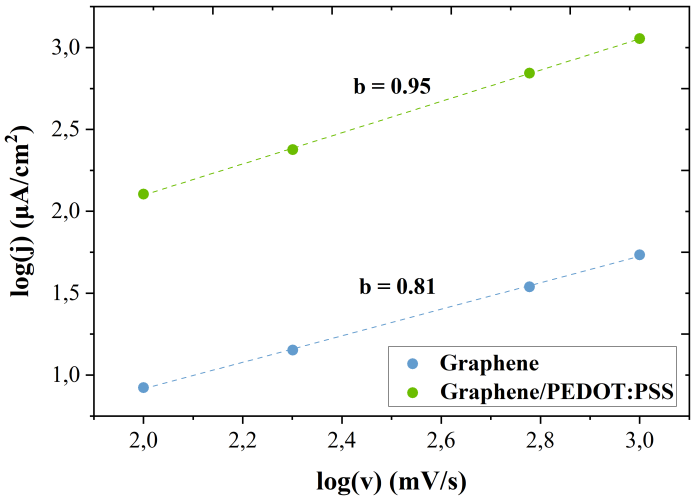

Figure B.3: Current dependence on scan rate. The current density (j), measured at the midpoint of the cyclic voltammetry (CV) voltage range (specifically at -0.2 V), was normalized to the electrode area and analyzed across various scan rates (v). The CV curves obtained from the 50 µm-diameter electrodes were used for this analysis. By presenting these values in logarithmic form, the resulting slope (b-value) provides insight into the capacitive characteristics of the electrode.

The current dependence on scan rate was analyzed through a power law relationship,

$$I_p = av^b \rightleftharpoons \log(I_p) = \log(a) + b \cdot \log(v)$$

where I_p represents the peak current, v the scan rate and a and b are the arbitrary constants. In the CV curves obtained from the 50 µm-diameter electrodes, no distinct peak currents were observed. Instead, a fixed potential point at -0.2 V was selected, where the current values remained consistent. By plotting the current and scan rate in logarithmic form, the resulting slope (b-value) provides valuable insights into the capacitive characteristics of the electrode. A b-value of 1 indicates that capacitive processes dominate the electrochemical kinetics, while a b-value of 0.5 suggests diffusion-limited processes [100]. Values between 0.5 and 1 indicate a mixed mechanism. The $log(j)$ vs $log(v)$ plot in Fig. B.3 demonstrates that the b-value corresponding to graphene and graphene/PEDOT:PSS electrodes are 0.81 and 0.95, respectively. This suggests that the PEDOT:PSS coating enhances the capacitive response compared to bare graphene.

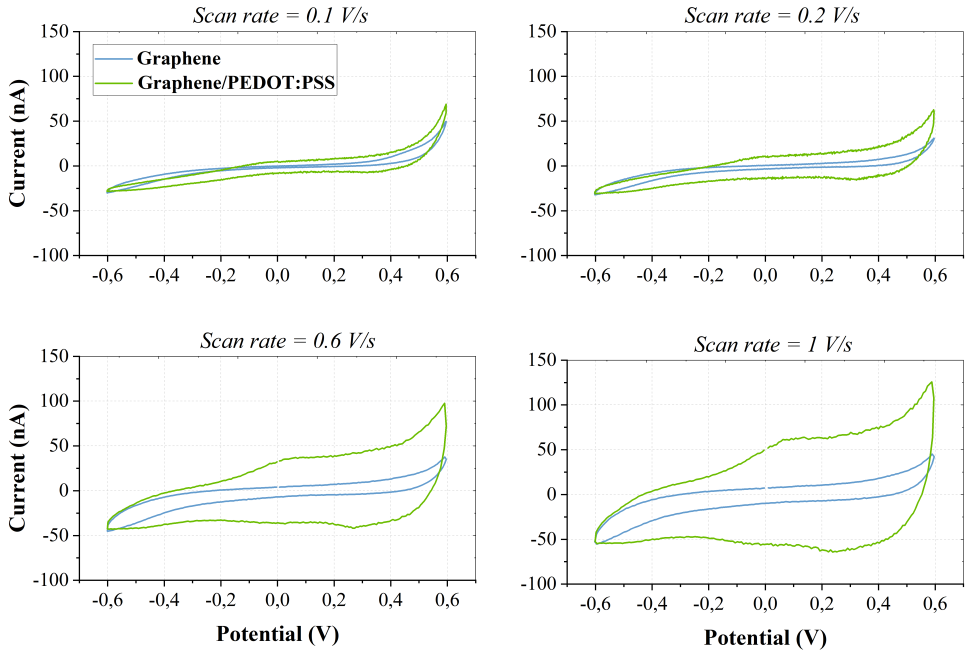

Figure B.4: Cyclic voltammetry (CV) curves of graphene and graphene/PEDOT:PSS electrodes. Electrodes with a diameter of 100 µm were characterized with scan rates of 0.1, 0.2, 0.6 and 1 V/s.

	$CSC\ total\ (\mu C/cm^2)$			
	0.1 V/s	0.2 V/s	0.6 V/s	1 V/s
$Graphene$	3216	1457	734	557
$Graphene/PEDOT:PSS$	5095	3025	2031	1816

Table B.2: Total CSC values for graphene and graphene/PEDOT:PSS electrodes (100 µm diameter in size) obtained at different scan rates.

C

Microfabrication flowchart

PEDOT:PSS-coated graphene microelectrode array on quartz substrate

Flow chart

Nerea Alvarez de Eulate

Run number:
Process engineer: Nerea Alvarez de Eulate
Mentor: Sten Vollebregt
Start: May 2024
Contamination: Yes
Labs: CR100, CR10000, MEMS, Polymer, Biosonics

EKL (Else Kooi Laboratory)
DELFT UNIVERSITY OF TECHNOLOGY

Address	Feldmannweg 17, 2628 CT Delft, The
P.O. Box	5053, 2600 GB Delft, The Netherlands
Phone :	+31 - (0)15 - 2783868
Fax :	+31 - (0)15 - 2622163
Website	http://ekl.tudelft.nl/EKL/Home.php

Detailed information about possible contamination:

Place/Clean Rooms used in the process:

- Write the sequence of used labs from start to finish.
- Which (Non-standard) materials or process steps
- Process step number
- What kind of process or machine was used?
- The other materials or wafers that contain non-green metals that are also processed in this machine

Lab/ Clean Room	Non-standard materials	Process step	Machine-process	Other materials used in machine
CR100	none	none	none	none
CR10000	Yes, graphene	12	BlackMagic	Cu, Pt, Ni
CR10000	Yes, gold	19, 23	CHA	Cu
MEMS	none	none	none	none
Polymer	none	none	none	none
Biosonics	none	none	none	none

If other labs are used:
Write the steps number: Possible contamination issues/materials.
None

If there are custom steps in a standard process or possible cross contamination materials are used: Write down the

- **Step number**
- **Material**
- **Machine/tool where the process is done**
- **Pre and past process step numbers that are used to prevent cross contamination.**

Step number	Material	Machine/Tool/lab	Process steps to prevent cross contamination
13	Cu	Trikon Sigma	Use the cassette for contaminated wafers. Use transport wafers for red metals for each of the test wafers. Use non-contaminated tweezers for the transport wafers and contaminated tweezers for the test wafers.

STARTING MATERIAL

Use **15 double side polished 4" fused silica (SiO2) wafer**, with the following specifications:

Type: NA	
Orientation:	NA
Resistivity:	NA
Thickness:	500 μm
Diameter:	100.0 mm

Wafers taken out of an already opened box must be cleaned before processing, according to the standard procedure.
Wafers taken out of an unopened wafer box do not have to be cleaned before processing**.**

PROCESS DESCRIPTION

The aim of the current process is to develop graphene-based optically transparent microelectrode arrays (MEAs). Graphene is being grown on a patterned Mo catalyst layer. After graphene growth, some metal layers will be deposited and patterned (a protective Ti/Al layer on the electrodes and a Ti/Au layer for the tracks and contact pads). Finally, the MEA will be encapsulated by 1 μm-thick parylene-C polymer and some openings will be created. Precautions related to processing transparent wafers and contaminated wafers are taken.

The process consist of 8 parts:

1) Cleaning step
2) Mo deposition, patterning and graphene growth
3) Ti/Al metal deposition and patterning (protective layer on electrodes)
4) Ti/Au metal deposition and patterning (tracks and contact pads)
5) Parylene C layers (encapsulation + sacrificial) deposition
6) Wafer dicing (Biosonics Lab)
7) PEDOT:PSS spin coating & peel-off
8) Packaging

PART 1: CLEANING STEP

1. CLEANING PROCEDURE: HNO3 99%

Wafers taken out of an unopened wafer box do not have to be cleaned before processing.
Cleaning:
10 minutes in fuming nitric acid (Merck: HNO3 99%) at ambient temperature. Use wet bench "HNO3 (99%)" and the carrier with the white dot.
QDR:
Rinse in the Quick Dump Rinser with the standard program until the resistivity is 5 MΩ.
Use the Semitool "rinser/dryer" with the standard program, and the white carrier with a red dot.

PART 2: MO DEPOSITION, PATTERNING AND GRAPHENE GROWTH

2. WAFER NUMBERING

Use a diamond tip scriber to indent the quartz wafers at the front side at the bottom end.
This helps identify each wafer and prevent miss-positioning of the wafer.

Perform a cleaning step afterwards to remove the particles created with the scriber.
Rinse with the DI water hose and spin dry.

3. CATALYST DEPOSITION

Use the **TRIKON SIGMA** sputter coater for the deposition of the catalyst metal Mo layer on the process wafers.
Follow the operating instructions from the manual when using this machine.

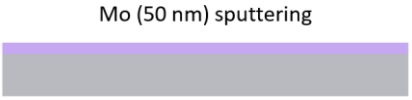

In order to coat transparent wafers, the sensors must be off!
Alternatively use carrier wafers, however this carries issues of the wafer moving above the carrier wafer.

If necessary, perform a target clean with recipe **'_TrgtCln_Mo_50C'**. This step will require the use of a dummy wafer.
Mo: 50 nm, recipe '**Mo_50nm_50C**'

4. BACKSIDE LAYER DEPOSITION

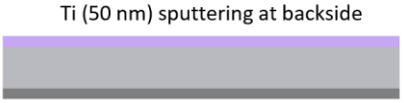

Use the **TRIKON SIGMA** sputter coater for the deposition of a 50nm Ti layer on the backside of the process wafers.
Follow the operating instructions from the manual when using this machine.

In order to coat transparent wafers, the sensors must be off!

If necessary, perform a target clean with recipe **'_Trgt_Cln_Ti_50C'.** This step will require the use of a dummy wafer.
Ti: 50 nm, recipe '**Ti_50nm_50C**'

5. COATING AND BAKING

Use the **EVG 120** wafertrack to coat the wafers with resist, and follow the instructions specified for this equipment.
The process consists of a treatment with HMDS (hexamethyldisilazane) vapor with nitrogen as a carrier gas, spin coating with Shipley SPR3012 positive photoresist, and a soft bake at 95degC for 2 mins 15 seconds.
Always check the temperature of the hotplate and the relative humidity (48 ± 2 %) in the room first.

Use coating recipe **'SpeCo – 3012 – 1.4 µm-glass-noEBR-SB2'15"'**

NOTE: Glass coating recipes have an extended bake times to compensate for the lower thermal conductivity, and prevent the photoresist to adhere to the mask during exposure with the contact aligner. Same counts for the development recipe.

6. ALIGNMENT AND EXPOSURE

Processing will be performed on the **SUSS MicroTec MA/BA8** mask aligner.
Follow the operating instructions from the manual when using this machine.

Use **G-MEA-NALV2024 mask**, **layer GRAPHENE**,
Use recipe: **'1_FSA_Soft_Contact'**
Calculate the exposure time by consulting the mask aligner exposure energy data log.
Assume Mo is opaque, so 140mJ/cm^2 for all wafers (add 15% more time to compensate for not being able to do hard contact).

7. DEVELOPMENT

Use the **EVG 120** wafertrack to develop the wafers and follow the instructions specified for this equipment.
The process consists of a post-exposure bake at 115°C for 2 mins 15 s, followed by a development step using Shipley MF322 developer (single puddle process), and a hard bake at 100°C for 2 mins 15 s.

Use development program '**Dev – SP glass**'

8. INSPECTION: LINEWIDTH

Visually inspect the wafers through a microscope and check the linewidth. No PR residues are allowed.

If resist remains are found attempt rinsing the wafers with a DI water gun and spin drying them. If it persists review your exposure settings as they might be off.
(In case of misalignment or defects in the photoresist pattern remove the photoresist layer with acetone followed by IPA).

9. PLASMA ETCHING OF MOLYBDENUM

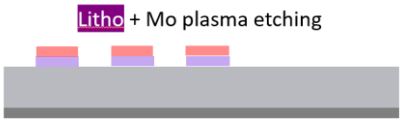

Use the **Trikon Ωmega 201** plasma etcher.
Follow the operating instructions from the manual when using this machine.
The process conditions of the etch program may not be changed!

Use sequence '**Mo_test8**' and set the platen temperature to **40 °C**. Check that the time is set for 50 nm (~30 sec). Increase the temperature in two steps. All in one go might lead to an overshoot in the control system.

NOTE: other Mo etching recipes (e.g., Mo_test5), although less selective to Mo, are also available which uses a combination of Cl_2 and O_2 gas etchants.

10. PHOTORESIST STRIPPING: NI555

In cr10000 fume hoods, fill a glass beaker with NI555. Prepare the ultrasonicator with DI water and set an elevated temperature (40-60ºC). Put the beaker with NI555 inside the ultrasonicator. Place the wafers in a holder and submerge it in the beaker with NI555. Start the ultrasonicator (at 40-60ºC, 80 kHz) and leave it for 30 mins. Rinse it with DI water for ~10 mins.

Carefully inspect the wafer under an optical microscope to check that all the photoresist has been removed. There might be visually hard to detect very thin (nm-thick) photoresist residues left on the Mo pattern.

NOTE: Due to the ion bombardment from the previous step, NI555 might not be effective enough at completely removing the photoresist. An additional short oxygen plasma cycle (using TePla Plasma 300) could be used to get rid of the residues left.

11. TI LAYER ETCHING

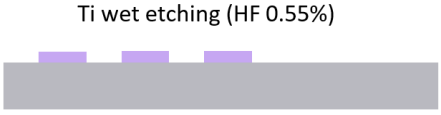

Perform a wet etching step using HF 0.55%. Etch until you can no longer see metal + 30 secs overetch. It should take around **1min** for the 50nm layer of Ti.

Rinse in the **rinser** and finish with the **Rinser Drier program**.

12. GRAPHENE GROWTH

Use the **AIXTRON BlackMagic Pro** to grow graphene using CVD
Use recipe: **'Mo_NEW_935C _20min_CH4_pre_annealing'**

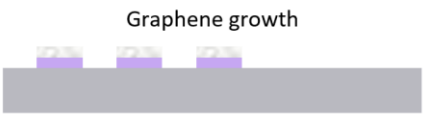

Use graphene reactor interior (Cu contaminated)!

USE RED BOX, OR WHITE BLISTER WITH CU WIRTTEN ON IT

The process wafers are now considered Cu contaminated on the front and back sides. Beware of which tweezers to use when handling the wafers. Put the wafers in a process box dedicated for Cu contaminated processes.

PART 3: AL DEPOSITION AND PATTERNING (electrodes)

Two different approaches were explored for the patterning of the Al layer: sputtering/wet etching and evaporation/lift-off.

OPTION A) SPUTTERING

13. A) METAL DEPOSITION

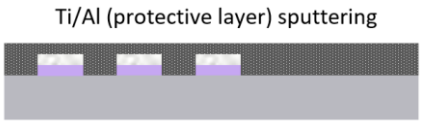

Use the cassette for contaminated wafers. Use carrier wafers for red metals for each of the test wafers. Use non-contaminated tweezers for the carrier wafers and contaminated tweezers for the test wafers.

Use the **TRIKON SIGMA** Sputter coater for the deposition of metal interface Ti+pAl layer on the wafers.
If necessary, perform a target clean with recipes '**_Trgt_Cln_Ti_50C**' and '**_TrgtCln_pAl50_DepC'**. This step will require the use of two dummy wafers.

Use recipe '**Ti_50nm_Al_100nm_50C**' for titanium and aluminium.

14. A) COATING AND BAKING

Prepare the brewer **manual spinner** with aluminum foil.
*****Use contaminated chuck for contaminated wafers and hotplate for contaminated wafers**

HMDS treatment	Treat wafers with HMDS (hexamethyldisilazane) vapor with nitrogen as a carrier gas for **10 mins**. Use cassette for contaminated wafers.
Photoresist coating	Use photoresist AZ3027. Use coating **'AZ_ECI_3027_3100nm'** (resist thickness: 3.10 µm). Gently remove PR from the back edger with a Q tip with acetone.
Soft Bake	Soft bake the wafer on a hot plate for contaminated wafers at **95 deg. C for 2 mins**. Direct contact with the contaminated hotplate.

15. A) ALIGNMENT AND EXPOSURE

Use the **SUSS MicroTec MA/BA8** mask aligner to expose the photoresist.
Use **mask** for device **G-MEA- NALV2024**, layer **METAL ELECTRODES**. Use the contaminated chuck for this step.

Use recipe **'1_FSA_Soft_Contact'**
Calculate the exposure time by consulting the contact aligner exposure energy data log [**420mJ/cm^2**] (don't add 15% of extra time).

16. A) MANUAL DEVELOPMENT

Post-exposure baking	Bake at 115 deg. C for **2 mins.** Direct contact with the contaminated hotplate.
Photoresist development	Use Shipley MF322 developer for **40 seconds**. Gently cover the wafer with the developer forming a puddle and immediately after 35-40s rinse it with DI

	water continuously to stop the development from delaminating the metal layer.
Dry	Spin dry the wafer spin. Use the contaminated chuck for the spin dryer.
Inspection	Visually inspect the wafers through a microscope and check the openings. If major defects are found remove the photoresist layer.
Hard baking	Bake **100 deg. C for 2 min.** Direct contact with the contaminated hotplate.

An extra baking step for the photoresist is needed: **30 mins @115ºC** before wet etching.

17. A) ETCHING OF TI+pAL

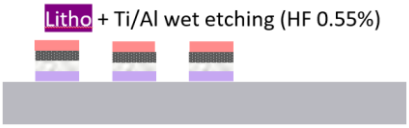

Make your own 0.55% HF bath in the wetbench of the CR10000. Perform a wet etching step using HF 0.55% for about **2 min**. (Etch until you can no longer see metal + 30 secs overetch). Rinse in DI water for **5 min**.

If inhomogeneous etching (higher etch rate at the bottom), follow this procedure:
1 min etching in HF → rinse it with DI water for 5 mins → flip the wafer by 180º → **1 min** etching in HF → rinse it again in DI water for 5 mins.

NOTE: the wet etching process was observed to be non-uniform, the etching was initiated in the patterned structures and gradually extended until the entire wafer surface was etched. This resulted in overetched structures by 1-3 um and in some cases complete removal of the protective Al electrode. If overetching this material layer is critical, consider using other approaches.

18. A) PHOTORESIST REMOVAL

Remove the photoresist with acetone followed by IPA.

NOTE: some very thin polymeric residues strongly adhered to the substrate were observed after the Al patterning. The origin of these residues was not clear. Residues persisted after additional cleaning methods with acetone and NI555 stripper at elevated temperatures and ultrasonication. Ultimately, the residues were removed by manually scrubbing the areas with a Q-tip immersed in acetone.

OPTION B) EVAPORATION AND LIFT-OFF

13. B) COATING AND BAKING

Prepare the brewer manual spinner with aluminum foil.
*****Use contaminated chuck for contaminated wafers and hotplate for contaminated wafers**

HMDS treatment	Treat wafers with HMDS (hexamethyldisilazane) vapor with nitrogen as a carrier gas for **10 mins**. Use cassette for contaminated wafers.
Photoresist coating	Use **NEGATIVE** photoresist **NLOF-2020**. Use coating **'AZ-Nlof-3500nm'** (resist thickness: 3.50µm). Gently remove PR from the back edger with a Q tip with acetone.
Soft Bake	Soft bake the wafer on a hot plate for contaminated wafers at **95 deg. C for 3 min.** Direct contact with the contaminated hotplate.

14. B) ALIGNMENT AND EXPOSURE

Use the **SUSS MicroTec MA/BA8** mask aligner to expose the photoresist.
Use **mask** for device **G-MEA- NALV2024**, layer **METAL ELECTRODES**. Use the contaminated chuck for this step.

Use recipe **'1_FSA_Soft_Contact'**
Calculate the exposure time by consulting the contact aligner exposure energy data log. Use **80mJ/cm2**.

15. B) MANUAL DEVELOPMENT

X-Link bake	Bake at 115 deg. C for **3 min**.
Photoresist development	Use **MF322** developer for **1 min** twice. Overdeveloping is not a major problem in negative photoresist.
Dry	Air dry the wafer.
Inspection	Visually inspect the wafers through a microscope and check the openings. If major defects are found remove the photoresist layer with acetone and IPA.
Hard baking	Bake **100 deg. C for 4 min.** Direct contact with the contaminated hotplate.

16. B) AL METAL DEPOSITION

Use the CHA Solution Std. for Ti/Al evaporator to deposit **10 nm** of **Ti** and **100 nm** of **Al**. **Make sure the non-gold dome and shutters have been installed**, if not ask a trained senior user to do change them. Also check that the pure Al material pocket is available.

Leave the machine with the wafers at vacuum overnight to achieve a higher adhesion of Ti/Al to the substrate.

Monitor the chamber temperature. If the temperature gets to 75ºC, stop the recipe, wait 20 mins and resume it, so as to avoid overbaking the photoresist.

17. B) LIFTOFF

Fill a glass beaker with **NI555**.
Place the wafers in a holder and submerge it in the beaker with **NI555**.
To accelerate the lift-off, do the process at high temperatures (**40-60 ºC**) for 2-3h. If PR is not completely removed, leave it overnight at RT. Rinse in DI water and allow to air dry.

18. B) INSPECTION

Check under an optical microscope the patterned Ti/Al material layer.

NOTE: fence-like structures, typical from lift-off patterning, might be present on the edges of the structures.

PART 4: AU DEPOSITION AND PATTERNING (tracks and contact pads)

19. BACKSIDE METAL DEPOSITION

Use the **CHA Solutions Std**. for the deposition of the Ti backside metal layer on the wafers.

Deposit **200nm** of **Ti** on the **backside**.

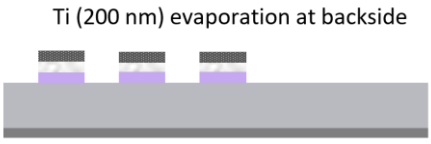

20. COATING AND BAKING

Prepare the brewer manual spinner with aluminum foil.
*****Use contaminated chuck for contaminated wafers and hotplate for contaminated wafers**

HMDS treatment	Treat wafers with HMDS (hexamethyldisilazane) vapor with nitrogen as a carrier gas for **10 mins**. Use cassette for contaminated wafers.
Photoresist coating	Use **NEGATIVE** photoresist **NLOF-2020**. Use coating **'AZ-Nlof-3500nm'** (resist thickness: 3.50μm). Gently remove PR from the back edger with a Q tip with acetone.
Soft Bake	Soft bake the wafer on a hot plate for contaminated wafers at **95 deg. C for 3 min.** Direct contact with the contaminated hotplate.

21. ALIGNMENT AND EXPOSURE

Use the **SUSS MicroTec MA/BA8** mask aligner to expose the photoresist.
Use **mask** for device **G-MEA- NALV2024**, layer **AU TRACKS**. Use the contaminated chuck for this step.

Use recipe **'1_FSA_Soft_Contact'**
Calculate the exposure time by consulting the contact aligner exposure energy data log. Use **80mJ/cm2**.

22. MANUAL DEVELOPMENT

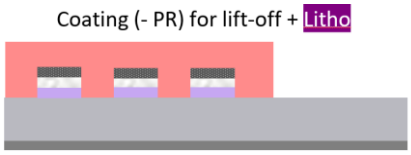

X-Link bake	Bake at 115 deg. C for **3 min**.
Photoresist development	Use **MF322** developer for **1 min** twice. Overdeveloping is not a major problem in negative photoresist.
Dry	Air dry the wafer.
Inspection	Visually inspect the wafers through a microscope and check the openings. If major defects are found remove the photoresist layer with acetone and IPA.
Hard baking	Bake **100 deg. C for 4 min.** Direct contact with the contaminated hotplate.

23. AU METAL DEPOSITION

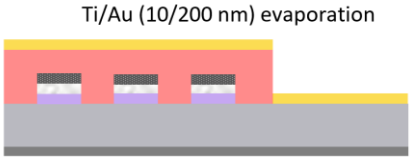

Use the CHA Solution Std. for Ti/Au evaporator to deposit **10 nm** of **Ti** and **200 nm** of **Au**. **Make sure the Au dome and shutters have been installed**, if not ask a trained senior user to do change them.

Leave the machine with the wafers at vacuum overnight to achieve a higher adhesion of Ti/Au to the substrate.

Due to the thickness of the gold layer, in order to avoid overbaking the photoresist, if the temperature gets to 75ºC, stop the recipe, wait 20 mins and resume it.

24. LIFTOFF

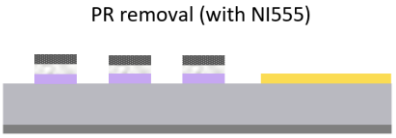

Fill a glass beaker with **NI555**.
Place the wafers in a holder and submerge it in the beaker with **NI555**.
To accelerate the lift-off, do the process at high temperatures (**40-60 ºC**) for 2-3h. If PR is not completely removed, leave it overnight at RT.

Rinse in DI water and allow to air dry.

PART 5: PARYLENE C LAYERS DEPOSITION

25. VACUUM HEAT

Vacuum heat at **200ºC** for **~1h** the wafers prior to Parylene-C deposition to remove all moisture and ensure better adhesion. Use SalvisLab vacuum heater in the Polymer Lab.

26. PARYLENE C DEPOSITION

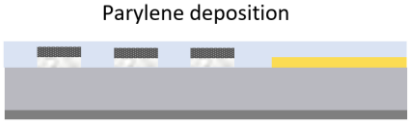

Deposit **1 µm** of Parylene C in MEMS lab using the **LABCOATER 2 (PDS 2010)**. For this purpose, use 2 g of dimer. Follow the instructions for Parylene C deposition.

To enhance the adhesion of parylene to the substrate, apply the adhesion promoter 3- (trimethoxysilyl)propyl methacrylate (Sigma Aldrich A-174) in the inner walls of the chamber with a Q-tip.

Use a carrier wafer to protect the backside of the wafer from parylene deposition.

MEASURE LAYER THICKNESS: use an additional quartz test wafer to check the parylene layer thickness. Two measurement technique options:

- *Dektak 8 Surface Profilometer: remove a section of the Parylene C layer from the edge of the wafer and then, measure the height difference.*
- *Reflectometer: use the model with the specific refractive index of parylene C.*

Do not forget to use the contaminated carrier and carrier wafers!

27. ANTI-ADHESIVE LAYER

Spin coat at 1000 rpm an anti-adhesive layer of Micro-90 in DI water (3% v/v soap solution).

NOTE: the anti-adhesive layer is deposited between the Parylene C encapsulation and sacrificial layer to facilitate the peel-off of the sacrificial layer.

28. PARYLENE C SACRIFICAL LAYER DEPOSITION

Anti-adhesive + sacrificial parylene deposition

Deposit **1 µm** of Parylene C in MEMS lab using the **LABCOATER 2 (PDS 2010)**. For this purpose, use 2 g of dimer. Follow the instructions for Parylene C deposition.

Use a carrier wafer to protect the backside of the wafer from parylene deposition.

29. COATING AND BAKING

Prepare the brewer manual spinner with aluminum foil.
*****Use contaminated chuck for contaminated wafers and hotplate for contaminated wafers**

HMDS treatment	Treat wafers with HMDS (hexamethyldisilazane) vapor with nitrogen as a carrier gas for **10 mins**. Use cassette for contaminated wafers.
Photoresist coating	Use photoresist AZ10xT. Choose a recipe with a spin coating velocity that gives a relatively thick PR layer (e.g., 6.5 µm). *NOTE: parylene to photoresist etching selectivity is around 1 due to their organic nature.*
Soft Bake	Soft bake the wafer on a hot plate for contaminated wafers at **110 deg. C for 3 min.** Direct contact with the contaminated hotplate.

Coat the extra test wafer coated with Parylene C to calculate the etching rate at a later step.
The AZ10xT photoresist requires a post bake delay of around 15 minutes.

30. ALIGNMENT AND EXPOSURE

Use the **SUSS MicroTec MA/BA8** mask aligner to expose the photoresist.
Use **mask** for device **G-MEA- NALV2024**, layer **OPENINGS**. Use the contaminated chuck for this step.

Use recipe **'1_FSA_Soft_Contact'**
Calculate the exposure time by consulting the contact aligner exposure energy data log. Use **600mJ/cm2** and no extra time.

31. DEVELOPMENT

Post-exposure baking is not needed.

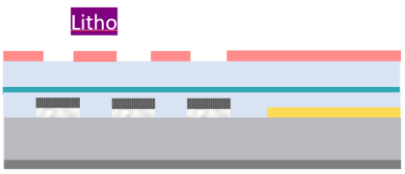

Photoresist development	Use **AZ400K** developer. Prepare a 1:4 solution. Immerse the wafer in the developer solution for 5-6 mins.
Dry	Air dry the wafer.
Inspection	Visually inspect the wafers through a microscope and check the openings. If major defects are found remove the photoresist layer with acetone and IPA

32. ETCHING OF DOUBLE-PARYLENE LAYER

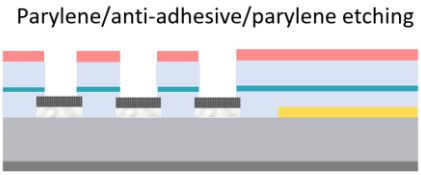

Use the **AMS110** plasma etcher to etch Parylene C
Use the **Par_etch** recipe. It uses O_2 plasma (O_2 185sccm, SF_6 15sccm, 0.08mbar, 2800W).

NOTE: Use a Si test wafer first to calculate the etching rate prior to performing this step on the final wafers. Use etching steps of one minute at a time and measure the parylene thickness in the reflectometer. It will give an idea of the parylene etching process and a reference etching rate. However, the etching dynamics will be different depending on the substrate (Si or quartz) and the material layers present.

Parylene etch rate (calculated on a Si test wafer) = 500 nm/min Parylene to photoresist selectivity ~ 1

The etch time might need to be adjusted per each wafer due to wafer-to-wafer parylene thickness variability and/or etching process variability. Attempt to etch the parylene in steps and inspect the openings under the microscope until parylene is completely etched. A change in colour is observed when the metal layer is reached, which can be used as an indicator of when the etch is complete.
Avoid overetching parylene to decrease the risk of damaging/removing the graphene layer by oxygen plasma, especially if the Al protective layer was overetched (step 17A).

33. PHOTORESIST REMOVAL

Remove the photoresist with acetone followed by IPA.
If photoresist residues are still present, leave the wafers in NI555 overnight. And if it persists, carefully scrub the areas with a Q-tip immersed in acetone.

PART 6: WAFER DICING

34. COATING AND BAKING

Prepare the brewer manual spinner with aluminum foil. Use chuck for contaminated wafers!

HMDS treatment	Treat wafers with HMDS (hexamethyldisilazane) vapor with nitrogen as a carrier gas for **10 mins**. Use cassette for contaminated wafers.
Photoresist coating	Use photoresist AZ3027. Use coating **'AZ_ECI-3027-4000nm'** (resist thickness: 4µm).
Soft Bake	Soft bake the wafer on a hot plate for contaminated wafers at **95 deg. C for 2 min**. Use carrier wafers for contaminated wafers

35. DEVELOPMENT

There will be no exposure step as the intent is to protect the whole surface from the dicing procedure.

Post-exposure baking	Bake at **115 deg. C for 2 min** in the **Memmert Oven**.
Photoresist development	Use Shipley MF322 developer for 1 min. Make sure not to overdevelop.
Dry	Spin dry the wafer.
Inspection	Visually inspect the wafers and ensure photoresist coats the entire surface.

36. WAFER DICING (Biosonics Lab)

Dice wafers with the **Disco Dicer (DAD3240).** Change the blade to a diamond blade (specific for glass).
The dicing parameters were optimized to avoid delamination of the sacrificial parylene layer. Both the feed speed and the water influx were decreased.

Dicing specifications:

- Die-to-die pitch: 20.05 mm
- Feed speed: 1 mm/s
- Spindle revolution: 20000 rpm
- Water influx
    - Blade: 1 L/min
    - Shower: 0.2 L/min
    - Spray: 0.3 L/min

37. PHOTORESIST REMOVAL

Remove the photoresist with acetone followed by IPA.

38. INSPECTION

Visually inspect the wafers through a microscope to check the openings and that all photoresist has been removed (and there are few to no residues).
If resist remains are found attempt removing them by carefully rubbing the surface with cotton bud soaked in IPA.

PART 7: PEDOT:PSS SPIN COATING & PEEL-OFF

39. ETCHING OF Ti+pAl

Make your own 0.55% HF bath in the CR 10000.
Perform a wet etching step using HF 0.55% for about 2.5 - 3min.
(Etch until you can no longer see metal + 30 secs overetch)
Rinse in DI water for 5min.

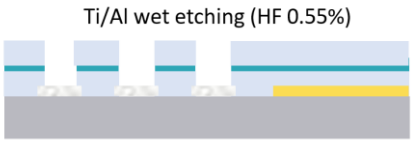

40. MO ETCHING

In cr10000 fume hoods, etch the Mo by gently covering the electrode area with a 31% H_2O_2 forming a puddle. Etch around 3 mins.

Carefully inspect the electrode openings on an optical microscope to check that the Mo underneath is almost completely removed, and graphene is not detached.

41. PEDOT:PSS SPIN COATING

Chemical preparation of the conductive polymer: A solution of PEDOT:PSS is mixed with ethylene glycol (to improve conductivity), DBSA (a surfactant to improve wettability) and GOPS (surface adhesion promoter and the crosslinker and stability enhancer of PEDOT:PSS in aqueous environments).
The mixture is first ultrasonicated for 10 to 15 min and filtered through 1.2-µm polytetrafluoroethylene filters.

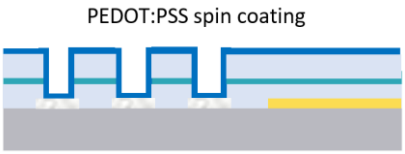

NOTE: normally a surface activation treatment is done to increase the bonding strength of the spin coated polymer to the substrate. However, such treatments would damage/etch the graphene layer.

In the polymer lab, spin coat PEDOT solution at **1000 rpm** (calculated thickness: 140 nm) and perform a soft baking step at **95ºC** for **2 min**.

42. PARYLENE C PEEL-OFF

Peel-off the sacrificial Parylene C layer manually, leaving only the PEDOT patterned on the microelectrodes. Use a scotch tape.

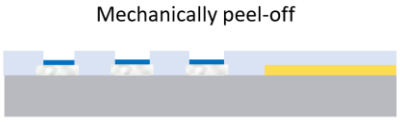

Gently remove PEDOT:PSS from the pads with a Q tip dipped in a bit of water.

Hard bake at 140 ºC for 1h. Such a high temperature is needed to properly activate the GOPS crosslinker.

Immerse the completed dies in DI water overnight to remove any remaining anti-adhesive residues and low molecular weight compounds from PEDOT.

PART 8: PACKAGING

43. ATTACH DIES TO PCBs (Biosonics Lab)

Using superglue adhesive, attach the dies to the PCBs at the corners.
Account for the height difference between the die and the PCB by placing some small wafer pieces below.
Be careful not to cover any contact pads with superglue.

Heat the assembled dies in a hot plate and cure at **80ºC for 15min.** Consider using a protective layer (e.g., aluminum foil or cleanroom tissue) over the hot plate to prevent superglue from curing on the hot plate.

Additionally, seal the edges of the dies from the backside by filling the gaps with epoxy (EPO-TEK 301-2FL).

- Prepare the epoxy by mixing Part A and Part B (check the datasheet for the mixing ratio specifications)
- Place the two-components mixed epoxy in a dispensing syringe
- Use the dispensing station and the optical microscope to carefully place epoxy on the die edges in a controllable manner.
- Cure the epoxy on a hot plate at **80ºC for 3h.**

44. WIREBONDING (EWI building, HB14.320)

Ball wirebond Au wires between the die contact pads and the PCB contact pads using the **TPT HB05** Au bonder.
Contact person: Zu Yao Chang

45. ATTACH WELLS TO DIES (Biosonics Lab)

Adhere the 3D printed wells to the surface of the MEA device by using the same epoxy (EPO-TEK 301-2FL). Consider using a small tape to keep the well in place. Use the procedure described in step 43 to prepare, dispense and cure the epoxy.

On a second round, place epoxy again covering the wirebonds to provide additional mechanical protection. Repeat the preparation, dispensing and curing process.